

Final Report to the: San Antonio River Authority

February 1st, 2025

A.T. Papagiannakis, M.H. Giacomoni, D. W. Johnson and J. Brasil



CONTENTS

CONTE	NTS	1
LIST O	F TABLES	3
	F FIGURES	
	IYMS AND ABBREVIATIONS	
	TIVE SUMMARY	
CHAPT	ER ONE: INTRODUCTION	12
1.1	Background	12
1.2	Implementation Challenges	
1.3	Study Goals and Tasks	
	ER TWO: PERMEABLE PAVEMENT DESIGN, CONSTRUCTION AND COS	
ANALY	'SIS	16
2.1	Introduction	16
2.2	Site Geology	17
2.3	Permeable Pavement Structural Details Permeable Pavement Design	18
2.3.1	Permeable Grid	23
2.3.2	Permeable Asphalt Mix Design	
2.3.3	Permeable Portland Concrete	
2.3.4	Permeable Interlocking Concrete Pavers	
2.3.5	Pavement Costs	27
СНАРТ	ER THREE: PERMEABLE PAVEMENT MONITORING AND SAMPLING	29
3.1	Water Quantity Monitoring Equipment	29
3.2	Real-time Monitoring Hardware	
3.3	Real-time Monitoring Software	
3.4	Pavement Temperature Sensors Calibration	37
3.5	Water Temperature	37
3.6	Sampling and Water Quality	37
CHAPT	ER FOUR: METHODOLOGY	40
4.1	Water Quantity Metrics	40
4.2	Infiltration Rate	
4.3	Water Quality Metrics	41
4.4	Pavement Usage	42
4.5	Statistical Analysis	46
4.5.1	Water Quality	46
4.5.2	Water Quantity	
4.5.3	Pavement Temperature	
СНАРТ	ER FIVE: RESULTS AND DISCUSSION	49
5.1	Water Quantity	49
5.2	Water Quality	
5.2.1	TSS and VSS	52
	~~~~	<i></i>

5.2.2	Fecal and Non-Fecal Bacteria	54
5.2.3	Metals – Zinc, Copper and Lead	56
5.2.4	Hardness	58
5.2.5	pH	60
5.2.6	Conductivity	62
5.2.7	Hydrocarbons (PAH and TPH)	64
5.3	Correlation Analysis	67
5.3.1	Correlations Between Water Quantity and Water Quality Parameters	67
5.3.2	Correlations Between Water Quality Parameters	73
5.4	Temperature	78
5.4.1	Pavement Sensor Calibration and Validation	78
5.4.2	Pavements Temperature	82
5.4.3	Water Temperature	88
5.5	Infiltration Rate	94
5.6	Pavement Usage	97
5.6.1	Calibration/Validation	97
5.6.2	Parking Lot Occupancy	100
5.6.3	Correlation Analysis	101
CHAPTER	SIX: CONCLUSIONS AND RECOMMENDATIONS	103
6.1	Conclusions	103
6.2	Recommendations	106
6.3	Future Study	107
REFEREN	CES	109
	X A: GEOTECHNICAL EXPLORATION AT THE CLASSEN-STEUBING P	
	X B: PRE-CONSTRUCTION MONITORING	
	X C: WATER QUANTITY MONITORING	
APPENDI	X D: TEMPERATURE GAUGE CALIBRATION	121

# LIST OF TABLES

Table 1: Borehole Depth	. 18
Table 2: Permeable asphalt concrete mixture properties (Source: TxDOT)	. 23
Table 3: In-situ layer thicknesses air voids for the PA pavement (Data Source: Raba-Kistner)	. 24
Table 4: PC mixture design	. 25
Table 5: PC compressive strength (Data source: Raba-Kistner)	. 26
Table 6: Permeable Pavement Surface Costs	. 28
Table 7: Summary of monitoring equipment, parameters, accuracy and data storage	. 31
Table 8: Three-trigger approach used for water sampling	. 38
Table 9: Water quality parameter and analysis methods	. 39
Table 10: Dates with the observed data for the ground truth	. 45
Table 11: Precipitation events monitored post-construction	. 49
Table 12: Permeable pavements peak flow reduction, delay, and water storage	. 51
Table 13: TSS and VSS Event Mean Concentrations (EMC) and loads.	. 53
Table 14: Non-Fecal and Fecal Bacteria Event Mean Concentration and loads	. 55
Table 15: Metal EMC and Load Statistics	. 57
Table 16: Hardness (CaCO ₃ ) EMC and Load Statistics	. 59
Table 17: Water runoff pH statistics	. 61
Table 18: Electric conductivity statistics	. 63
Table 19: Temperature differences before the calibration process	. 79
Table 20: Temperature differences after the calibration process	. 80
Table 21: Differences between the laser measurement and the pavement probe	. 81
Table 22: Daily minimum temperature statistics across different pavement types	. 83
Table 23: Daily average temperature statistics across different pavement types	. 83
Table 24: Daily maximum temperature statistics across different pavement types	. 84
Table 25: Water temperature data for all events.	. 90
Table 26: Average infiltration rate (in/min) per monitoring location	. 96
Table 27: Calibration/validation accuracy of pavement occupancy using the automated detection system	
Table 28: Accuracy of the automated car detection system for the whole dataset	. 99
Table 29: Water quality parameters and analysis methods	115

# LIST OF FIGURES

Figure 1: Edwards Aquifer, Bexar County and its 2011 impervious cover (Data Source: National Land Cover Dataset, Xian et al., 2011)
Figure 2: Boreholes at the Classen-Steubing Ranch Park site (Source: Arias Geoprofessionals) 17
Figure 3: Construction of the liner and perforated drain lines backfilled with gravel
Figure 4: (a) Plastic Grid (PGr), (b) Permeable Concrete (PC), (c) Permeable Asphalt (PA), and (d) Permeable Interlocking Concrete Pavers (PICP), (Source: <i>Rialto Studio</i> )
Figure 5: Manhole and instrumentation box
Figure 6: Surface drain for the CP (i.e., impermeable) pavement
Figure 7: Construction of the PGr pavement
Figure 8: Aggregate gradation for the PA
Figure 9: Construction of the PA pavement
Figure 10: Construction of the PC pavement
Figure 11: Construction of the PICP. Note temperature sensor lead wires
Figure 12: Location of the site monitoring parameters. Source: Google Earth
Figure 13: Monitoring box and equipment
Figure 14: Software flow chart
Figure 15: RTM Dashboard: Pavement temperatures are displayed at the top, with real-time hydrograph and precipitation data at the bottom streamlined in real-time after an event 36
Figure 16: Simple infiltration test apparatus
Figure 17: Digital cameras installation at the CSRP pavilion for monitoring parking lot usage . 42
Figure 18: Flow chart of automated car detection and counting algorithm
Figure 19: Examples of the imaging system of car counting by parking lot area
Figure 20: Rainfall and flow response time series for selected water quantity events 51
Figure 21: EMC boxplots for TSS and VSS by pavement type
Figure 22: Pavements pairwise comparisons for TSS and VSS using the Wilcoxon signed-rank test; Shaded cells indicate p-values $< 0.05$ (i.e., significant differences at 95% confidence) 54
Figure 23: EMC boxplot per pavement for bacteria (Non-Fecal and Fecal)
Figure 24: Pavements pairwise comparison with Wilcoxon signed-rank test for Non-Fecal and Fecal Bacteria
Figure 25: EMC boxplot per pavement for Hardness as CaCO3
Figure 26: Pavements pairwise comparison with Wilcoxon signed-rank test for Hardness 60
Figure 27: EMC hoxplot per payement for pH

Figure 28: Pavement water runoff pH pairwise comparison with Wilcoxon signed-rank test 6	2
Figure 29: Electrical conductivity boxplots	3
Figure 30: Pavements pairwise conductivity comparison with Wilcoxon signed-rank test 6	4
Figure 31: PAH number of detections and quantifications for 16 different chemicals	5
Figure 32: Total PAH EMCs for the monitored events	6
Figure 33: PAH concentration boxplots for all analyzed events	7
Figure 34: CP water quantity versus water quality correlation analysis	8
Figure 35: PICP water quantity versus water quality correlation analysis	0
Figure 36: PGr water quantity versus water quality correlation analysis	1
Figure 37: PA water quantity versus water quality correlation analysis	1
Figure 38: PC water quantity versus water quality correlation analysis	2
Figure 39: Correlation analysis between pollutants; CP	4
Figure 40: Correlation analysis between pollutants; PICP pavement	4
Figure 41: Correlation analysis between pollutants; PGr pavement	5
Figure 42: Correlation analysis between pollutants; PA pavement	5
Figure 43: Correlation analysis between pollutants; PC pavement	6
Figure 44: Relationship between DS18B20 Sensor 5 and the reference probe temperatures (°C	
Figure 45: Temperature differences between pavement surface and permeable layer bottom 8	1
Figure 46: Minimum daily temperature time series	2
Figure 47: Average daily temperature time series	3
Figure 48: Maximum daily temperature time series	4
Figure 49: Temperature changes during rainfall events	6
Figure 50: Comparison of the pavement surface temperatures median. The main diagonal show the median temperature of the pavement	
Figure 51: Characterization of the water temperature data collection	8
Figure 52: Comparison between pavement surface temperature and water temperature	2
Figure 53: Linear relationship between water temperature and pavement surface temperature 9	13
Figure 54: Comparison between observed and modeled parking lot occupancy. Images wer analyzed every 5 minutes from dawn to dusk	
Figure 55: Pavement parking occupancy by pavement type during the monitoring period 10	1
Figure 56 - Borehole location B-8 (Source: Arias Geoprofessionals)	2
Figure 57 - Borehole location B-9 (Source: Arias Geoprofessionals)	3

Figure 58: Google Earth® images pre- and during construction: (a) 03/01/2021 and (b)	
Figure 59: Pre-construction water quantity monitoring events 1 to 4	116
Figure 60: Pre-construction water quantity monitoring events 5 to 8	116
Figure 61: Pre-construction water quality monitoring.	117
Figure 62: Water quantity monitoring for events 1 to 4	118
Figure 63: Water quantity monitoring for events 5 to 8	119
Figure 64: Water quantity monitoring for events 9 to 11	120
Figure 65: Temperature sensors calibration curves	122

#### ACRONYMS AND ABBREVIATIONS

ADP= Antecedent Dry Period

API = Application Programming Interface

BMP = Best Management Practices

CSRP = Classen-Steubing Ranch Park

DT = Digital Twin

EA = Edwards Aquifer

EMC = Event Mean Concentration

EPA = Environmental Protection Agency

ICP-MS Inductively Coupled Plasma Mass-Spectrometry

IWS = Internal Water Storage

LID = Low Impact Development

LiPo = Lithium-Polymer

OGFC = Open Graded Friction Course

PA = Permeable Asphalt

PAH = Polycyclic Aromatic Hydrocarbons

PC = Permeable Concrete

PFC = Permeable Friction Course

PG = Performance Grade

PGr = Permeable Grid

PICP = Permeable Interlocking Concrete Pavers

PTFE = polytetrafluoroethylene

PP = Permeable Pavements

PQL = Practical Quantitation Limit

MDL = Minimum Detection Limit

MQTT = Message Queuing Telemetry Transport

RTM = Real-Time Monitoring

STD = Standard Deviation

TCEQ = Texas Commission on Environmental Quality

TPH = Total Petroleum Hydrocarbons

TSS = Total Suspended Solids

VSS = Volatile Suspended Solids

UHI = Urban Heat Island

#### **EXECUTIVE SUMMARY**

This study aims to evaluate the capability of permeable pavements (PPs) to mitigate both the water quality and the amount of stormwater associated with impervious surfaces on top of the Edwards Aquifer (EA). In addition, it examines how PPs affect pavement surface and water temperatures. The study involved the design and construction of parking lots with four types of permeable surfaces and a parking lot with a conventional (i.e., impermeable) surface as the comparison reference. Four PP types were constructed in the second half of 2022 on the Classen-Steubing Ranch Park in San Antonio, namely, Plastic Grid filled with aggregates (PGr), Permeable Portland concrete (PC), Permeable Asphalt concrete (PA), and Permeable Interlocking Concrete Pavers (PICP). The Conventional Pavement (CP) was constructed with a closed-graded asphalt concrete surface. Each parking lot had space for eight passenger cars (i.e., surface area of about 2,050 ft²). The base layers of the PPs are 12 inches thick to provide sufficient water storage for a 50-year rain event. Each PP was built with an impermeable bottom liner, while perforated pipes were installed, allowing water drainage from the base layer. PP unit construction costs ranged from \$13.05/ ft² to \$21.59/ ft². The PGr and the PICP were the easiest to construct requiring no specialized paving equipment. None of the PPs required any structural repairs during the observation period.

Each pavement was equipped with two main pieces of equipment: a water sampler and a water flow meter. Additional sensors included pavement and water temperature gauges, absolute water pressure transducers, and rain gauges. Power for each installation was provided by solar panels/batteries, while a wireless system was developed that allowed remote real-time monitoring

of the equipment. In addition, digital cameras were installed in the park pavilion, and an automated system was developed to measure the occupancy of each parking lot.

Data from a total of 11 rain events were captured between August 2023 and May 2024. Water quantity metrics included the Peak Reduction (i.e., the ratio of the peak flows from each PP to the peak flow of the CP), the Peak Delay (i.e., the time difference between the peak flow for each PP and that of the CP), and the Storage (i.e., the percent difference between rainfall volume and drain outflow). Water quality metrics included event mean concentration and total load of Total Suspended Solids (TSS), Volatile Suspended Solids (VSS), metals (Zinc, Copper, and Lead), counts of fecal and non-fecal bacteria, hardness, pH, and Polycyclic Aromatic Hydrocarbons (PAHs).

The PPs significantly outperformed the CP in reducing stormwater runoff and lowering peak flows through water storage. Among the PPs, the PGr provided the highest hydrological benefits in reducing and delaying peak flows. The other PPs also demonstrated significant runoff attenuation. Overall, all four PPs effectively reduced runoff volumes and mitigated flow peaks compared to the CP, underscoring their stormwater management benefits.

All four PP types yielded substantially lower TSS, and VSS concentrations in water outflow compared to the CP. The PICP showed the best performance by producing the lowest and most stable mean TSS and VSS concentrations followed closely by the PGr. The PA exhibited occasionally higher mean TSS and VSS concentrations caused by outlier events, while the PC exhibited slightly higher TSS concentrations compared to the other PP types. Overall, these findings confirm the capability of permeable paved surfaces to reduce suspended solids in runoff relative to impervious surfaces. Bacterial analyses indicated no significant difference in fecal or non-fecal coliform levels between CP and PPs.

Runoff from all pavements had low metal concentrations, often below practical quantitation limits. The runoff from the CP showed the highest Zinc loads, while PC occasionally exhibited higher effluent concentrations of Zinc and Copper. The PGr and PA tended to retain deposited metals, resulting in lower metal loads in the outflow. Hardness varied among pavement types, with the PA and PGr displaying higher levels than the CP. The PC generated markedly alkaline runoff (mean pH around 10), which helped precipitate metals out of solution, but adversely affect nearby aquatic ecosystems. The CP, PGr, and PICP generally showed moderately alkaline pH levels, while the PA's runoff was between neutral to mildly alkaline. All PPs exhibited higher mean electrical conductivity (EC) than the CP, reflecting elevated dissolved ion content. The PC consistently showed the highest conductivity. PAHs concentrations were generally low for both CP and PPs, with CP exhibiting higher levels in some of the measurements.

The PPs demonstrated better thermal performance than the CP. The PC and PICP maintained lower average and maximum temperatures, while the PGr exhibited higher cooling at night. The PA produced the highest daytime maxima. During rainfall, the PGr and the PC outflows showed consistently lower average water temperatures than the PA and the PICP.

Automated car detection revealed notable differences in usage by pavement type, with the PICP being the most heavily used and the PGr the least used. This was likely due to drivers' preference for more familiar parking lot surfaces. The CP and PA showed moderate usage with intermittent peaks, while the PC experienced relatively lower but steady usage. Statistical correlations indicated that higher occupancy of the CP corresponded to elevated TSS levels, while occupancy had no significant effect on TSS for the PPs, underscoring the effective pollutant mitigation offered by permeable designs.

Monitoring infiltration rates is essential to assess future clogging that will require maintenance to restore pavement permeability. For all the PPs, the infiltration rate exceeded the maximum rainfall intensity throughout the monitoring period, suggesting no need to maintain the surfaces. Clogging over time can be mitigated by vacuum sweeping or pressure washing. It is recommended that the City of San Antonio follows the maintenance routine defined in the San Antonio River Authority's Low Impact Development (LID) Technical Design Guidance Manual.

The findings of this study suggest that PPs have significant environmental benefits and should be considered as one of the LID strategies available for mitigating impermeable ground cover effects in delicate ecosystems and especially over sensitive aquifers. Wider use of permeable surfaces will result in lowering construction costs that will make them more competitive. Constructing PGr and PICP surfaces are particularly attractive since they require no specialized equipment for construction and repair.

### **CHAPTER ONE: INTRODUCTION**

### 1.1 Background

The Edwards Aquifer (EA) is the main water source for over 2 million people living in South-Central Texas. It is a feature of the Karst terrain that extends for over 180 miles, from Kinney and Edwards counties in the west to Caldwell and Guadalupe counties in the east. The demand for EA water is anticipated to increase substantially as the region experiences one of the highest population growths in the U.S. The EA is particularly vulnerable to urbanization, especially over its recharge zone. In urban areas, replacing the natural land cover with impervious surfaces, such as roads, parking lots, rooftops, and sidewalks, increases pollutant concentration in runoff (e.g., bacteria, heavy metals) (Tong et al. 2009) while reducing infiltration and aquifer recharge rates (US EPA 1993). Furthermore, the urban drainage infrastructure removes excess runoff from the surface, which results in concentrated runoff volumes and faster and higher peak flows, which can cause downstream flooding, property damage, and loss of life (Sharif et al., 2014; Fang et al., 2014).

Developing effective strategies to mitigate the adverse effects of urbanization on the EA is essential in sustaining this unique resource. An integral part of these strategies is adopting green infrastructure in the form of Low Impact Development (LID). LID are decentralized stormwater control measures designed to mitigate the impact of urbanization by restoring the hydrologic flow regime near pre-development conditions. LID encompasses several structural Best Management Practices (BMPs) that include bioretention, sand filters, rainwater harvesting, bioswales, infiltration trenches, retention basins, vegetation filter strips, and permeable pavements (PP) (Dorman et al., 2013). Among all LID BMPs, permeable pavements have significant potential to improve the sustainability of water resources in urban areas due to the large footprint of pavement

surfaces in the built environment. For instance, conventional paved surfaces (i.e., roadways, walkways, and parking areas) comprise a significant fraction of the impermeable ground cover in Bexar County, which is estimated to be about 14.1% of its total area (Figure 1).

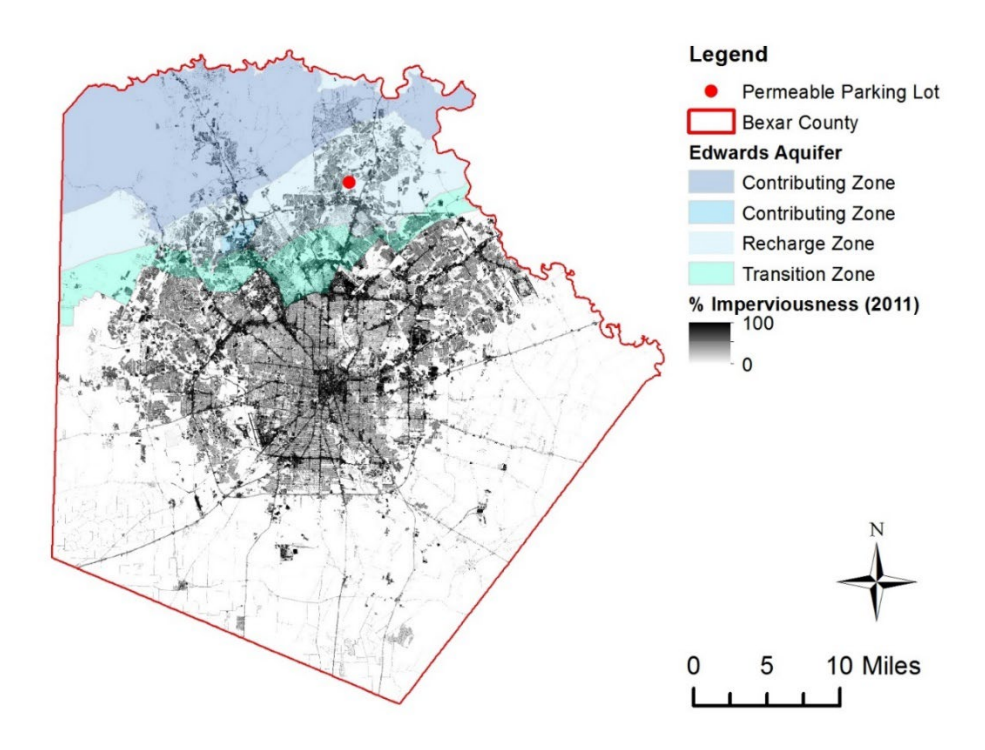


Figure 1: Edwards Aquifer, Bexar County and its 2011 impervious cover (Data Source: National Land Cover Dataset, Xian et al., 2011)

## 1.2 Implementation Challenges

Despite the use of PPs, especially on roadways in the form of open-graded friction courses (OGFCs) or permeable friction courses (PFCs) (TXDOT 2016), there are still significant barriers to their broader acceptance as a stormwater BMP option in urban environments. The reasons are primarily financial and regulatory. The literature shows that, even though pollutant removal efficiency can be relatively high, it could vary depending on the PP design (e.g., layers, liners), the pollutant loads, and the local rainfall characteristics (Davis et al. 2003; Kim et al. 2012).

Financially, there is still a perception among developers and the public that green stormwater infrastructure, such as PPs, is more capital-intensive to construct than traditional roadways and

parking lot pavements. This is compounded by the uncertainties in maintenance costs, which depend on the design and location of the projects. Another reason that prevents the wider application of stormwater LID BMPs is that the technology is relatively new, and most commercial suppliers do not release the technical details of their designs (Houdeshel et al., 2011). As new data is collected, new evidence suggests LIDs have similar capital and maintenance costs with conventional stormwater drainage methods (Liu et al. 2014).

Stormwater regulation also plays an important role in implementing sustainable BMPs nation-wide. States, counties and municipalities, typically located on the East and West Coasts, have more stringent stormwater requirements than prescribed by the Federal government. Other jurisdictions still lack a more stringent regulatory framework. In Texas, for example, stormwater regulations set by the Texas Commission on Environmental Quality (TCEQ) require stormwater treatment to achieve 80% reduction in total suspended solids (TSS) on top of the EA recharge zone (TCEQ 2005). There are no requirements for controlling other pollutants such as nutrients, metals and bacteria. On the other hand, TCEQ requires LID BMPs to have infiltration barriers (i.e., liners) preventing treated stormwater from directly infiltrating the EA. These liners disrupt the hydrologic flow regime and hinder aquifer recharge while adding construction costs. Clearly, wider implementation of BMPs, such as PPs, requires a better understanding of the advantages PPs have in reducing urban pollution and peak stormwater discharge volumes.

### 1.3 Study Goals and Tasks

The primary goals of this study are: 1) to demonstrate how PP designs can mitigate the water quality and amount of stormwater runoff associated with impermeable pavement surfaces over the Edwards Aquifer recharge zone; and 2) to examine how PP designs reduce pavement surface temperatures and water runoff temperatures and thus contribute to mitigating urban heat island

(UHI) effects. The study performs a comprehensive monitoring campaign where water quality, water quantity, and temperature data were collected for four types of PP: namely (a) plastic grid filled with aggregates, (b) Permeable Portland Concrete, (c) Permeable Asphalt Concrete and (d) Interlocking Concrete Pavers. In addition, this study examined whether the PP designs reduce pavement surface temperatures and water runoff temperatures. The study involved three main tasks, (1) design/construction several PP parking lot surfaces and a conventional (i.e., impermeable) surface for comparison, (2) design/install the monitoring equipment for each parking lot and (3) collect, analyze and interpret the data.

The report consists of six chapters. Chapter II showcases the design, construction and cost estimates of all the four PP and control parking lots. Chapter III describes the monitoring and sampling setup, including the water quantity and quality equipment, real-time monitoring hardware and software, pavement temperature sensors, and water sampling. In Chapter IV, the main methodological steps for data analysis are presented, including the metrics and statistical analysis. Chapter V presents all the results and discussion about the results for water quantity (volume, peak flow and time), water quality (TSS, VSS, Fecal and Non-Fecal Bacteria, metals, hardness, pH, conductivity and hydrocarbons). In the same chapter, we present correlation analysis between the different parameters, as well as the characterization of pavement and water temperature for all the pavement surfaces. Last, chapter V shows the results for infiltration tests, and pavement car usage. The report concludes with final remarks, recommendations, and topics for future research in Chapter VI.

# CHAPTER TWO: PERMEABLE PAVEMENT DESIGN, CONSTRUCTION AND COST ANALYSIS

#### 2.1 Introduction

This chapter presents the planning, design, and construction details of four alternative PP parking lot surfaces and an impermeable parking lot pavement to serve as control. The rationale for including a control parking lot is twofold. First, unlike other stormwater control measures BMPs, the influent of PP is in the form of sheet flow, which is very hard to sample due to the shallow water depth. Therefore, characterizing the water quality of PP needs to occur through the effluent samples, which were collected through an underdrain pipe. Second, having the same data collected under the same hydrologic and climatic conditions allows for a direct comparison between the different types of pavements.

The location of the project is the Classen Steubing Ranch Park, established in the Stone Oak area in San Antonio, Texas. This location was suggested by the Public Works Dept. and the Transportation and Capital Improvements Dept. of the City of San Antonio (COSA). The selected site is located on top of the recharge zone of the EA (see red dot on Fig 1) and offers a tremendous opportunity to educate the public about stormwater sustainability, Low Impact Development, and the Edwards Aquifer.

Each parking lot is 36 ft by 57 ft (area 2050 ft²), and has a capacity of eight parking spots. The parking lots were designed so the only influent comes from direct rainfall. Therefore, the drainage area is the same as the parking lot area. No stormwater runoff from neighboring areas infiltrates through the PPs. This setup allows the influent volumes and rates to be similar among all the five parking lots being monitored.

The design of each parking lot followed the recommendations of TCEQ regulations applicable to LIDs installed at the top of the EA recharge zone (TCEQ 2005), and the San Antonio River Basin Low Impact Development Technical Design Guidance Manual 3rd Edition (SARA, 2023). The structural pavement design details (i.e., layer thicknesses) were based on hydrological calculations, pavement layer properties and the geological characteristics at the site.

## 2.2 Site Geology

The geological stratigraphy at the Classen-Steubing Ranch Park (CSRP) was established through several boreholes drilled at the site (Figure 2). This work was carried out by *Arias Geoprofessionals*. The depth of each borehole varied by location (see Table 1: Borehole Depth).



Figure 2: Boreholes at the Classen-Steubing Ranch Park site (Source: Arias Geoprofessionals)

Table 1: Borehole Depth

Boring Structure		Depth, ft
No.		
B-1	Pavilion	10.0
B-2	20 Space Parking Lot	4.5
B-3	Access Road and Lighting	8.5
B-4	Low Water Crossing	8.5
B-5	Low Water Crossing	13.5
B-6	B-6 Access Road and Lighting	
B-7	50 Space Parking Lot (North)	4.75
B-8	Pavilion and Restroom	18.5
B-9	50 Space Parking Lot (South)	4.5
B-10	Proposed Playground	12.0

The stratigraphy of boreholes B-8 and B-9, which are nearest to the PP parking lot location, is shown in Appendix A. Three main layers were identified across the C-S park site, namely a residual clay-gravel (GC) and fat clay (CH) overlying a limestone layer from the Edwards Limestone formation (*Ked*), referred to as layers I, II and III, respectively. It is observed that Layer II (i.e., the CH layer) is not present in these two locations, and hence, expansive clays were not an issue at the parking lot locations. Borehole location B-9 revealed hard bedrock at the surface (i.e., missing layers I and II), which suggests excellent foundation conditions at that location. Split spoon (SS) samples were possible only at borehole location B-9 at depths of 0-3.5 feet (GC layer) and 5.5-11 feet depth (GC embedded into the limestone). Standard penetration testing revealed 36 to 50+ blows at these two locations suggesting dense layer conditions through the layers (i.e., estimate unconfined strength higher than 4 tons/ft². Finally, it is noted that no water table was encountered at the boreholes drilled (i.e., drilling took place in Dec. 2019). Overall, no foundation problems were identified during the geotechnical investigation.

### 2.3 Permeable Pavement Structural Details Permeable Pavement Design

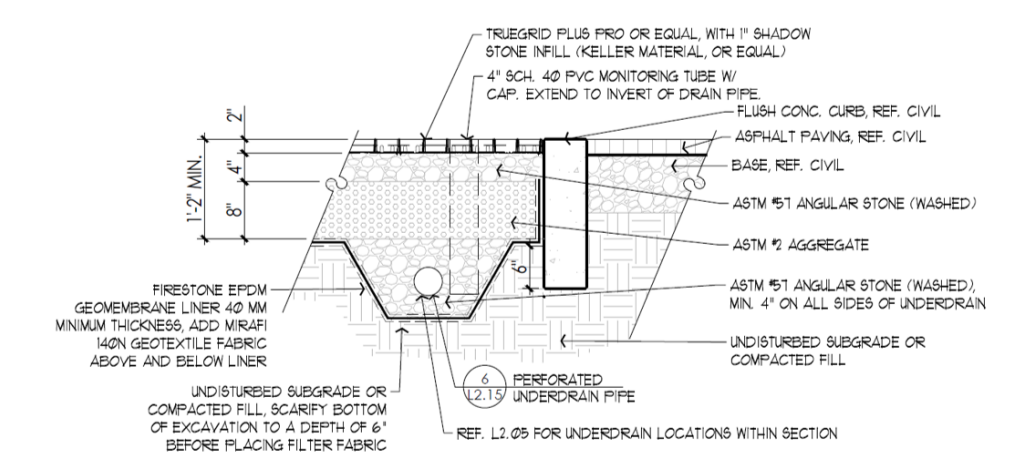
Four PP types were constructed with different surfaces, namely (a) Truegrid® plastic grid filled with aggregates, (b) Raincrete® Permeable Portland Concrete, (c) Permeable Asphalt Concrete and (d) Interlocking Concrete Pavers donated by Keystone Hardscapes Inc. These pavement types

are hence, referred to as Permeable Grid (PGr), Permeable Concrete (PC), Permeable Asphalt (PA) and Permeable Interlocking Concrete Pavers (PICP). These four PP were selected because they are included in the SARA LID Technical Design Guidance Manual.

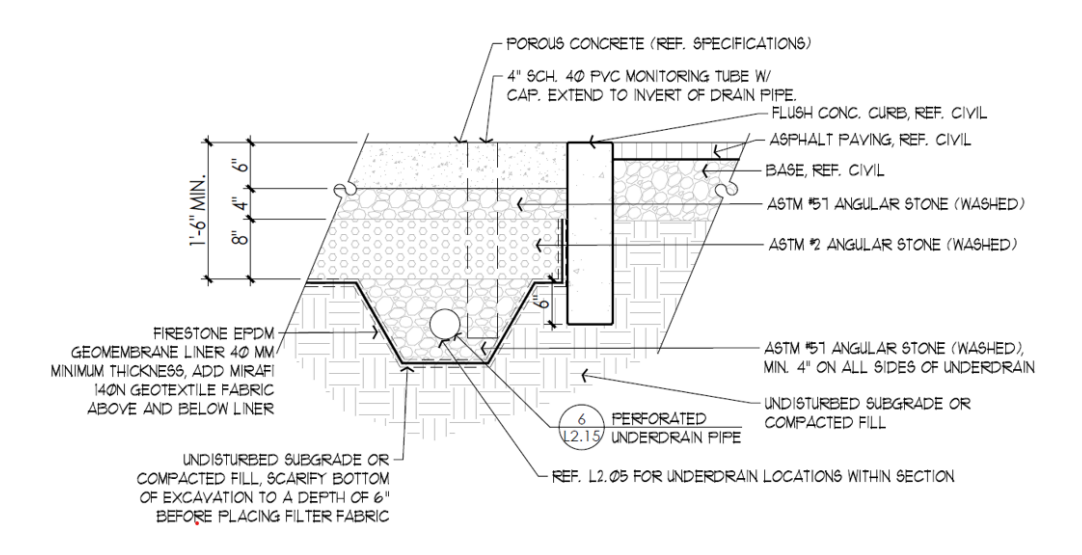
Common to the design of these sections were thick base/subbase layers consisting of 4 inches of ASTM No. 8 washed gravel placed over 8 inches of ASTM #2 washed crushed stone. It was estimated that the 12-inch base/subbase layers provide sufficient water storing capacity to accommodate a 50-year rainfall of 12 inches (i.e., given the area of each permeable surface of 2,050 ft², the volume of the voids is approximately 800 ft³, assuming a porosity of 0.4). In addition, a 40 mm geomembrane was placed at the top of the excavated subgrade and perforated water collector pipes were inserted along the length of the parking area and backfilled with ASTM #1 stone (Figure 3). The structural details of the four pavement sections and the configuration of the perforator collector pipes are shown in Figure 4 (a) to (d). Pavement construction took place in the summer of 2022 over a period of several months.



Figure 3: Construction of the liner and perforated drain lines backfilled with gravel

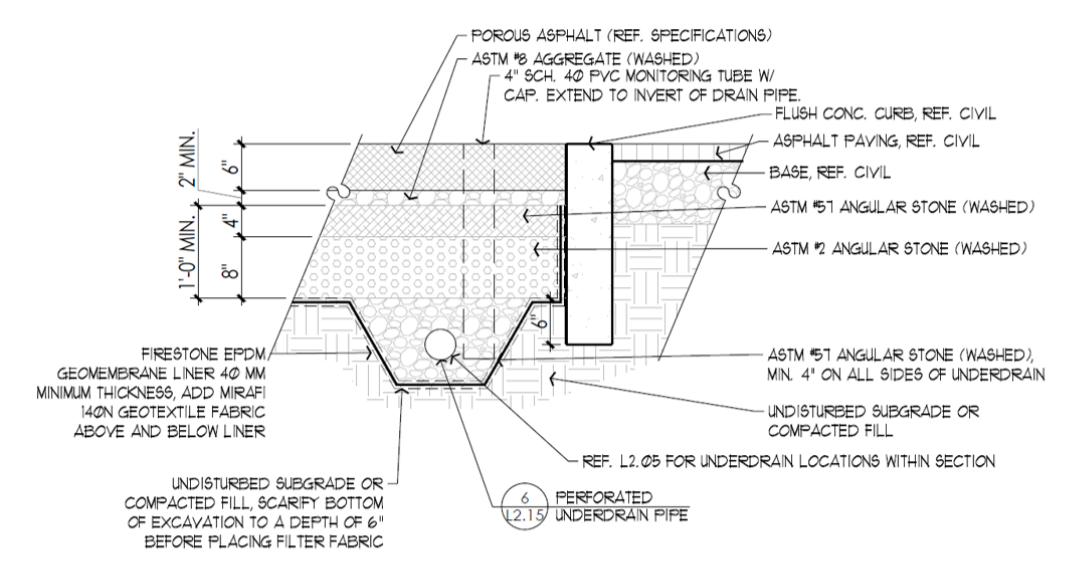


# SECTION: POROUS GRID PAVER

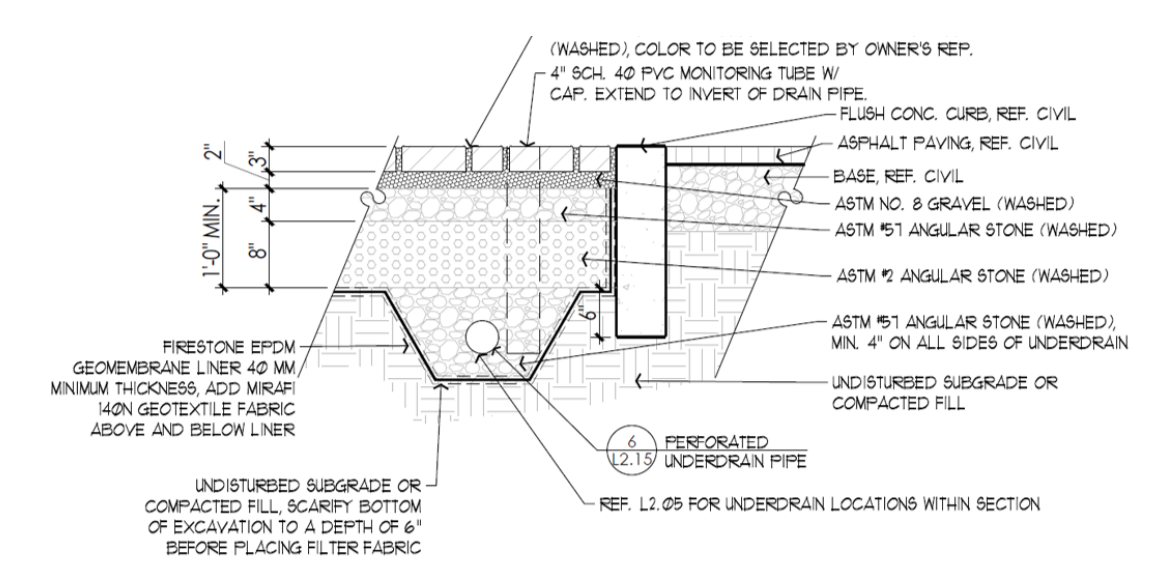


# SECTION: POROUS CONCRETE SCALE: 1"= 1'-0"

Note: The curbs were raised to 4 inches above the finished pavement surfaces to better isolate the rainfall on each parking lot surface.



# SECTION: POROUS ASPHALT



SECTION: POROUS CONCRETE PAVERS
SCALE: 1"= 1'-0"

Note: The curbs were raised to 4 inches above the finished pavement surfaces to better isolate the rainfall on each parking lot surface.

Figure 4: (a) Plastic Grid (PGr), (b) Permeable Concrete (PC), (c) Permeable Asphalt (PA), and (d) Permeable Interlocking Concrete Pavers (PICP), (Source: *Rialto Studio*)

The collector pipes were led to manholes containing instrumentation to monitor water volume and intake pipes for water sampling (Figure 5). Water drained from the manholes by daylighting downstream from the parking lots.



Figure 5: Manhole and instrumentation box

In addition to these four permeable pavements, a Conventional Pavement (CP) (i.e., impermeable) asphalt concrete pavement parking lot of the same area was constructed to provide the control for the experiment. Water runoff from this pavement was removed via a surface drain (Figure 6). The drain was directed to a separate manhole and instrumentation box.



Figure 6: Surface drain for the CP (i.e., impermeable) pavement

# 2.3.1 Permeable Grid

The PGr pavement was constructed by laying the grid on the ASTM #57 stone and then filling the surface with 1-inch crushed gravel (Figure 7: Construction of the PGr pavement). The grid provides confinement for the gravel and prevents its horizontal movement under the action of traffic.



Figure 7: Construction of the PGr pavement

### 2.3.2 Permeable Asphalt Mix Design

The PA mixture used was a typical design used by the Texas DOT (TxDOT) to construct permeable friction courses (PFCs). It is designated as 342-PFC-C. The key design properties are summarized in Table 2. It can be seen that the design air voids are 80%.

Table 2: Permeable asphalt concrete mixture properties (Source: TxDOT)

Property	Value			
Aggregate bulk specific gravity (G _{sb} )	3.149			
Binder grade	PG76-22 (source: Valero)			
Binder specific gravity (G _b )	1.038			
Fiber content	0.30%			
Binder content	6.4%			
Mix bulk specific gravity (G _{mb} )	2.171			
Mix theoretical max specific gravity (G _{mm} )	2.713			
Air voids (VTM)	80%			

This was accomplished by the gap-graded aggregate gradation of the mixture (Figure 8).

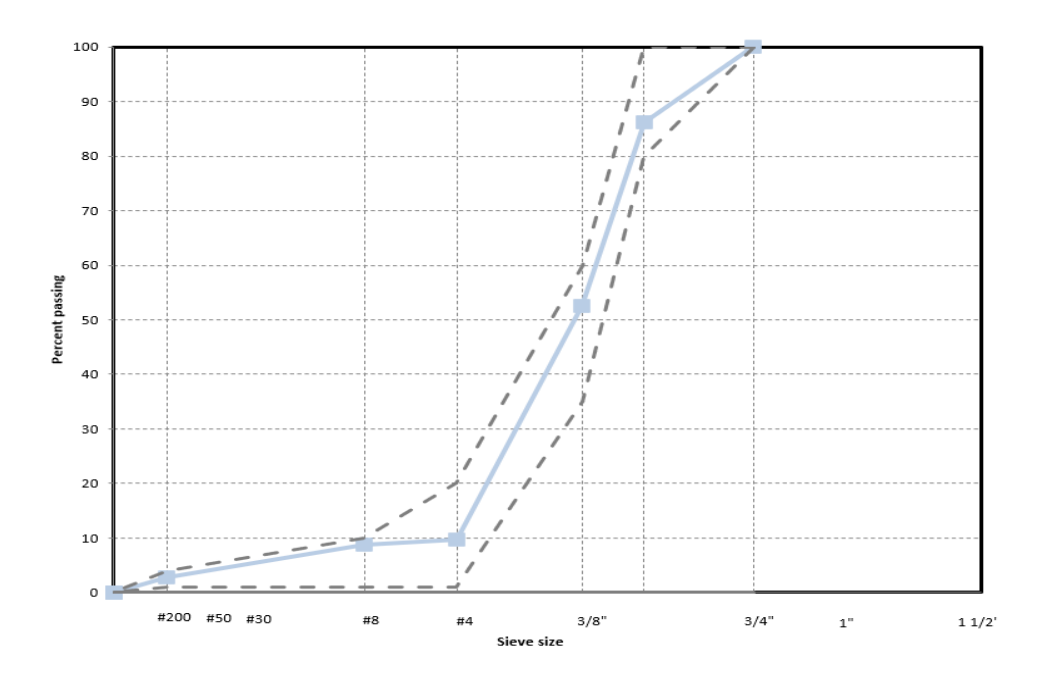


Figure 8: Aggregate gradation for the PA

Following construction (Figure 9), permeable asphalt concrete cores were obtained for volumetric analysis. The results show that the thickness of the asphalt concrete slab ranges between 5 and 6.75 in and that the air voids are over the designed 20% design target (Table 3).

Table 3: In-situ layer thicknesses air voids for the PA pavement (Data Source: Raba-Kistner)

Test #	Location	Received thickness in.	Trimmed thickness in.	Compaction %	Air voids %
1	4' South 5' West of NE corner	6.75	5.82	78.1	21.9
2	4' South 5' West of NE corner	6.35	5.80	76.7	23.3
			Average	77.4	22.6
3	5' North 10' West of SE corner	5.25	4.41	73.5	26.5
4	4' North 10' West of SE corner	5.75	5.04	74.5	25.5
			Average	74.0	26
5	5' North 10' East of SE corner	5.00	4.45	77.8	22.2
6	5' North 10' East of SE corner	5.25	4.52	79.4	20.6
			Average	78.6	21.4



Figure 9: Construction of the PA pavement

### 2.3.3 Permeable Portland Concrete

The PC was supplied by *Raincrete®*. This was a roller-compacted proprietary mixture that involved joints and dowel bars. The joints were made from pressure-treated wood that served as the guide for the compaction rollers (Figure 10). The mixture had the following composition:

Table 4: PC mixture design

Property	Value			
Coarse 3/8" aggregate	2485 lbs			
Fine aggregate	0 lbs			
Portland Cement (TypeI/II)	64 lbs			
Raincrete® admixture (proprietary)	3 gallons			
Water	12 gallons			
Air voids	18%			
Unit weight 12	125.61 lbs/ft ³			

Cylindrical samples 4-inches in diameter were obtained during pouring and tested in compression at 7 and 28 days (Table 5). The 28-day strength ranged from 71% to 111% of the design target of 3,000 psi.



Figure 10: Construction of the PC pavement

Table 5: PC compressive strength (Data source: *Raba-Kistner*)

SET INDEX	: S	et 1 of 1		ARF	RIVE SITE:	9:3	30	DEPART S	ITE:	14:30
SUPPLIER: Easy Mix		BATCH TIME: 13:0		:00	AIR CONTENT (%):		4.1			
TRUCK NO	:	309		SAM	IPLE TIME:	13	:13	UNIT WEI	SHT (pcf):	NA
TICKET NO	):	2378	35	SAM	IPLE TEMP. (	°F): 94		FIELD CUR	RED (day):	1
SAMPLED	AT (cu yds)	: 8		AME	BIENT TEMP.	(°F): 83		SAMPLE T	YPE:	Concrete Cylind
DESIGN ST	R.(psi):	3,00	0	SLU	MP (in.):	8.0	00	SAMPLE S	SIZE(in.):	4 x 8
PRODUCT	NO.:	Perv	ibus	CLA	SS:	Α		WATER AD	DDED:	5
PLANT NUMBER: Easy Mix,						RECEIVE	D DATE:	8/23/2022		
SPECIMEN	DATE	AGE	LOAD	DIAMETER	AREA	STRENGTH	PERCENT	FRACTURE	T	ESTED
NUMBER	OF TEST	(days)	(lbs)	(in)	(in.²)	(psi)	OF DESIGN	TYPE		BY
1	08/29/2022	7	29,980	4.01	12.63	2,370	79	Type 4	CHRISTO	PHER PARTON
2	08/29/2022	7	33,220	4.01	12.63	2,630	88	Type 4	CHRISTO	PHER PARTON
3	09/19/2022	28	33,030	4.01	12.63	2,620	87	Type 4	CHRISTO	PHER PARTON
4	09/19/2022	28	26,870	4.01	12.63	2,130	71	Type 4	CHRISTO	PHER PARTON
5	09/19/2022	28	41,950	4.01	12.63	3,320	111	Type 4	CHRISTO	PHER PARTON

# 2.3.4 Permeable Interlocking Concrete Pavers

The interlocking pavers used for the PICP were 3.50-in. thick and arranged in a herring-bone pattern with 1/4 -in. gaps. They were installed on an ASTM #8 washed gravel leveling course and backfilled with the same type of gravel filling the gaps (Figure 11).

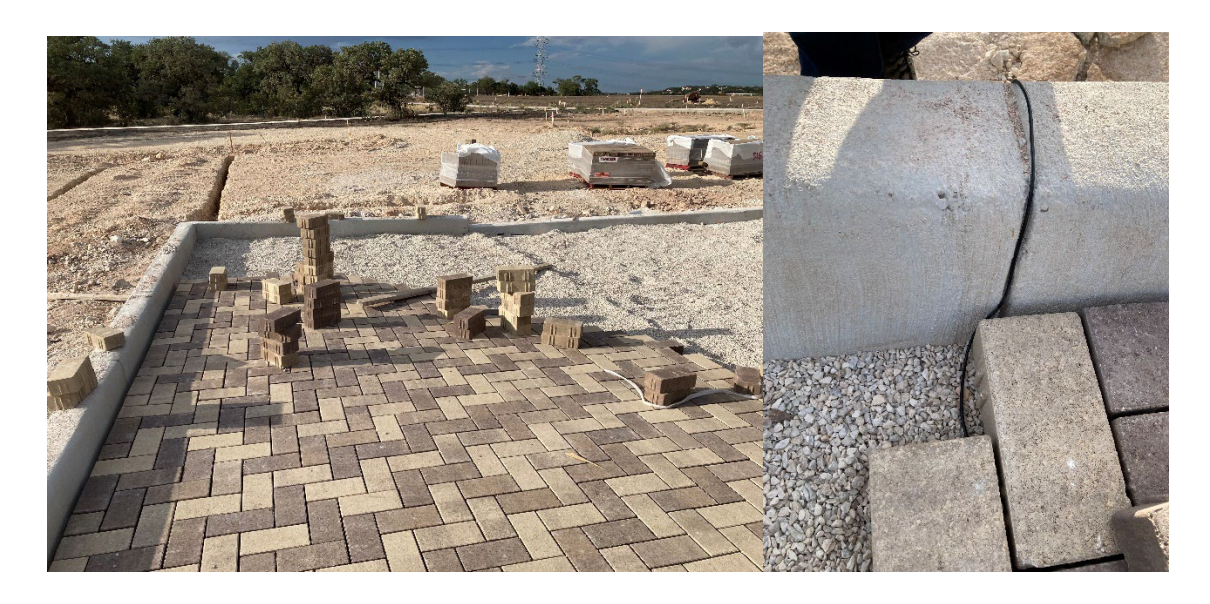


Figure 11: Construction of the PICP. Note temperature sensor lead wires.

### 2.3.5 Pavement Costs

The cost of the parking lot permeable pavement surfaces is summarized in Table 6. It includes only the cost of the surface layer and reflects markup and fees charged by the general contractor (i.e., Crown Hill Construction LLC). It is noted that the subgrade preparation, drainage and base layer materials were comparable between these four alternative permeable pavement types. As a result, the unit prices in Table 6 provide a direct comparison between these four PP alternative surfaces. These unit costs reflect the small volume of the material necessary for each pavement surface (i.e., approximately 1,025 ft³). Economies of scale are expected to reduce these unit costs, where larger volumes of material are used. A direct comparison between the cost of the PPs and the CP was not meaningful, since the latter was the same material used for all the Park access roads and hence it was produced at much higher volumes. A more meaningful comparison was made considering the unit prices established from 2022 TxDOT contract bids (Papagiannakis and Masad 2024). The unit cost of PFC was approximately twice as high as the unit cost of conventional asphalt concrete with the same PG76-22 asphalt binder (i.e., \$187/ton versus \$96/ton).

Table 6: Permeable Pavement Surface Costs.

Permeable Pavement Type	Total Cost \$	Unit Cost \$/ft ²
PGr (Includes the cost of filler gravel)	\$34,100	16.63
PC	\$44,250	21.59
PA	\$26,756	13.05
PICP (Includes the value of the interlocking pavers donated)	\$34,100	16.63

### CHAPTER THREE: PERMEABLE PAVEMENT MONITORING AND SAMPLING

This chapter outlines the monitoring equipment, monitored parameters, equipment maintenance, calibration, sensor deployment, and sampling strategies used during this project. Continuous monitoring of permeable pavements enables a direct comparison with conventional asphalt. Therefore, this chapter serves as the basis for the data analysis and discussion of the results presented in Chapter Four.

### 3.1 Water Quantity Monitoring Equipment

The monitoring setup includes equipment for monitoring the pavement temperature, rainfall, pavement outflow, and water temperature. Figure 12 shows the permeable and conventional parking lot surfaces. Each pavement was equipped with a monitoring box, except for the PA and the PC, which shared the same box.



Figure 12: Location of the site monitoring parameters. Source: Google Earth

Each monitoring box was off-grid and was powered by a 200W solar panel, a Maximum Power Point Tracking (MPPT) solar panel controller, and a 12V 100 mAh lithium-polymer (LiPo) battery (Figure 13). The battery sets provided two days of power without any sunlight.

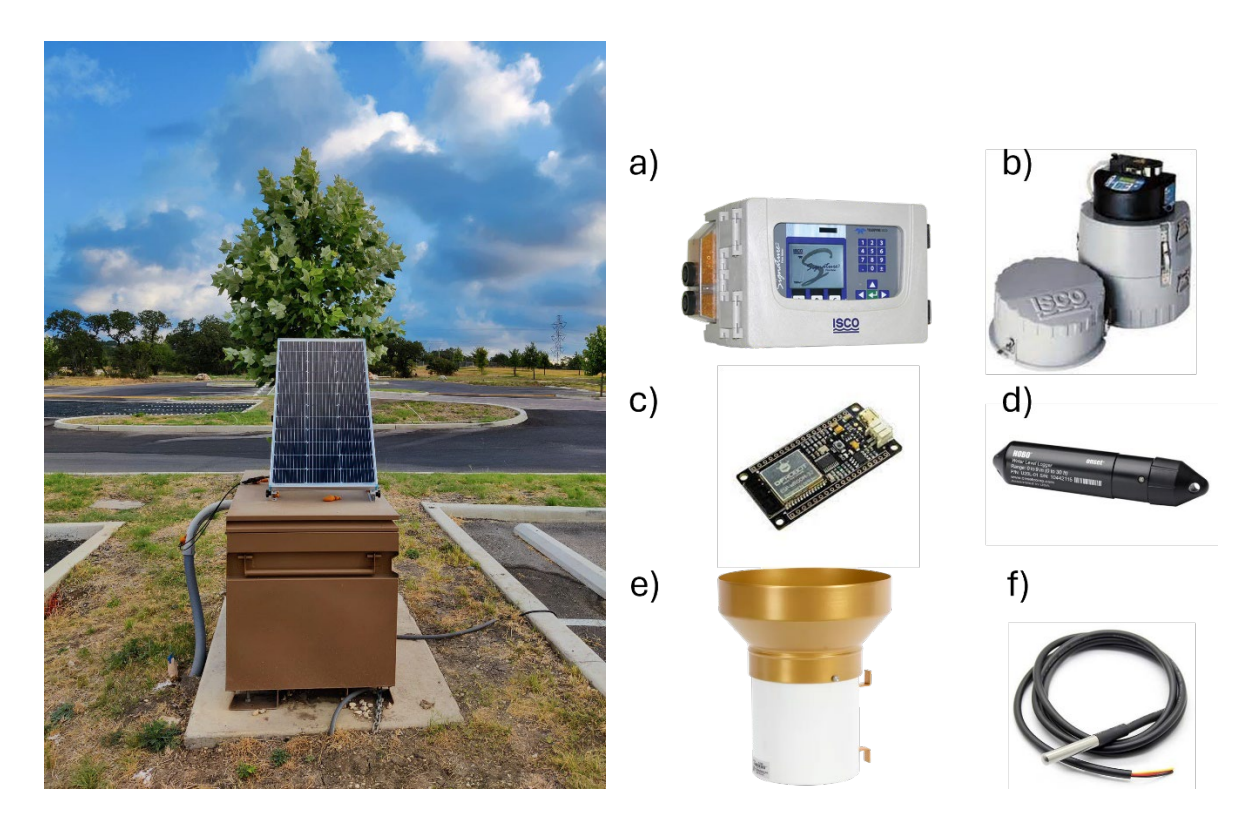


Figure 13: Monitoring box and equipment

Each monitoring box contained an ISCO Bubbler flowmeter (Figure 13a), an ISCO 6712 sampler (Figure 13b), and an ESP32 box (Figure 13c). The ISCO Bubbler monitors the water level inside the pavement underdrain. The water level was converted to flow through a V-Notch Thel-Mar 6-inches in diameter weir through a calibration curve. Each pavement had two DS18B20 12-bit temperature sensors (Figure 13f) to monitor the pavement temperature. The temperature sensors were placed at the top of the base layer (i.e., bottom of the permeable surface layer), spaced horizontally 1 foot from each other and 1 foot from the curbside (Figure 12).

Each permeable pavement had an inspection pipe close to the outlet, as shown in Figure 12, where a HOBO UL20 absolute pressure transducer was placed (Figure 13d). This pressure transducer monitored the pavement water level and temperature. It was equipped with a transducer measuring atmospheric pressure to account for atmospheric pressure variations.

Two 6-inch tipping bucket rain gauges monitor the site's rainfall (Figure 13e). The rain gauges were placed on an 8-foot pole far from any obstacles that could interfere with the measurements. The monitoring equipment, parameters measured, their frequency, accuracy, and data storage are summarized in Table 7.

Table 7: Summary of monitoring equipment, parameters, accuracy and data storage

Parameter	Equipment	Time Resolution	Units	Accuracy	Data Storage
Water Level and Water Flow	ISCO Bubbler Flowmeter/Thel-mar V-notch weir	1 to 5 minutes	in./cfs	±0.06 in.	USB flash drive
Pavement Temperature	DS18B20	5 minutes	°F	±0.5 °C	SD card
Rainfall	Texas Electronic TR- 525I	Accumulated tips for 5 minutes	in.	±1% from 0-2 in./h	SD card
Water temperature	HOBO U20L Pressure Transducer	1 to 5 minutes	°C	±0.44 °C	Proprietary coupler
Water sampling	ISCO 6712	See Table 8	-	-	USB flash drive

### 3.2 Real-time Monitoring Hardware

Various data retrieval processes, ranging from USB flash drives to proprietary systems, would have made the data collection time-consuming and prone to data loss. Additionally, each device's unique logging and timestamping method hindered data synchronization, leading to potential discrepancies between the variables monitored. Instead, a real-time monitoring (RTM) system was developed and installed at the CSRP site to improve pavement data storage and transmission. The RTM used the DFRobot Firebeetle v2 ESP32-E and several external modules to integrate the data from different devices.

Key elements included a DS3231 Real Time Clock module to maintain date and time during power disruptions, a MicroSD SDHC TF card adapter with a 32GB SD card for offline data backup, and a TTL to RS-485 transceiver utilizing the Modbus protocol for data retrieval from the

ISCO Signature flow meter. A power supply module was also employed to step down the 12V battery voltage to the 5V needed to power the ESP32. The setup was cost-effective, with the total kit priced under \$25, demonstrating the economic viability of open-source solutions in urban water management systems. A 4G WiFi Router using a Mint SIM Card was also placed at the site to provide Internet connectivity to the devices and allow remote data retrieval.

The system collected data from the sensors and streamlined them across various devices. The RTM units gathered pavement temperature, water level, and rainfall at the frequencies given in Table 7 and sent the data to a Network Time Protocol (NTP) server. Subsequently, the data was transmitted to a Node-RED API on a Raspberry Pi via a Message Queuing Telemetry Transport (MQTT) protocol. Node-RED is an open-source, flow-based programming tool designed to integrate hardware devices, APIs, and online services as part of the Internet of Things by enabling event-driven applications to be visually constructed with minimal coding. This centralized system fed into an InfluxDB database that in-turn fed a Grafana dashboard, enabling real-time data visualization.

The rain gauges used a reed switch sensor and a magnet attached to the bucket. When the magnet passes near the reed switch, it closes the circuit, logging a "tip" in the datalogger. However, the reed switch was incompatible with the RTM system (i.e., its signal was too weak for detection by the ESP32). Therefore, it was necessary to modify the tipping bucket mechanism. This was done by replacing the reed switch with a Hall effect sensor. Like the reed switch, the Hall effect sensor detects magnetic fields. However, instead of a physical connection, it uses a solid-state mechanism that generates a voltage in the presence of a magnetic field. With no moving parts, the Hall effect sensor is more durable and better suited for integration with the ESP32 monitoring

system. Unlike the reed switch, the Hall effect sensor required a power source, which was not an issue since all monitoring boxes had a power supply.

### 3.3 Real-time Monitoring Software

Custom software was developed to allow RTM of precipitation events and remote data collection and transmission. The design of this software was modular, meaning that the same code could handle different sensors. A flowchart indicating the sequence of actions followed in RTM of precipitation events is given in Figure 14.

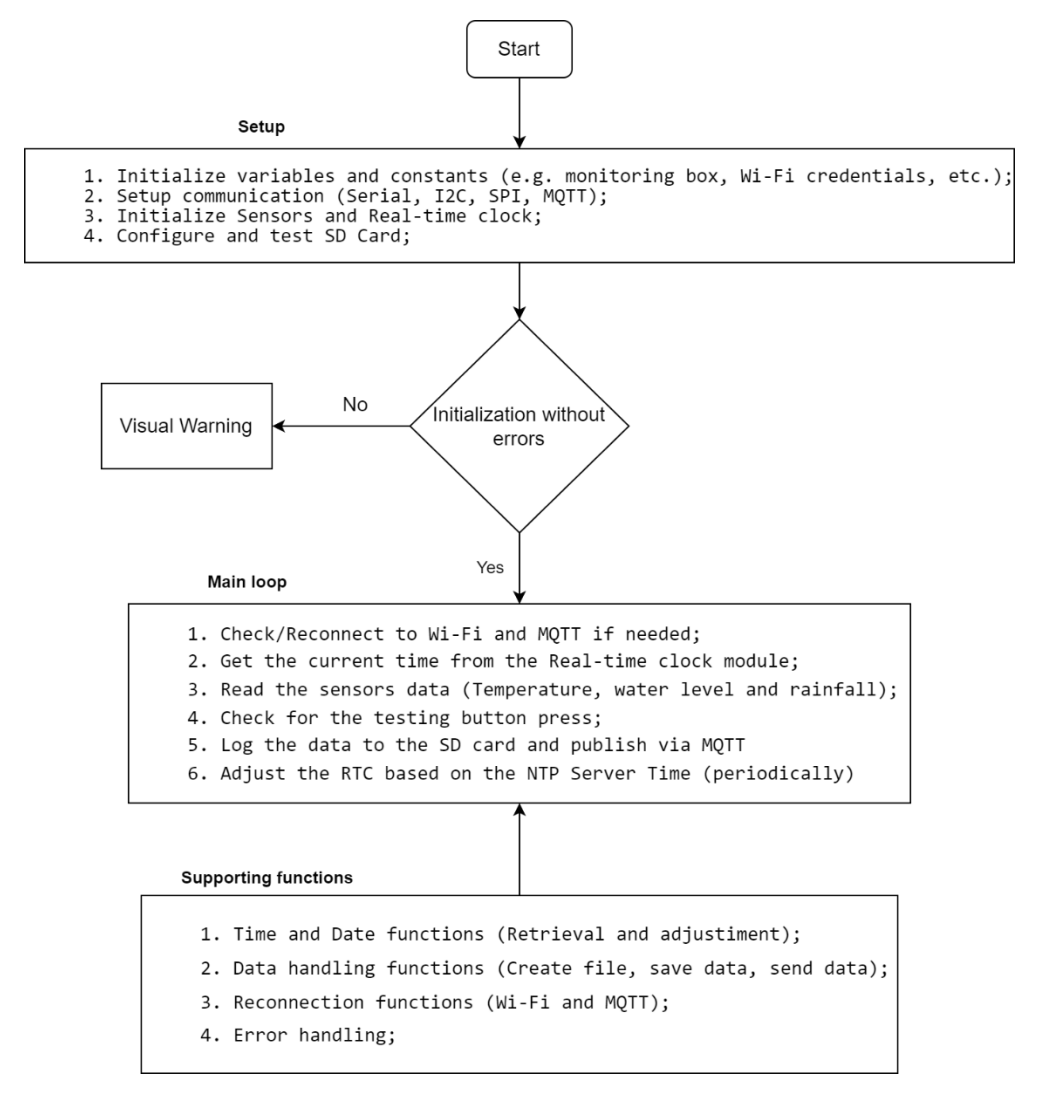


Figure 14: Software flow chart

At initialization, the system enters a loop, continuously checking for Wi-Fi connectivity and reconnecting if necessary. It reads the current time from the real-time clock module and gathers data from various sensors, which monitor parameters like temperature, water level, and rainfall. This information is logged onto an SD card and published over Message Queuing Telemetry Transport (MQTT). Wi-Fi and MQTT connectivity are essential for the system, with reconnection functions to ensure continuous operation. The system also checks for user interaction through a testing button and adjusts the real-time clock periodically based on the Network Time Protocol (NTP) server time to ensure accuracy.

The code includes a setup for temperature sensors, defines the hardware pins used for connections, and provides the calibration factors established for accurate measurements. The pluviometer setup indicates whether the rainfall data will be considered in the system's operation, which is determined by the specific monitoring box. A DS3231 real-time clock manages date and time, and the software includes functions to retrieve and adjust these values as needed.

In the loop function, the software manages the main operational flow, including reconnecting to Wi-Fi and MQTT, retrieving and adjusting the current time, reading sensor data, logging it to the SD card, and publishing it over MQTT. The code also includes setup for an SD card where data is logged and managed through various functions to create, save, and send data files. The software responds to a button press by saving test temperature data to the SD card. Rainfall data collection is conditional, activated only for specific data acquisition boxes, and handled by dedicated functions within the code.

Error handling is provided throughout the code, with visual warnings indicated by LED states and serial print statements informing about operations' success or failure, such as Wi-Fi

connectivity, SD card initialization, and sensor readings. The system is robustly designed to handle various scenarios and maintain operation even during intermittent connectivity or other issues.

The RTM system developed for this study has improved significantly the efficiency and reliability of data collection for monitoring precipitation events at the PP test site. This represents a significant step in automating data retrieval, which traditionally relies on manual collection via USB and proprietary setups that are time-consuming and prone to data loss. Furthermore, RTM allowed faster detection of defective sensors or unreliable readings, reducing system down time and data loss. Another significant RTM advantage was that it enabled timely decisions on whether a precipitation event was significant enough to warrant collecting water quality samples.

The RTM system also enabled real-time synchronization of data elements including rainfall depth, water level, and temperature. This automation minimized time discrepancies between datasets, ensuring a more consistent and accurate reflection of the monitored conditions. Reliability was improved through warning triggers, which sent email alerts whenever sensor readings were implausible or data collection from sensors ceased.

While the 4G router provided connectivity across all devices, maintaining a reliable connection was challenging due to the distance between the monitoring boxes and the router, signal interference from the metal monitoring boxes, and intermittent cellular 4G signal during thunderstorms. A stable connection was achieved by adding a signal repeater to enhance the antenna signals.

Cost-effectiveness was another significant benefit, considering that the RTM system utilized open-source hardware such as the ESP32 microcontroller and various compatible modules for data transmission and storage. This open-source approach resulted in a very cost-effective setup that could be readily implemented at a larger scale, promoting sustainable practices in urban water

management by reducing the financial burden typically associated with proprietary commercial systems.

Finally, the RTM system developed streamlined data transmission and visualization by centralizing all collected data into an InfluxDB database, which fed directly into a Grafana dashboard. This integration provided real-time data visualization, enabling immediate insights into permeable pavement performance, as can be seen in Figure 15. Moreover, this centralized platform can serve as the basis for Digital Twin (DT) applications, facilitating predictive and adaptive stormwater infrastructure management. Data reliability, cost-efficiency, and real-time visualization advancements can contribute to a smarter, more resilient approach to urban stormwater management.

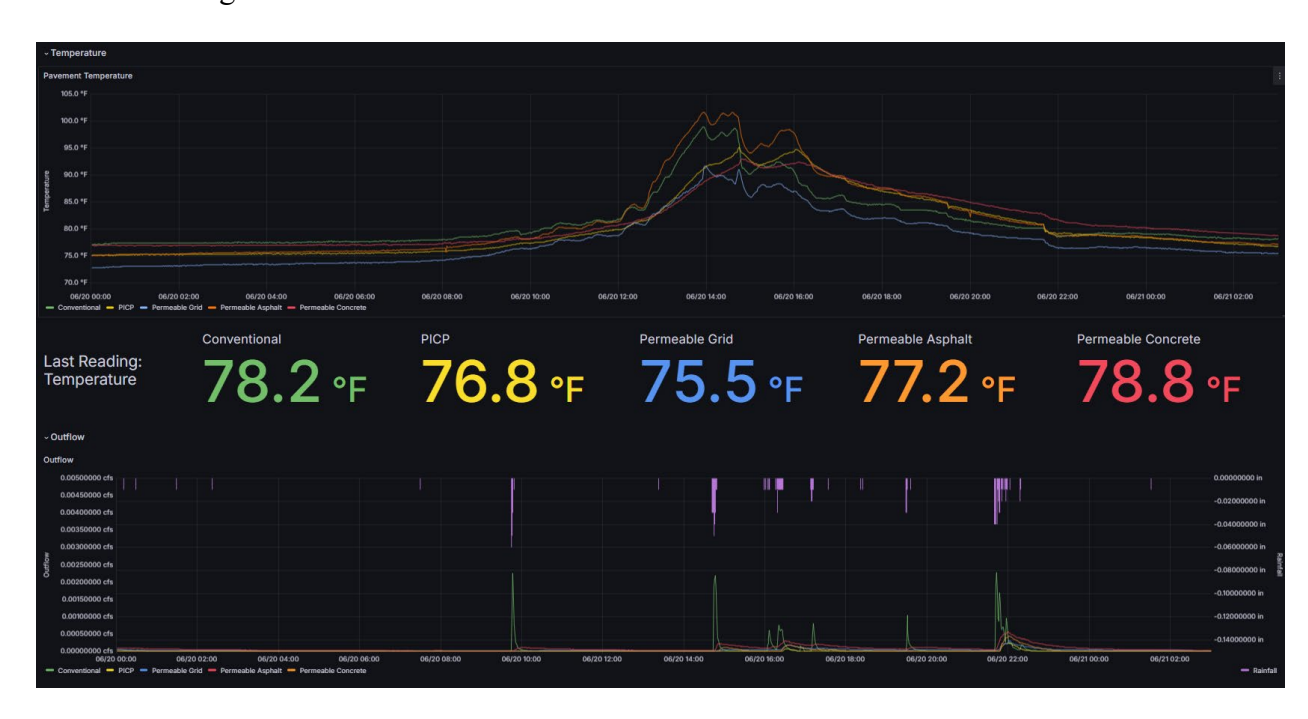


Figure 15: RTM Dashboard: Pavement temperatures are displayed at the top, with real-time hydrograph and precipitation data at the bottom streamlined in real-time after an event

## 3.4 Pavement Temperature Sensors Calibration

The DS18B20 temperature sensors were calibrated and validated in two steps. First, a single-point comparative calibration was used on a laboratory configuration based on the methodology described by Koestoer et al. (2019). Second, the in-situ pavement temperature was compared to the measurements of a hand-held laser sensor.

In the first step, the DS18B20 probes and the reference sensors (Fluke 54-2 B) were subjected to a bath in DI water. The reference probe had a resolution of 0.1°C, a temperature range of -250°C to 400°C, and an accuracy of ±0.05%. The temperature range for the calibration was from 1°C to 55°C. Similarly, the second step compared a laser probe temperature reading with the temperature probe installed at the pavement's bottom of the surface layer to validate the calibration established by the first step. According to Chen et al. (2019), the surface pavement temperature is expected to be higher than at the bottom, where the probes were installed, due to the heat absorption, conduction, and dissipation within the pavement surface layer.

## 3.5 Water Temperature

The rainfall data was combined with pressure transducer data to retrieve water temperature data during the events. For each pavement across all monitored events, the periods with water presence were identified, and the maximum, minimum, average, median, and standard deviation of water temperature during these periods were calculated. The water temperature then, was compared to the pavement surface temperature to determine which pavement has performed better in cooling down the pavement surface without significantly increasing in the water temperature.

#### 3.6 Sampling and Water Quality

Water was sampled from the pavement outflow and analyzed for several parameters. Each pavement's sampling equipment comprised an ISCO 6712 automatic water sampler, 12 glass

bottles containing 950 mL, and a polytetrafluoroethylene (PTFE) suction line. A three-trigger sampling method was employed to capture various rainfall events, including the first flush, small rainfall volume events, and larger rainfall events (Table 8).

Table 8: Three-trigger approach used for water sampling

Sampler Trigger	Condition to collect a sample	Samples
First Flush	Underdrain water level > 0.25 inches for 30 seconds	1
A	Every 5 cubic feet of underdrain outflow	2-6
В	Every 10 cubic feet of underdrain outflow	7-12

The UTSA Environmental Lab facilities were used to analyze:

- Total Suspended Solids (TSS),
- Volatile Suspended Solids (VSS),
- pH,
- Fecal and Non-Fecal Bacteria, and
- Polycyclic Aromatic Hydrocarbons (PAHs),

A commercial laboratory (Alamo Analytical Laboratories) was used for measurements of:

- Metals (i.e., Zinc, Lead, Copper),
- Total Petroleum Hydrocarbons (TPH), and
- Hardness.

The methods, instruments, and test limits are summarized in Table 9.

Table 9: Water quality parameter and analysis methods

Parameter	Units	Method	Instrument	<b>Test Limits</b>
pH	-	Standard Method 4500-H+B	HACH® sensION156	2 to 14
Conductivity	μs/cm	Standard Method 2510 B	HACH® sensION156	0.01 to 1000
Total Suspended Solids (TSS)	mg/L	USEPA Gravimetric Method for water and wastewater of solids, nonfilterable suspended solids	Desiccator, Furnace	NA
Volatile Suspended Solids (VSS)	mg/L	USEPA Gravimetric Method for water and wastewater of solids, nonfilterable suspended solids	Desiccator, Furnace	NA
Bacteria (Total Coliform)	CFU/100 ml	Prepared Agar Plates Method with Membrane Filtration for low-turbidity water	Incubator	NA
Zinc	μg/L			4.5E-7
Lead	μg/L	Acid digestion preparation with ICP M-S	PerkinElmer ELAN DRC-e Spectrometer	7E-8
Copper	μg/L	W.W. 101 111 5	Dies o spoonomous	5E-8
РАН	μg/L	EPA Method 610**	GC/MS	Parameter dependent*
ТРН	mg/L	TCEQ Method 1005	GC/FID	5

^{*}Table 1 of EPA Method 610 **Due to limitation on the sample volume, the PAH analysis was done using 500mL instead of 1L as suggested by the EPA 610

#### **CHAPTER FOUR: METHODOLOGY**

### 4.1 Water Quantity Metrics

The PPs were compared with the conventional (i.e., impermeable) asphalt concrete pavement and between each other across all the parameters monitored. For water quantity, the peak flow reduction was calculated as:

$$Peak \ Reduciton = \frac{Q_{peak,perm.}}{Q_{peak,convent.}} \tag{1}$$

where,  $Q_{peak,perm.}$  is the peak flow of the permeable pavement and  $Q_{peak,convent.}$  is the CP peak flow. The Peak Delay (minutes) was defined as the time difference between the peak flow for the permeable pavements and the CP, expressed as:

$$Peak \ Delay = Q_{peak,perm.} - Q_{peak,convent.}$$
 (2)

Finally, the percent difference between the monitored rainfall volume ( $Volume_{rainfall}$ ) and the volume of water that drains out of the pavement ( $Volume_{outflow,pav.}$ ) was defined as Storage, expressed as:

$$Storage = \frac{Volume_{rainfall} - Volume_{outflow,pav.}}{Volume_{rainfall}} \times 100$$
 (3)

#### **4.2** Infiltration Rate

A total of seven infiltration tests were conducted to ensure that the permeability of the PP surfaces did not significantly change. The tests were carried out using a simple infiltration test developed by Winston et al. (2016). The method uses a single ring falling head and has similar results to the single-ring constant-head standard method (ASTM C1701 and C1781) but requires 73% less time, enabling data collection of data on three defined points on each pavement on the same day. The apparatus used on the test consists of a wooden square frame with a side length of 0.56 m and inner surface of 0.32 m². Plumber's putty was placed around its inner perimeter to

prevent sideways water percolation (Figure 16). The water level drop inside the box enclosure allowed estimating the permeability of the surface.



Figure 16: Simple infiltration test apparatus

For each permeable pavement (PP), three locations were selected for the infiltration tests: the top-left corner, the center, and the bottom-right corner of the pavement (locations 1 to three respectively). A minimum distance of 1 foot from the curbside was maintained to ensure proper placement of the apparatus and to minimize potential lateral flow interference caused by the proximity to the curb. This helped prevent curbside effects from influencing infiltration measurements and ensured more representative results for the pavement surface. To maintain consistency, the same locations were used for each PP test throughout the monitoring period. Permeability measurements were obtained for all PPs except the PGr pavement that drained too quickly to allow meaningful observations of water level drop (i.e., its voids were too high and the surface too uneven to allow proper sealing around the box).

# 4.3 Water Quality Metrics

Water quality was analyzed in terms of the Event Mean Concentration (EMC) of pollutants, expressed as the mean of the samples obtained from each rain event:

$$EMC = \frac{\sum_{i=1}^{n} V_i C_i}{\sum_{i=1}^{n} V_i}$$
 (4)

where  $V_i$  is the volume of flow during the period i,  $C_i$  is the concentration associated with the period i and n is the total number of samples taken during an event following the three-trigger routine described in Table 8.

The total load per event was also used to characterize the pollutants in each pavement. Since pH and conductivity were not expressed in terms of concentration, an average of the samples was used to summarize the events. The Total Load of each pollutant was calculated using:

$$Total \ Load = \sum_{i=1}^{n} V_i C_i \tag{5}$$

## 4.4 Pavement Usage

Pavement usage of each parking lot is important in ascertaining the effect of cars parked on the PP surfaces. Pavement usage detection was automated via cameras, and custom software was developed for this purpose. Two video digital cameras were installed near the roof of the park pavilion, one aimed towards the PICP and the PGr pavements and the other towards the PA and PC pavements (Figure 17). The video was recorded on a digital recorder located at the site and retrieved manually at bi-weekly intervals.



Figure 17: Digital camera installation at the CSRP pavilion for monitoring parking lot usage

The vehicle detection algorithm is shown in Figure 18. The first step in the pavement usage algorithm was to process the digital video to retrieve still images at 5-minute time increments. This interval was selected based on the assumption that cars are unlikely to remain parked for less than 5 minutes, ensuring minimal loss of relevant information about vehicle activity. By aggregating the video into discrete images at 5-minute intervals, the computational burden was significantly reduced, enabling efficient processing and analysis. Image pre-processing involved cropping and rotating the images to isolate the specific pavement areas of interest, which minimized interference from cars outside the targeted region. This pre-processing step was iteratively performed along with the automatic car detection and calibrated manually, evaluating the results and changing the target area.

The car counting process employed the YOLOv5 (You Only Look Once Version 5) object detection model, which is based on a convolutional neural network. YOLO is a widely used tool in fields such as surveillance, autonomous driving, and industrial automation due to its ability to detect multiple objects in real time. The model utilized pre-trained weights from the COCO dataset, which includes 80 object classes, such as cars and trucks. Figure 16 shows a flow chart illustrating the steps of the automated car detection system.

The results of the car counts in each parking lot were calibrated using visual counts. The accuracy in counting the number of cars in each parking lot was affected by several factors:

- Obstruction in the line of sight from trees or instrumentation boxes and,
- Overlap of car images when one was parked behind another, making the location of a partially or entirely hidden car unclear.

To improve accuracy, three filters were applied to refine the results: an area box size filter, a centroid distance filter to eliminate overlapping detections, and a containment filter to remove

boxes fully contained within others. The parameters for these filters were manually calibrated for each pavement and camera sight line.

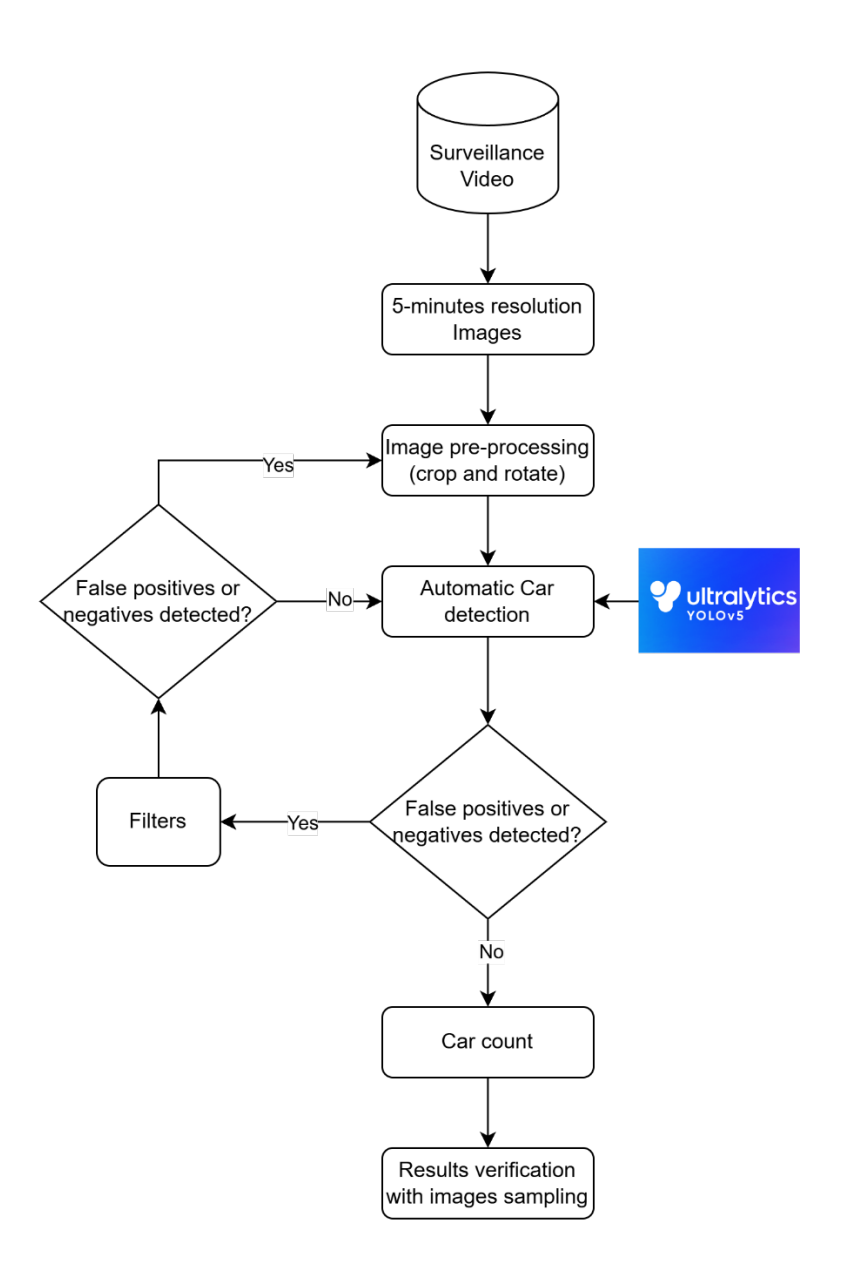


Figure 18: Flow chart of automated car detection and counting algorithm

A ground truth dataset comprising 11 days was selected to calibrate and validate the algorithm's performance in counting cars parked on the pavement. The selected days, detailed in

Table 10, spanned different seasons and days of the week to account for variations in lighting conditions and pavement usage. Observations were based on manual counts of cars parked per parking lot using static images from video recordings. Six randomly selected days were used to calibrate the filters, while the remaining five days were reserved for validation.

Table 10: Dates with the observed data for the ground truth

5/28/2023*	2/10/2024*
6/1/2023	3/1/2024
6/9/2023	3/20/2024
8/19/2023	3/26/2024*
9/5/2023*	4/22/2024*
10/25/2023*	

*Used for calibration

The calibration and validation steps were evaluated based on accuracy, representing the percentage of correct counts from the algorithm compared to the ground truth in the percentage of the total number of 5-minute images evaluated. Figure 19 illustrates examples of both accurate and inaccurate detections for the CP and PC pavements. The algorithm generates images with bounding boxes, the probability of an object being a car, and the box area in pixels. In Figure 19a, all cars are correctly counted, even when a tree partially obscures one. Conversely, Figure 19b demonstrates an error where a car parked on the PA lot is improperly counted. In this instance, the minimum box area filter failed to exclude cars outside the CP. Figure 19c shows a correct count for the PC pavement, where the filters effectively excluded cars outside the pavement. However, Figure 19d highlights an error where an open car door was mistakenly counted as a car on the PC pavement.

After calibration/validation, the algorithm was used to establish Parking Lot Occupancy, defined as the cumulative number of car minutes per day for each parking lot. The Parking Lot Occupancy was then aggregated between rainfall events, and a Shapiro-Wilk test was performed

to assess data normality. Since the data was non-normal, a Spearman correlation analysis was conducted to evaluate the relationship between Parking Lot Occupancy and TSS. However, it was not possible to relate the Parking Lot Occupancy to other auto-related pollutants (e.g., PAHs) due to their low concentrations.



Figure 19: Examples of the imaging system of car counting by parking lot area

# 4.5 Statistical Analysis

## 4.5.1 Water Quality

The water quality statistical analysis included a summary of events, pair-wise comparisons, and correlation analysis. The results were summarized in terms of the medians, averages, and standard deviations of EMC and the Total Load of pollutants.

A Shapiro-Wilk test was first applied for the pair-wise analysis to evaluate data normality. Where the data followed a normal distribution, a parametric t-test was conducted. If the normality assumption was not satisfied, the non-parametric Wilcoxon signed-rank test was used instead. This

approach assessed pavement performance, compared the CP with PPs, and evaluated differences between the PP types.

Similar to the pair-wise analysis, the correlation analysis was performed with a parametric Pearson's test if the data followed a normal distribution, or a non-parametric Spearman's test otherwise. These statistical tests were conducted for each pavement, using pollutant-to-pollutant and water quantity-to-pollutant relations. A confidence level of 95% was used (statistical significance for p-value<0.05). The pollutant-to-pollutant correlation indicates the potential relationship between pollutants and helps to identify co-pollutant production.

## 4.5.2 Water Quantity

Regarding the water quantity, a correlation analysis was performed between water quality parameters and water quantity indicators, including rainfall depth, event duration, rainfall intensity, antecedent dry period, peak flow, and runoff volume, to explore potential relationships that may influence pollutant concentrations and transport. The Antecedent Dry Period (ADP) was defined as the number of days without outflow from any of the permeable pavements.

## 4.5.3 Pavement Temperature

The temperatures from the four PPs and the CP were aggregated into daily maxima, average, and minima. The aggregation reduced the effect of autocorrelation and day/night temperature fluctuations. The Shapiro-Wilk test was used to assess data normality. If the pavement temperature data met the normality assumption, a parametric t-test pairwise. Otherwise, the non-parametric Wilcoxon signed-rank test was employed for pairwise comparisons.

In addition to reporting p-values, the differences in median pavement temperatures were also calculated to highlight the thermal performance of each pavement type. This approach complemented the statistical tests by offering a practical measure of temperature variation between

pavements, allowing for a more direct interpretation of how each pavement type performs in heat retention or dissipation.

#### CHAPTER FIVE: RESULTS AND DISCUSSION

This chapter outlines the results of the permeable pavement monitoring and statistical testing for water quantity, water quality, and temperature. It directly compares the performance of the four permeable pavement types tested against the conventional (i.e., impermeable) asphalt concrete pavement.

# **5.1** Water Quantity

The post-construction monitoring included eleven rainfall events from August 2023 to May 2024. The key rainfall characteristics are summarized in Table 11. Total rainfall depths ranged from 0.48 inches to 4.5 inches. Rainfall durations varied between 85 minutes and 2,080 minutes (34.8 hrs). Maximum intensities ranged from 0.96 inches per hour to 5.16 inches per hour. The monitored events differed in terms of rainfall depth, duration, and maximum intensity, allowing comparisons between the PP types.

Table 11: Precipitation events monitored post-construction

No.	<b>Event Date</b>	Total Rainfall Depth (in)	Rainfall Duration (min)	Maximum Intensity (in/hr)	Antecedent Dry Period (days)
1	08/22/2023	0.62	295	5.16	61
2	10/05/2023	1.05	485	1.8	43
3	10/25/2023	0.97	1140	0.96	20
4	11/09/2023	0.72	530	1.08	10
5	12/23/2023	0.65	680	1.2	7
6	01/21/2024	4.5	2080	2.16	13
7	02/02/2024	1.18	865	1.32	8
8	04/09/2024	0.71	160	2.04	48
9	04/20/2024	0.56	160	2.16	11
10	04/28/2024	1.65	85	2.64	7
11	05/13/2024	0.48	115	2.16	15

The ADP is an important factor in water quality analysis because it represents the time during which pollutants can accumulate on the surface of pavements between rainfall events. It was calculated as the time difference between the start of the observed outflow in the current event and the last outflow recorded from any of the permeable pavements during the previous event. ADPs ranged from 7 to 61 days.

Figure 20 illustrates the flow response time series of selected rainfall events by pavement type. It shows significant differences between the CP and PPs. In all events, the CP produced the highest peak flows with the shortest response times. In contrast, the PPs, particularly the grid and the PICP, reduced peak flows and delayed runoff significantly. These patterns illustrate the hydrological response of the PPs versus time in response to precipitation events. They clearly demonstrate the benefits of PPs in managing stormwater by reducing runoff volumes, delaying peak flows, and increasing water storage. Appendix C provides a complete record of these figures for all the events.

The water quantity performance of the four PPs was analyzed with reference to the CP utilizing three parameters, namely the peak flow reduction, the peak flow delay, and the water storage ratio, as defined earlier (Equations 1, 2, and 3, resp.). Table 12 shows the average and the standard deviation (STD) of these parameters. It suggests that the PGr pavement exhibited the best overall hydrological performance, producing the highest peak flow reduction, highest delay, and highest water storage. This was expected, given its high air voids and surface layer permeability, yielding the highest infiltration rates, as documented later. The PICP and the PA also demonstrated excellent hydrologic performance for all three metrics. The hydrologic performance of the PC pavement was slightly inferior compared to the other three PPs. Overall, all four PPs exhibited

significant stormwater management benefits compared to the CP, by drastically reducing precipitation runoff volumes and delaying peak flows.

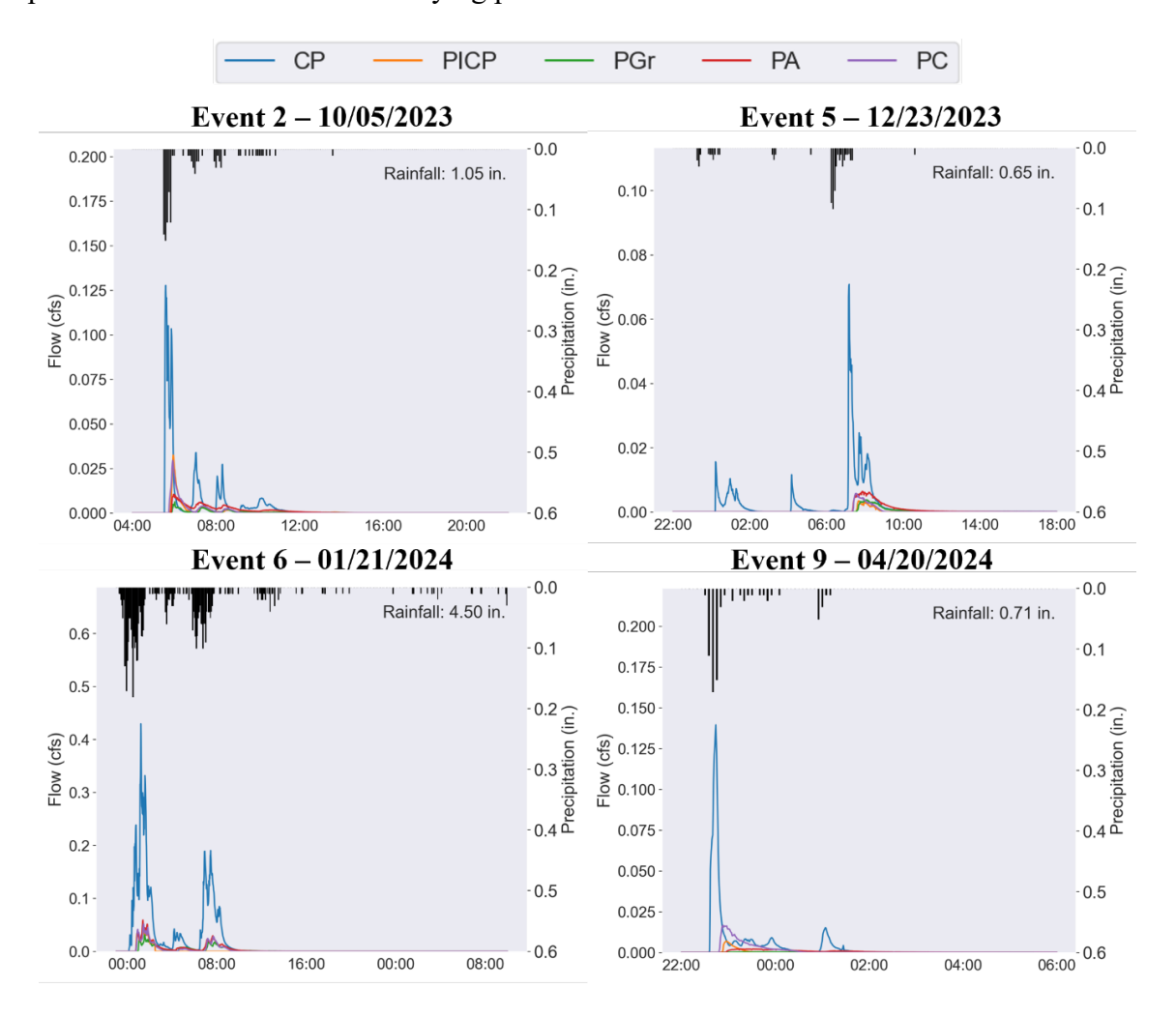


Figure 20: Rainfall and flow response time series for selected water quantity events.

Table 12: Permeable pavements peak flow reduction, delay, and water storage

Pavement	Average peak flow reduction*	Peak flow reduction STD	Average peak flow delay (min)*	Peak flow delay STD (min)	Average volume reduction (%)**	Volume Reduction STD (%)**
PICP	89.9%	8.56%	20	15	82.3	13.2
PGr	94.7%	5.74%	33	21	85.7	9.4
PA	90.1%	8.48%	24	18	64.4	12
PC	84.9%	9.80%	16	14	71.6	19.6

^{*}Relative to the CP; **Outflow reduction from rainfall

# 5.2 Water Quality

#### 5.2.1 TSS and VSS

The analysis of TSS and VSS in the water outflow from the pavements allowed direct comparison between the PPs and the CP (i.e., impermeable) pavement, as well as between the PP types. Figure 21 shows EMC (Equation 4) boxplots for TSS and VSS concentrations. Table 13 summarizes concentration statistics for TSS and VSS, as well as for Total Load (Equation 5).

The CP exhibited the highest median and mean EMC values for TSS, and the highest variability in these concentration measures between rainfall events. Comparison between PPs reveals that the PICP performed best, exhibiting the lowest median EMC for both TSS and VSS. The PGr pavement exhibited slightly higher median EMCs, while the PA and the PC pavements exhibited higher EMC variability. The PA, in particular, had an elevated mean EMC compared to its median, caused by several outlier observations (Figure 21). The PC also had slightly higher mean TSS concentrations and a wider inter-quartile range compared to the other PPs. Overall, the PICP produced the lowest and most consistent TSS and VSS mean concentrations compared to the other PP designs. This data highlights the benefit of PPs in reducing the concentration of TSS and VSS from the levels generated by impermeable pavements.

Pairwise statistical comparisons of EMCs between pavement types further supported these findings (Figure 22). For TSS, the CP showed significantly higher concentrations than all permeable pavement types. PICP, PGr, and PA TSS concentrations did not differ significantly, while the PC exhibited significantly higher TSS concentrations than the other PPs.

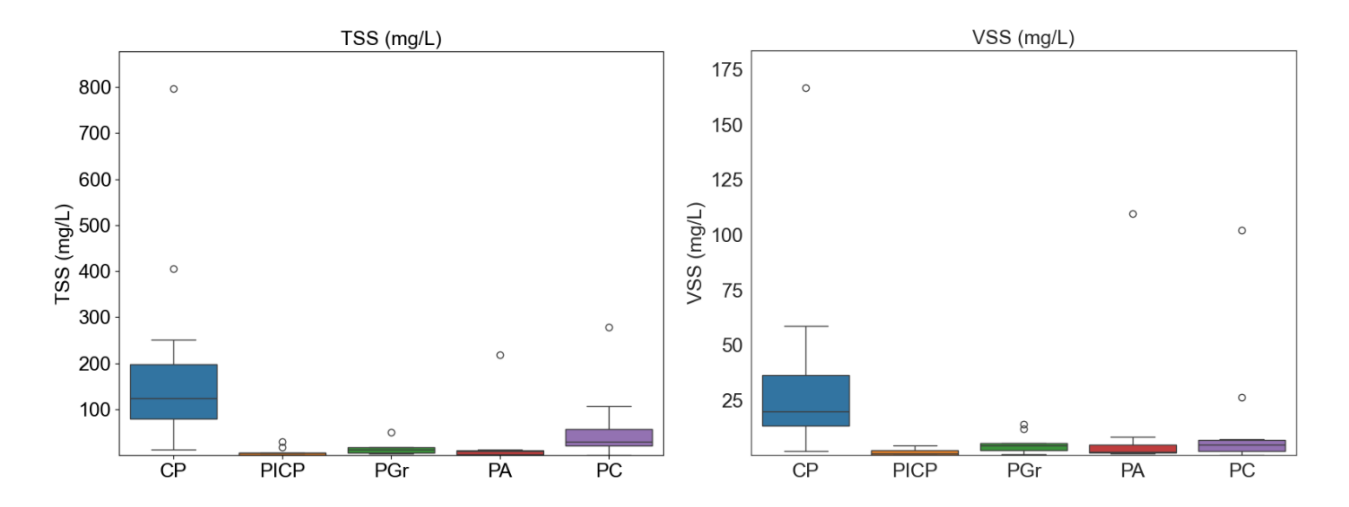


Figure 21: EMC boxplots for TSS and VSS by pavement type.

Table 13: TSS and VSS Event Mean Concentrations (EMC) and loads.

Water Quality Parameter	Pavement Type	EMC Median (mg/L)	EMC Mean (mg/L)	EMC STD (mg/L)	Total Load Mean (Kg)	Total Load STD (Kg)
	CP	123.89	197.30	226.42	0.807	0.606
Total	PICP	5.93	8.00	9.82	0.015	0.027
Suspended Solids	PGr	11.89	14.56	13.43	0.013	0.016
(TSS)	PA	8.34	25.93	64.12	0.071	0.138
(155)	PC	29.50	59.29	78.50	0.070	0.082
V-1-4:1-	CP	19.77	35.83	46.30	0.142	0.128
Volatile	PICP	0.91	1.54	1.74	0.002	0.003
Suspended Solids (VSS)	PGr	4.33	5.20	4.53	0.005	0.004
	PA	1.47	12.49	32.40	0.029	0.067
( v SS)	PC	4.81	14.62	29.91	0.011	0.014

Figure 22 shows that the CP exhibited significantly higher VSS concentrations than the PPs, (i.e., higher volatile matter concentrations and concentration variability). This can be attributed to its impervious surface, which prevented water infiltration and led to increased surface runoff and organic material inclusion. Comparing PPs revealed that the PICP showed significantly lower levels of VSS concentration compared to the PGr pavement. The PA and the PC pavements exhibited more variability. This was due to outlier concentration observations for some events,

likely caused by accumulated soil or dust on these two permeable pavement types. Overall, these findings confirm that permeable pavements effectively reduce TSS and VSS levels.

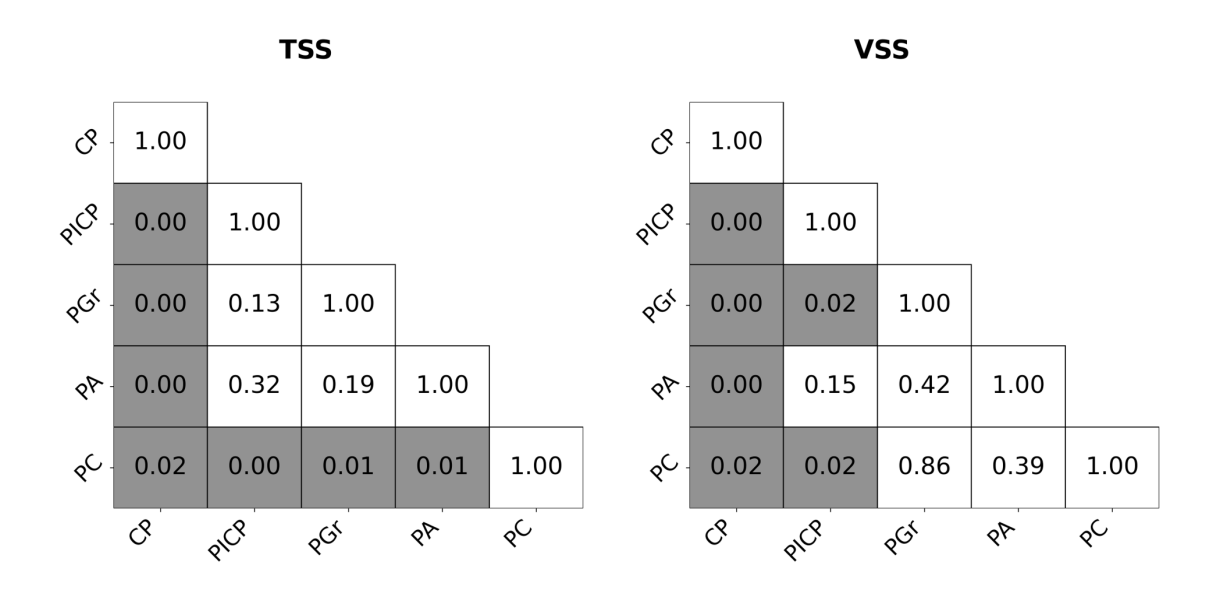


Figure 22: Pavements pairwise comparisons for TSS and VSS using the Wilcoxon signed-rank test; Shaded cells indicate p-values < 0.05 (i.e., significant differences at 95% confidence)

## 5.2.2 Fecal and Non-Fecal Bacteria

The fecal and non-fecal coliform bacteria analysis for the pavement types showed distinct bacterial presence and variability patterns. Their logarithmic EMC box plots, in terms of colony-forming units/100ml (cfu/100ml), are shown in Figure 23. The statistics for the EMC concentration of non-fecal and fecal bacteria and the associated loads are summarized in Table 14. The data suggests that the CP yields the highest median EMCs for non-fecal coliform bacteria. However, this is not the case for their mean concentrations. Similar discrepancies were observed for the fecal bacteria concentrations; the PA exhibited the highest median EMC, but the PGr yielded the highest mean EMC. For fecal bacteria, the large differences between mean and median EMCs and the relatively large STD values observed can be attributed to the random contamination

possible from external sources, such as wildlife waste. The high mean EMC of fecal bacteria from the PGr could be the result of animal waste adhering to its rougher surface. In contrast, the PICP with the smoothest surface, exhibited the lowest mean EMC values for fecal bacteria.

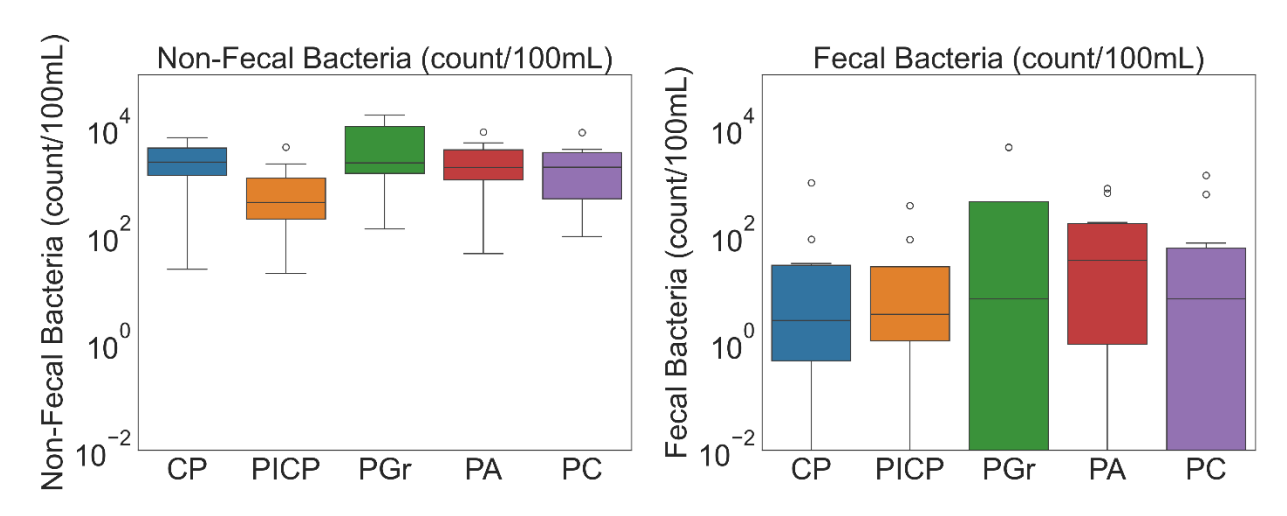


Figure 23: EMC boxplot per pavement for bacteria (Non-Fecal and Fecal).

Table 14: Non-Fecal and Fecal Bacteria Event Mean Concentration and loads

Water Quality Parameter	Pavement	Median EMC (cfu/100ml)	Mean EMC (cfu/100ml)	EMC STD (cfu/100ml)	Average Load (cfu x 10 ⁸ )	Load STD (cfu x 108)	Total Load (cfu x 10 ⁸ )
	CP	2345.26	2857.97	2335.97	1.26	1.34	13.82
N. D. 1	PICP	416.22	1080.02	1527.12	0.13	0.21	1.21
Non-Fecal Bacteria	PGr	2268.79	6394.31	6841.90	0.46	0.58	4.63
Bacteria	PA	1869.82	2787.25	2650.37	0.47	0.53	5.12
	PC	1896.43	2497.28	2534.94	0.25	0.31	2.76
	CP	2.63	110.41	299.61	0.02	0.05	0.26
Fecal	PICP	3.41	57.67	126.22	0.01	0.02	0.06
Coliform	PGr	6.61	1037.30	1934.51	0.09	0.18	0.9
Bacteria	PA	34.48	175.69	277.87	0.06	0.1	0.67
	PC	6.62	200.90	434.31	0.02	0.05	0.22

The pairwise statistical comparisons established significant differences in EMCs for non-fecal and fecal bacteria between pavement surface types (Figure 24). This data revealed that there were no statistically significant differences between the CP and the PPs for either non-fecal and fecal EMCs. On the other hand, the PICP pavement was significantly better in reducing non-fecal

bacteria concentrations than the PGr. No significant statistical difference was found for Fecal Bacteria.

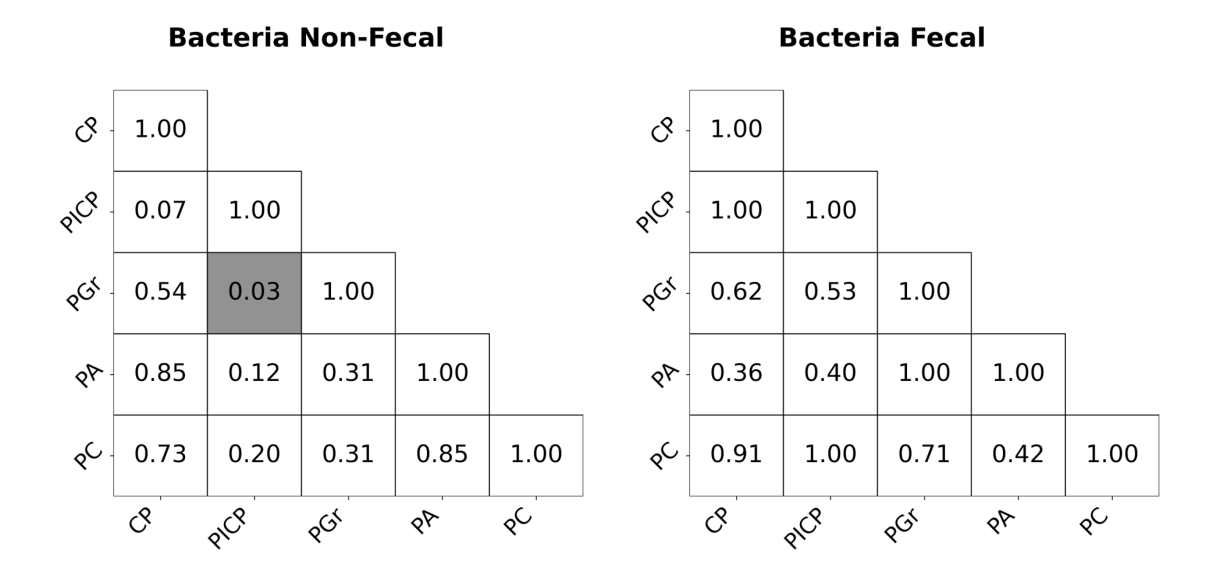


Figure 24: Pavements pairwise comparison with Wilcoxon signed-rank test for Non-Fecal and Fecal Bacteria.

# 5.2.3 Metals – Zinc, Copper and Lead

The presence of metals such as Zinc, Copper and Lead in water runoff are associated with anthropogenic activities, such as the presence of cars. Zinc has been associated with automotive brakes, (Davis et al., 2001; Legret & Pagotto, 1999; McKenzie et al., 2009), Copper has been associated with automotive tires and brakes (McKenzie et al., 2009; Sansalone & Buchberger, 1997), while Lead has been associated with paints and wheel balancing weights (Adachi & Tainosho, 2004).

The analysis of metals highlights the differences in runoff contamination between the CP and the PPs due to the presence of parked cars. The analysis was conducted using an ICP-MS following EPA Method 200.7, which had a Practical Quantitation Limit (PQL) of 10 µg/L for all the metals. No quantifiable concentrations were measured for all events, reflecting low concentrations of these metals in the water samples. Specifically, none of the events produced quantifiable Lead

measurements, and hence, Lead is not discussed further. The number of events that produced quantifiable Zinc and Copper measurements are summarized in Table 15. Table 15 also summarizes statistics for EMC (Equation 4) and Total Load (Equation 5) for Copper and Zinc.

Table 15: Metal EMC and Load Statistics

Water Quality Parameter	Pavement	Sample size*	Median EMC (μg/L)	Mean EMC (μg/L)	EMC STD (µg/L)	Average Load (mg)	Load STD (mg)	Total Load (mg)
	CP	0	ı	ı	ı	ı	-	-
T . 4 . 1	PICP	1	0.5	0.5	ı	0.57	1.60	5.10
Total Copper	PGr	1	0.08	0.08	ı	0.00	0.01	0.02
Соррег	PA	2	0.03	0.03	ı	0.03	0.10	0.38
	PC	5	8.1	10.2	7.9	1.58	1.99	17.35
	CP	8	5.9	13.2	25.8	26.44	58.20	290.84
Total	PICP	2	17.7	17.7	6.0	3.18	8.15	28.59
Zinc	PGr	6	4.4	6.1	6.7	0.44	0.72	4.46
	PA	4	1.5	5.0	7.9	1.43	3.97	15.74
	PC	5	9.7	28.0	46.6	5.41	14.77	59.56

^{*}Quantifiable samples considering the method PQL

Table 15 suggests that the CP yielded water runoff with the highest number of Zinc quantifiable samples (i.e., sample size) and the highest Zinc Total Load compared to the PPs. Comparing Zinc Total Load amongst the PPs, suggests that the PC and the PICP yielded the highest Total Loads. Assuming comparable car usage for all five parking lots, it appears that the PPs retain some of the Zinc being deposited by the parked cars. The degree of Zinc retention is higher for the permeable PA and the PGr pavements. The likely reason is differences in void structure and material surface chemistry.

For Copper, the PC showed the highest mean EMC and Total Load among all pavement types. This can be attributed to factors related to the material properties and pavement structure. Unlike the CP, which is entirely impermeable, the PC pavement has interconnected voids designed to allow water infiltration. The porous structure may retain and accumulate metals within its matrix.

Over time, the metals may bind to the surface of the concrete or become trapped within its pore spaces, resulting in a lower concentration of metals being released during runoff events.

It is important to note that the concentrations of metals, including Zinc and Copper, are still very low across all pavement types. While PC showed higher metal accumulation in some cases, the overall concentration of Zinc and Copper remained typically below detection limits. This suggests that while differences in metal retention exist between the pavement types analyzed, the absolute concentration of metals in runoff is not a significant concern.

#### 5.2.4 Hardness

The hardness analysis of the water runoff revealed distinct differences in mineral concentrations between pavement types (Figure 25). The PA and PGr pavements exhibited higher concentrations than the CP, suggesting that these pavement materials may contribute to the dissolved mineral content, particularly calcium and magnesium. Table 16 summarizes hardness EMC and Total Load statistics. It shows that the PA had the highest mean EMC and Total Load values compared to all other pavement types, which may be attributed to material composition. This can be attributed to its porous nature that allows for longer water retention, which may promote the dissolution and transport of minerals. In contrast, the PC and the PGr pavements demonstrated lower hardness concentrations than the CP (Figure 25). The lower hardness in the PC is likely due to its alkaline nature, which can act as a buffer, preventing the release of additional minerals. The high infiltration rates of concrete reduce surface runoff and limit the transport of hardness-inducing minerals. Similarly, the PGr pavement, which often incorporates gravel or plastic materials, facilitated better infiltration, resulting in lower mineral accumulation in the runoff compared to the CP.

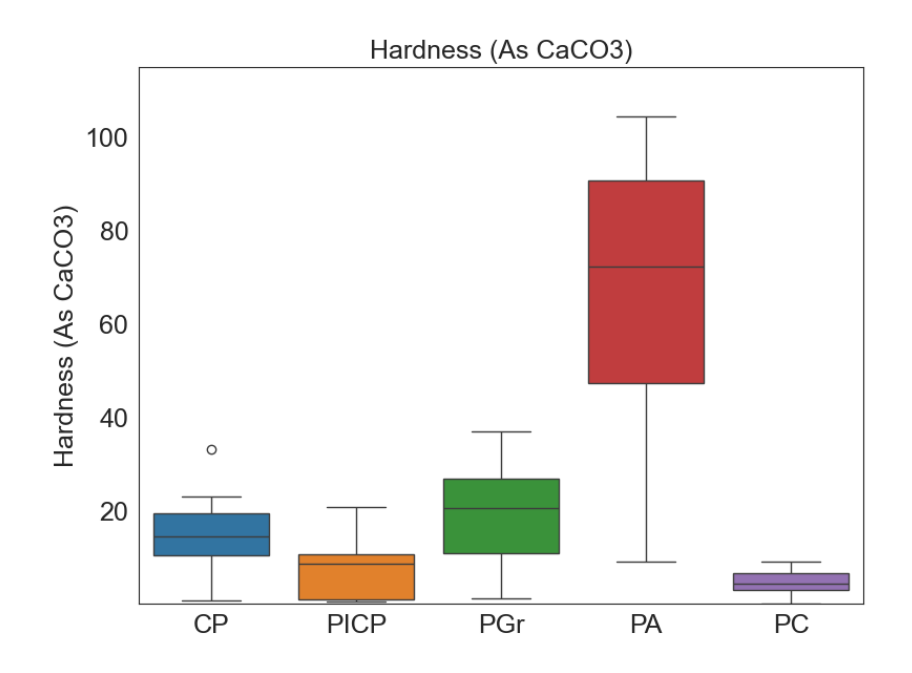


Figure 25: EMC boxplot per pavement for Hardness as CaCO3.

Table 16: Hardness (CaCO₃) EMC and Load Statistics

Water Quality Parameter	Pavement	Median EMC (mg/L)	Mean EMC (mg/L)	EMC STD (mg/L)	Average Load (g)	Load STD (g)	Total Load (g)
	CP	14.52	15.35	8.68	67.96	24.66	747.54
TT 1	PICP	8.66	8.29	6.73	9.78	9.03	88.02
Hardness (CoCO)	PGr	20.62	19.15	12.16	12.74	11.26	127.40
(CaCO ₃ )	PA	72.34	65.80	33.57	116.69	57.82	1283.61
	PC	4.48	4.61	2.91	6.26	7.50	68.91

Pairwise statistical analysis (Figure 26) showed significant differences between PA and all the other pavement types (p-values < 0.05). The PGr and the PC also differed significantly from the CP, with lower hardness concentrations, particularly in comparison to the PA. The PICP, while generally showing lower hardness levels than the PA, also differed significantly from both the PGr and the PA, indicating better performance in reducing dissolved mineral content.

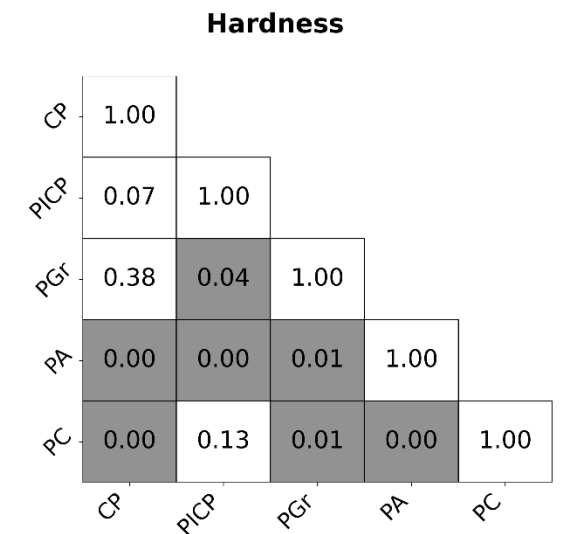


Figure 26: Pavements pairwise comparison with Wilcoxon signed-rank test for Hardness.

Overall, the results indicate that while the PA contributes to higher hardness levels in the runoff, the PGr and the PC are more effective in reducing mineral content than the CP. These findings suggest that material composition and the ability of permeable pavements to promote infiltration play critical roles in controlling the release and transport of dissolved minerals in urban runoff.

#### 5.2.5 pH

The pH analysis of water runoff revealed significant differences between pavement types. The highest pH value was for the runoff from the PC pavement (Figure 27). Its mean pH was 10.10, suggesting significantly more alkaline water than that generated by all other pavement types. This elevated pH can contribute to the precipitation of metals such as copper and zinc, effectively reducing their bioavailability and environmental impact, even if higher concentrations of these metals are present in runoff. The highly alkaline nature of Permeable Concrete suggests that it can buffer metal mobility. This may explain why higher metal loads are observed but in less harmful forms due to decreased solubility. Table 17 summarizes the pH statistics.

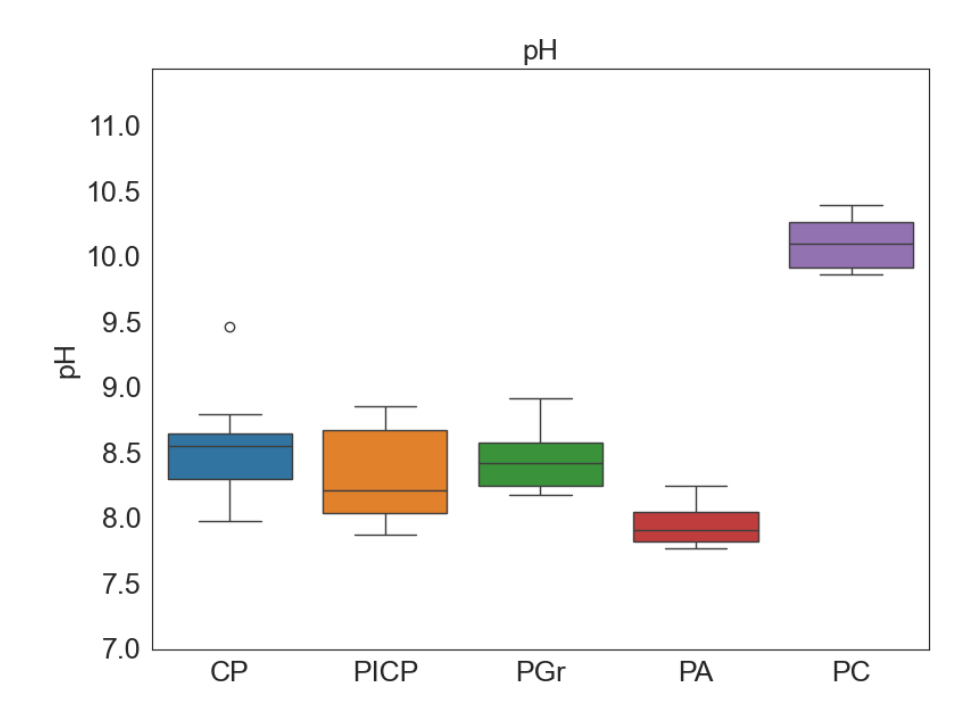


Figure 27: EMC boxplot per pavement for pH.

By comparison, the CP, PGr and PICP pavements yielded slightly alkaline runoff with pH values, ranging from 8.21 to 8.55. While these values are within a range that can reduce metal solubility, they are significantly lower than those for the PC pavement. The PA pavement yielded runoff with a pH value of 7.95, which could also lead to increased metal solubility and bioavailability, thus potentially having a greater environmental impact from metals in the stormwater runoff.

Table 17: Water runoff pH statistics

Water Quality Parameter	Pavement	Median	Mean	STD
	CP	8.55	8.53	0.39
	PICP	8.21	8.31	0.36
рН	PGr	8.42	8.45	0.24
	PA	7.90	7.95	0.16
	PC	10.10	10.10	0.21

The pairwise statistical analysis of the pH data is shown in Figure 28. It confirms that there are significant differences in pH for the PC pavement and all other pavement types (i.e., p-values < 0.01). The PICP also showed significantly lower pH values compared to the PA and the PC pavements. The lower pH of the PA suggests that it may be less effective in reducing metal solubility compared to the other permeable systems.

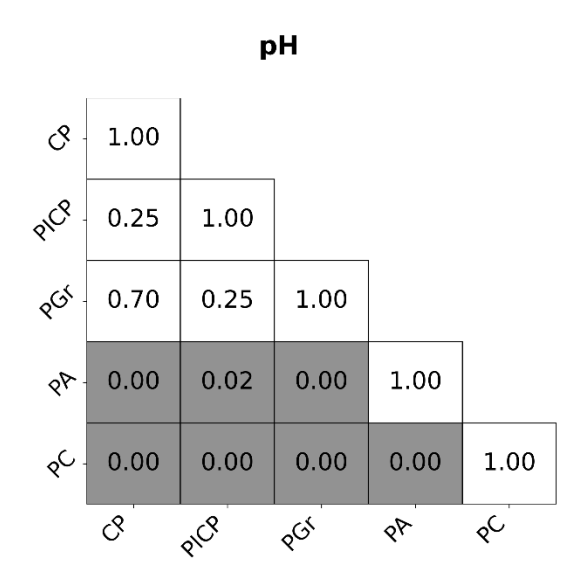


Figure 28: Pavement water runoff pH pairwise comparison with Wilcoxon signed-rank test.

5.2.6 Conductivity

Analysis of the electric conductivity of water runoff revealed significant differences between pavement types (Figure 29). The water runoff from the PC pavement yielded the highest mean conductivity of 579.82 µS/cm. As a result, the PC pavement may release more dissolved ions into runoff, possibly due to its alkaline nature and the materials used in its construction. All PPs showed higher conductivity values than the CP and hence, contribute more to the dissolved ion content of runoff. Table 18 summarizes conductivity statistics for all pavement types.

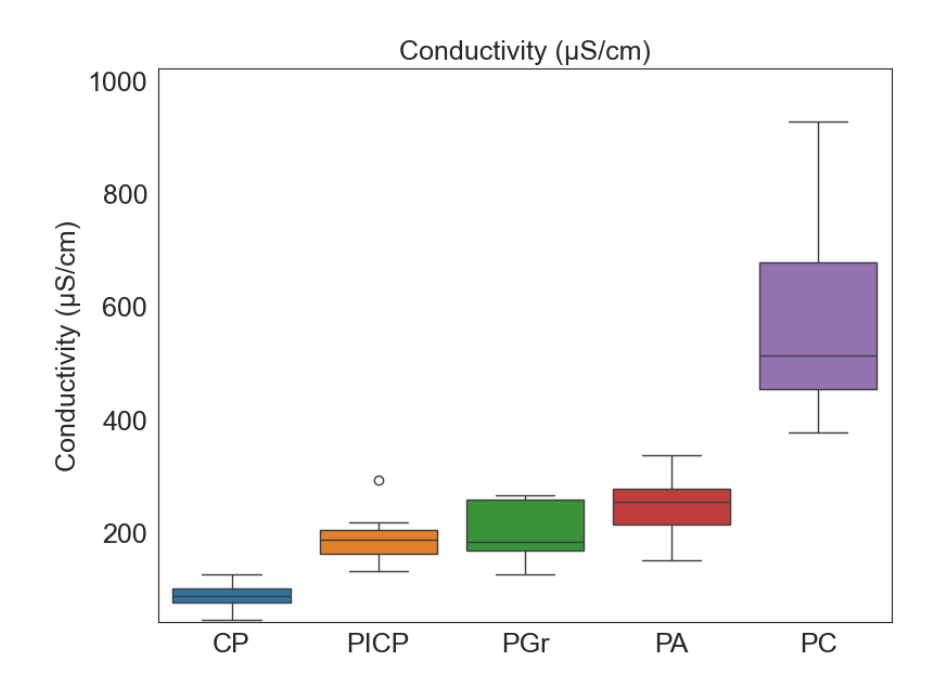


Figure 29: Electrical conductivity boxplots.

Table 18: Electric conductivity statistics

Water Quality Parameter	Pavement	Median	Mean	STD
	СР	89.09	90.08	23.80
Conductivity (µS/cm)	PICP	188.50	192.56	46.62
	PGr	185.81	202.97	53.48
	PA	255.36	248.27	57.86
	PC	514.75	579.82	188.74

Pairwise comparisons for conductivity are shown in Figure 30. They confirm significant differences between the CP and all permeable pavements (i.e., p-values < 0.01). Also, the PC exhibited significantly higher conductivity than the other permeable pavements, indicating a greater contribution to dissolved ion transport in runoff. These findings suggest that permeable pavements' material composition and infiltration capabilities are critical in controlling pH and conductivity in urban runoff.

### Conductivity

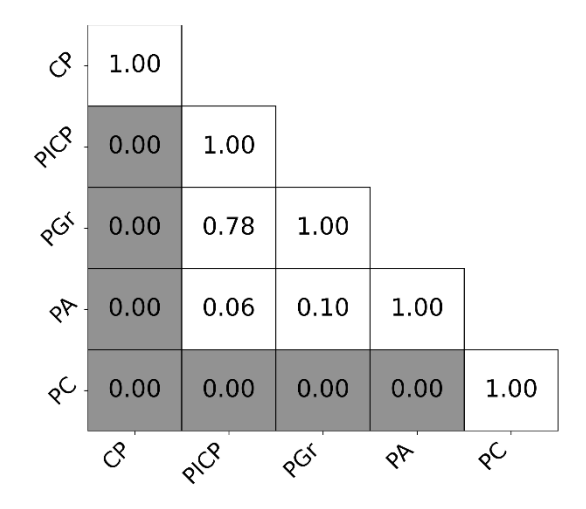


Figure 30: Pavements pairwise conductivity comparison with Wilcoxon signed-rank test.

# 5.2.7 Hydrocarbons (PAH and TPH)

Hydrocarbons, including Polycyclic Aromatic Hydrocarbons (PAHs) and Total Petroleum Hydrocarbon (TPH), are environmental contaminants of concern due to their persistence and potential risks to ecosystems and human health. PAHs are organic compounds composed of multiple aromatic rings, primarily formed during incomplete combustion of organic materials such as fossil fuels, wood, and biomass. TPH, on the other hand, represents a broad category of petroleum-derived compounds (e.g., alkanes, cycloalkanes, and aromatic hydrocarbons) originating from fuels, lubricants, or industrial releases. In permeable pavement systems, hydrocarbons are critical to monitor, as they may leach into underlying soils or groundwater, particularly in areas exposed to vehicular runoff or accidental spills. In this study, all TPH results were below the PQL, indicating no quantifiable concentrations of petroleum hydrocarbons in the evaluated systems. As a result, TPH will not be discussed further.

Similar to metals, only a limited number of water samples showed quantifiable PAH concentrations. Figure 31 illustrates the count of samples with PAH event and mean concentrations

(EMCs) exceeding the Minimum Detection Limit (MDL) and those quantified above the Practical Quantitation Limit (PQL). The data indicates that only a subset of PAHs could be reliably quantified. Heavier PAHs, such as Benzo[a]pyrene, Chrysene, Fluoranthene, and Phenanthrene—were more frequently quantified across pavement types. Their lower volatility and environmental persistence likely contributed to their detectability. In contrast, lighter PAHs like Naphthalene and Acenaphthylene, which have shorter retention times and higher volatility, were often detected but rarely quantified, as their concentrations typically fell below the PQL. This is reflected in the data, where detection counts are higher, but quantification counts are lower, especially for lighter PAHs.

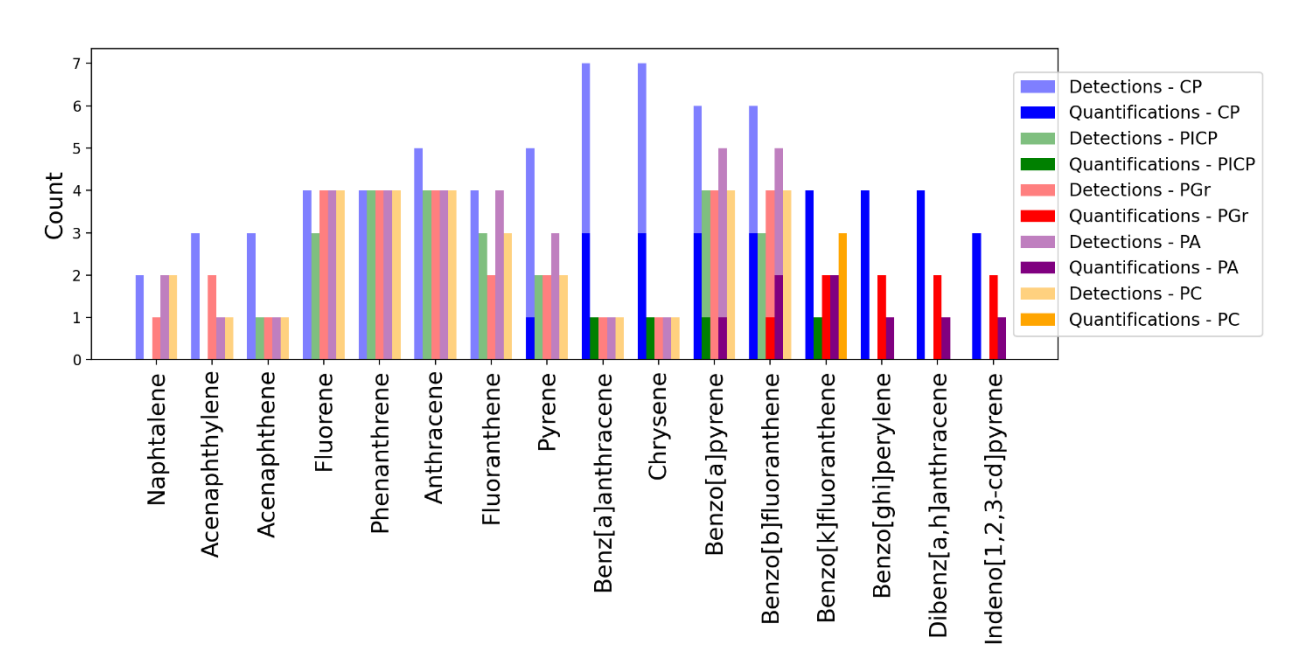


Figure 31: PAH number of detections and quantifications for 16 different chemicals

A plot of total PAH concentrations by event and pavement type is shown in Figure 32. It shows a general trend of decreasing PAH concentrations. This decline could be associated with the initial higher leaching of PAHs from the pavements when newer, susceptible to stormwater runoff for the CP, and infiltration for the PPs. The PAH concentrations likely start high during the initial phase due to higher volatile content in fresh asphalt concrete, which diminishes over time as the pavement cures and fewer contaminants are available for leaching.

Event 7 shows an increasing PAH concentration for the CP and the PA. This variability in the trend could suggest the influence of external, point-source factors like vehicle oil leakage, tire wear, or other contamination from nearby sources, contributing additional PAHs into the runoff that was not directly related to the aging or composition of the pavements. These sources could occasionally elevate PAH levels in runoff during specific events.

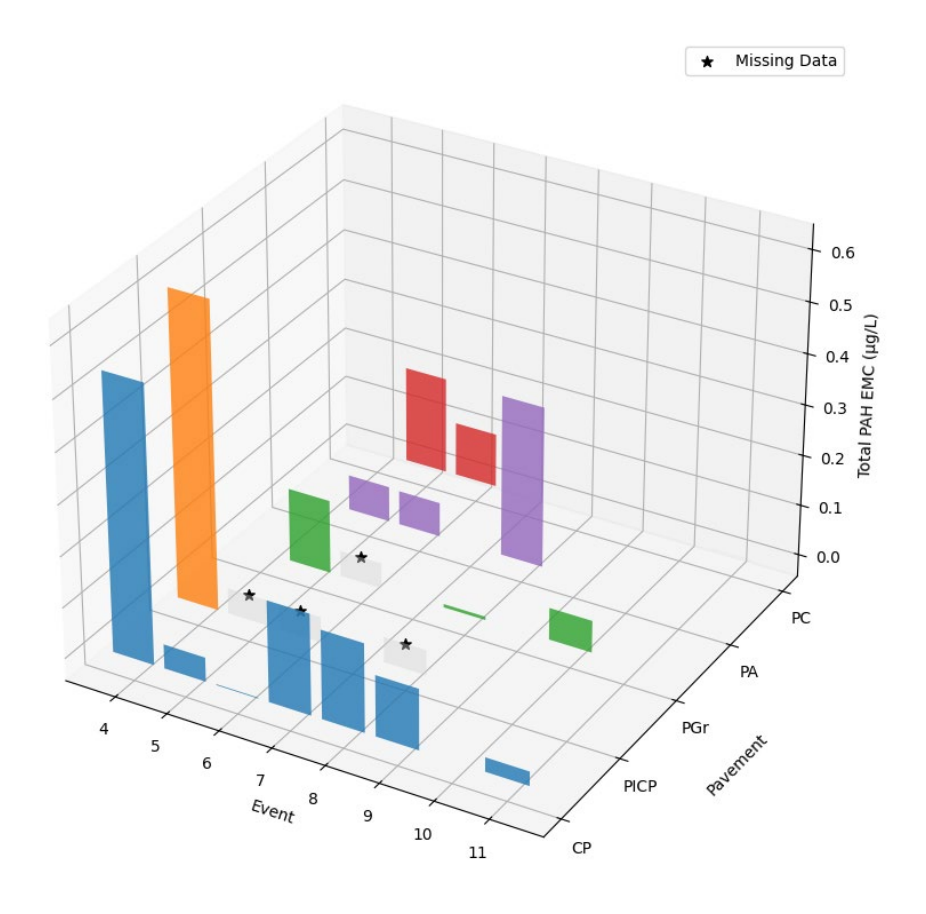


Figure 32: Total PAH EMCs for the monitored events

Despite the variability between events, the overall concentrations of PAHs were low for both the CP and the PPs, with a maximum concentration of around 0.6  $\mu$ g/L (Figure 31). This suggests that even though PAHs are present, the leaching from these pavement types is not an environmental concern.

PAH concentration box plots are shown in Figure 33. The water runoff from the CP has higher PAH concentrations than the PPs. Outlier observations suggest the random nature of PAH deposition across the parking lots. Due to the small sample size of PAH quantifications, it was not possible to conduct statistical comparisons of concentrations between pavement types.

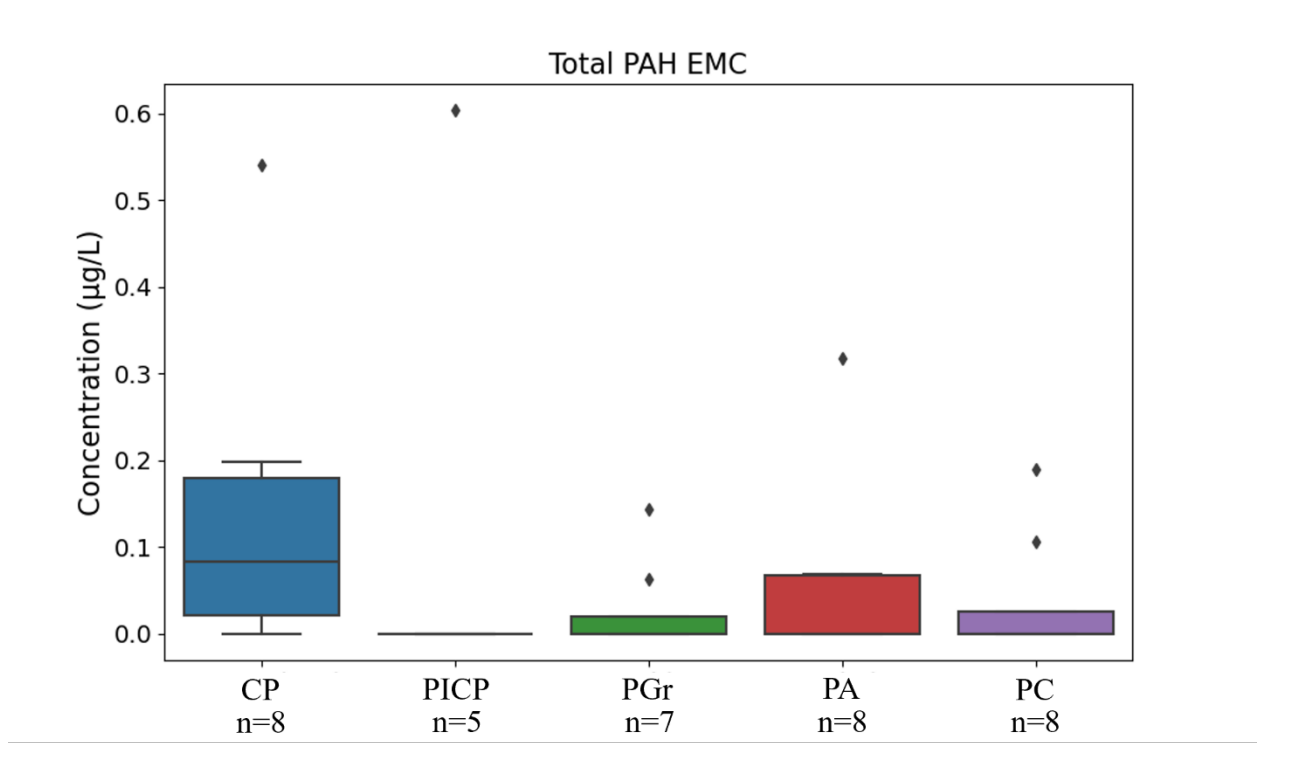


Figure 33: PAH concentration boxplots for all analyzed events

# **5.3** Correlation Analysis

## 5.3.1 Correlations Between Water Quantity and Water Quality Parameters

The correlation analysis between water quantity and water quality parameters describes the influence of hydrological factors on pollutant behavior across different pavement types. It aims to identify key factors affecting pollutant concentrations and transport mechanisms by examining relationships between rainfall characteristics (e.g., depth, duration, and intensity), antecedent dry period, peak flow, and runoff volume versus the monitored pollutants. Understanding these

relationships allows for interpreting the ability of PPs to mitigate pollutant loads and inform design strategies for enhancing water quality outcomes.

For the CP, the correlation analysis identified significant relationships between some water quantity indicators and water quality parameters (Figure 34). The shaded cells in these figures suggest a statistically significant correlation at 95% confidence.

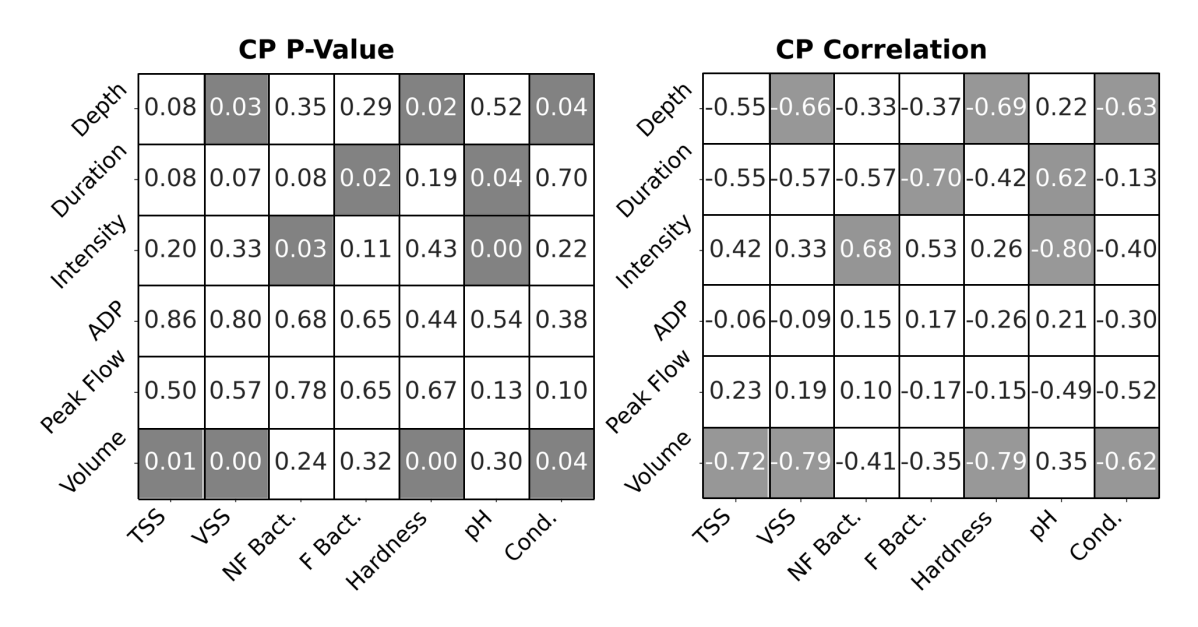


Figure 34: CP water quantity versus water quality correlation analysis

Outflow volume is significantly negatively correlated with TSS, VSS, hardness, and conductivity. Higher runoff volumes corresponded to decreased concentrations of these pollutants, reinforcing the dilution phenomenon observed with rainfall depth. These findings imply that the increased water volume effectively reduces the pollutant concentrations in the runoff from the CP surfaces during larger storm events. As rainfall flows over the CP, it washes off accumulated surface pollutants, and during high-volume storm events, the concentration of these pollutants gets diluted, decreasing their concentration. This dilution effect is characteristic of impervious surfaces,

where water cannot infiltrate the ground, leading to higher runoff volumes that carry, but also dilute, surface pollutants.

Rainfall duration was positively correlated with pH, indicating that longer events led to higher pH levels in the runoff. This could be due to prolonged interaction between rainwater and pavement materials, allowing for greater leaching of alkaline substances that raise the pH. Also, rainfall intensity displayed a significant positive correlation with non-fecal bacteria levels and a significant negative correlation with pH. Higher intensity storms were associated with increased mobilization of non-fecal bacteria, likely due to the scouring effect of heavy rainfall dislodging bacteria from the pavement surface. The decrease in pH with higher intensity may be the result of the rapid runoff preventing sufficient interaction with pavement materials that could otherwise neutralize acidity. Finally, the rainfall depth exhibited significant negative correlations with VSS, hardness, and conductivity, indicating that larger rainfall depths were associated with lower concentrations of these pollutants. This also suggests a dilution effect, where increased rainfall volume dilutes the runoff's soluble and particulate matter concentration.

The correlation analysis for the PPs showed different relationships between water quantity and water quality than those observed for the CP (Figures 35 to 38). Unlike the CP, where increased rainfall depth and runoff volume were generally associated with decreased pollutant concentrations due to dilution effects, the PPs exhibited positive correlations between water quantity indicators and pollutant concentrations. The positive correlations between rainfall depth, runoff volume, and pollutant concentrations in PPs suggest that larger storm events can mobilize accumulated pollutants within the pavement structure, leading to higher concentrations in the outflow.

For the PICP and PGr pavements, rainfall depth showed significant positive correlations with TSS and VSS concentrations (Figures 35 and 36, respectively). Specifically, in the PICP pavement,

depth was positively correlated with hardness (correlation coefficient of 0.67, p = 0.0499) and negatively correlated with conductivity (correlation coefficient of -0.73, p = 0.0246). This suggests that larger rainfall events may mobilize more suspended solids within the permeable pavement structure, leading to higher concentrations in the outflow. Similarly, in the PGr pavement, depth was significantly positively correlated with TSS (correlation coefficient of 0.67, p = 0.033) and fecal bacteria (correlation coefficient of 0.71, p = 0.031), indicating increased pollutant mobilization during larger storms.

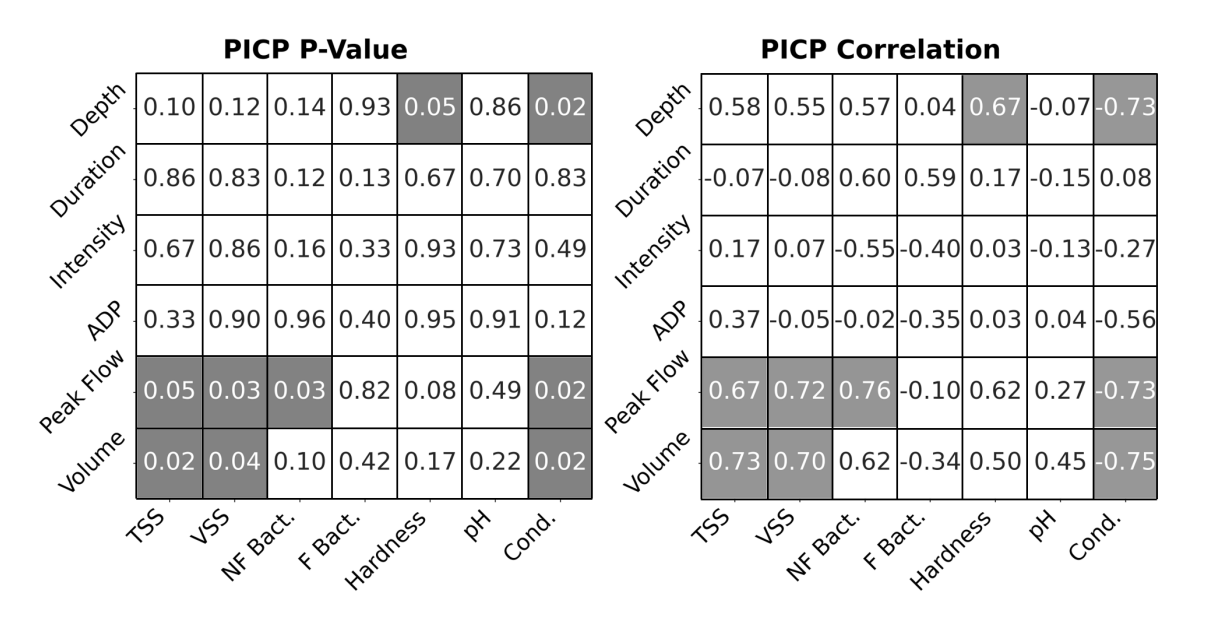


Figure 35: PICP water quantity versus water quality correlation analysis

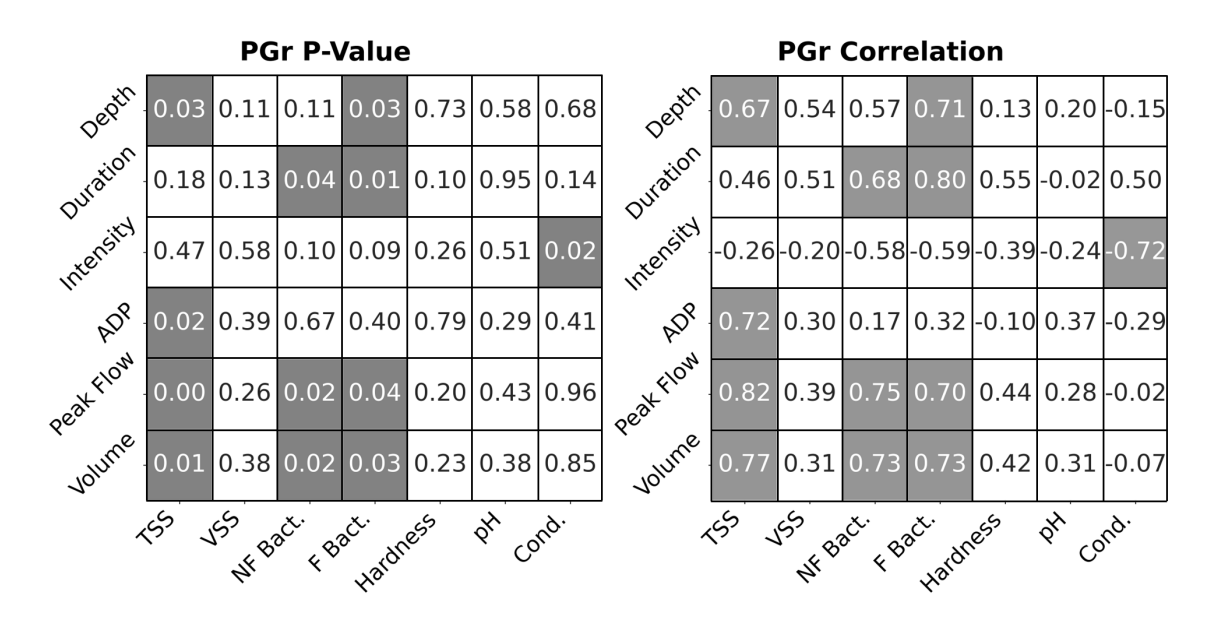


Figure 36: PGr water quantity versus water quality correlation analysis

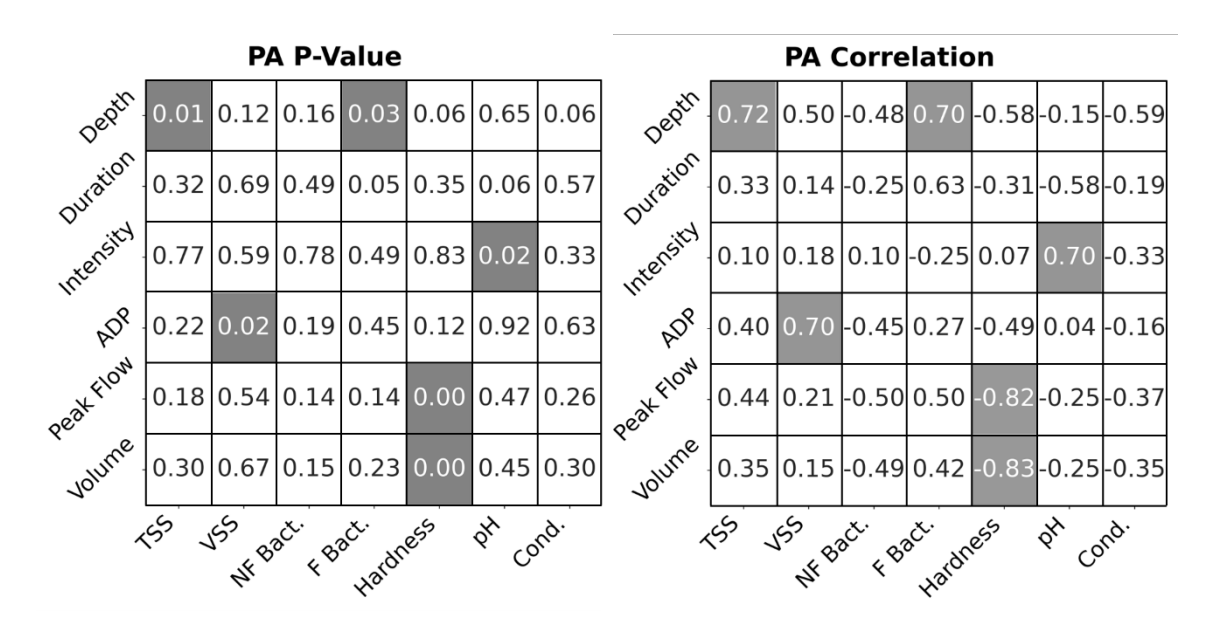


Figure 37: PA water quantity versus water quality correlation analysis

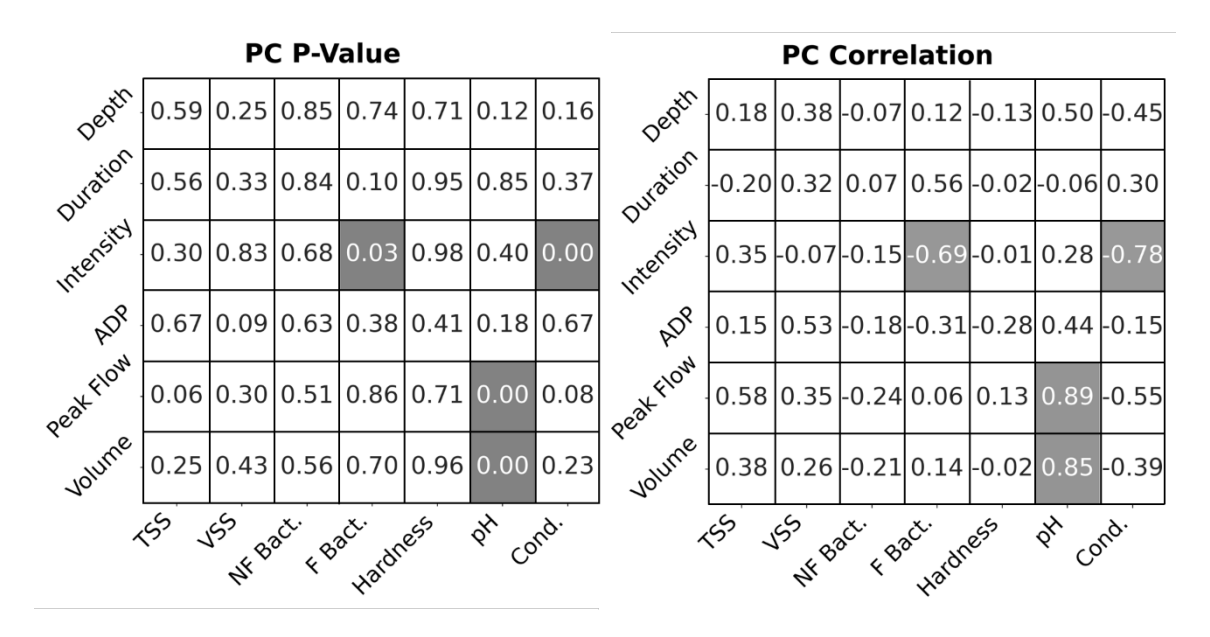


Figure 38: PC water quantity versus water quality correlation analysis

Runoff volume was also significantly positively correlated with TSS and VSS in the PICP and PGr pavements. In the PICP pavement, volume was positively correlated with TSS (correlation coefficient of 0.73, p = 0.025) and VSS (correlation coefficient of 0.70, p = 0.036). This contrasts with the CP, where runoff volume was negatively correlated with these pollutants, highlighting a key difference in how PPs influence pollutant transport mechanisms.

The PA pavement showed significant positive correlations between rainfall depth and TSS and fecal bacteria (Figure 37). Additionally, the ADP which is an indicator of length of drought prior to a rain event, was significantly positively correlated with VSS, suggesting that longer dry periods lead to increased accumulation of particulates that are subsequently mobilized during rainfall events. However, the ADP overall had only a few significant correlations across the PP types. This limited influence was unexpected, as ADP is typically considered a key factor in pollutant buildup on surfaces between storm events. The lack of consistent correlations suggests that factors other

than ADP, such as rainfall intensity or surface characteristics, may have played a more important role in pollutant mobilization and transport across both PPs and the CP.

Differences are evident in the PA and PC pavements; the PA pavement showed strong negative correlations between hardness and both peak flow (correlation coefficient of -0.82, p = 0.002) and volume (correlation coefficient of -0.83, p = 0.002) (Figure 37), indicating that increased flow reduces hardness concentrations, possibly due to dilution or reduced leaching of minerals. In contrast, the same water quality parameters (peak flow and volume) have a strong positive relation with pH for the PC pavement, highlighting that the increased flow produces a buffer effect, increasing the pH values of the outflow.

These findings highlight that the differences in materials and void structure between PPs play a significant role in the relationship between water quantity and water quality parameters. Each material's surface characteristics, porosity, and infiltration capacity can lead to varying levels of pollutant retention, accumulation, and mobilization.

Moreover, the contrast between CP and PPs is particularly notable due to the distinct processes involved. CP primarily manages water through runoff, which often results in the dilution of surface pollutants during transport. In contrast, the PPs promote infiltration, which filters and retains pollutants within the pavement layers and mobilizes accumulated pollutants on the surface. This fundamental difference in water management explains the variations observed in pollutant behavior between the two pavement types.

### 5.3.2 Correlations Between Water Quality Parameters

The correlation analysis between water quality parameters by pavement type is summarized in Figures 39 to 43. For the CP, the TSS and VSS concentrations show a very strong positive correlation, (i.e., correlation of 0.96), suggesting that VSS forms a significant portion of the total

suspended solids (Figure 39). Hardness also showed a notable correlation with other pollutants, particularly with VSS, non-fecal bacteria, and TSS (correlations of 0.63, 0.65, and 0,61, respectively), indicating a likely common source for these pollutants. Additionally, the negative correlation between hardness and pH (correlation of -0.61) is caused by reduced buffering capacity and changes in water chemistry for the CP.

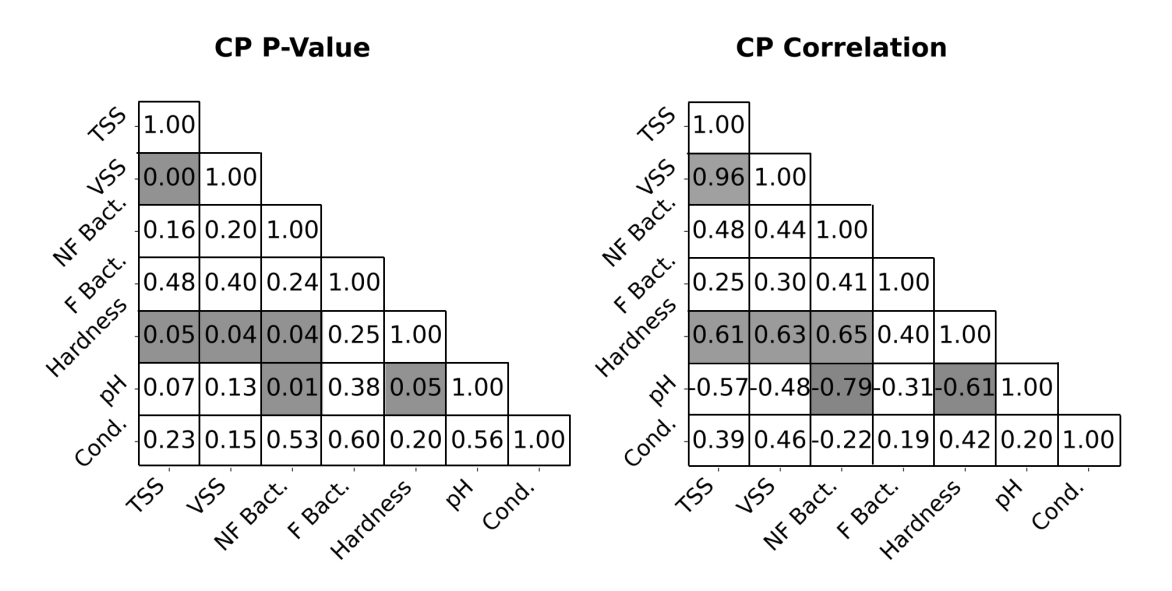


Figure 39: Correlation analysis between pollutants; CP

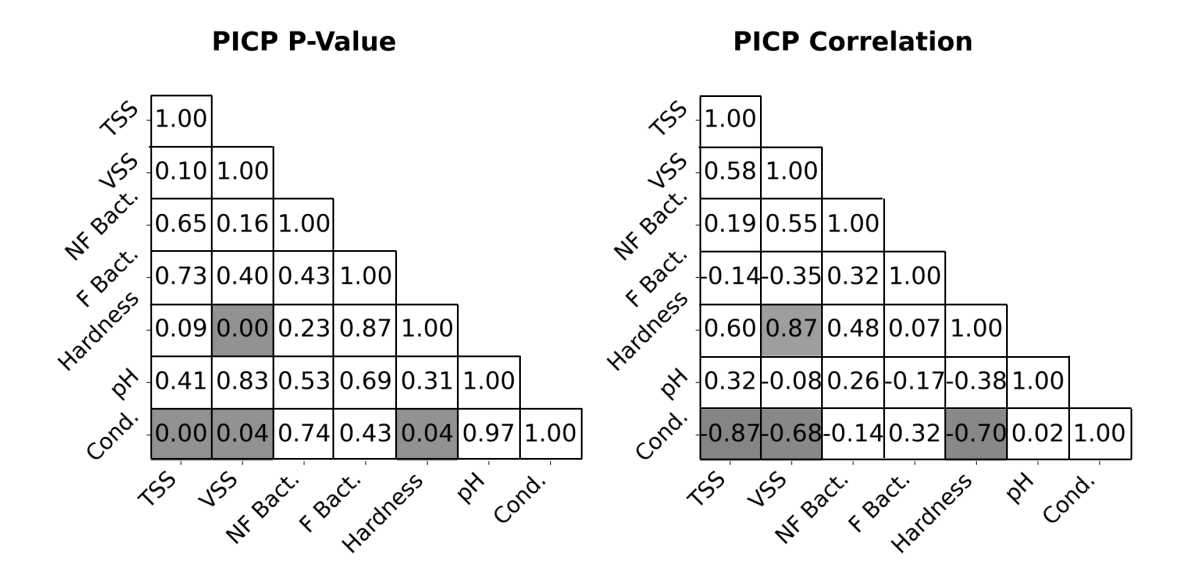


Figure 40: Correlation analysis between pollutants; PICP pavement

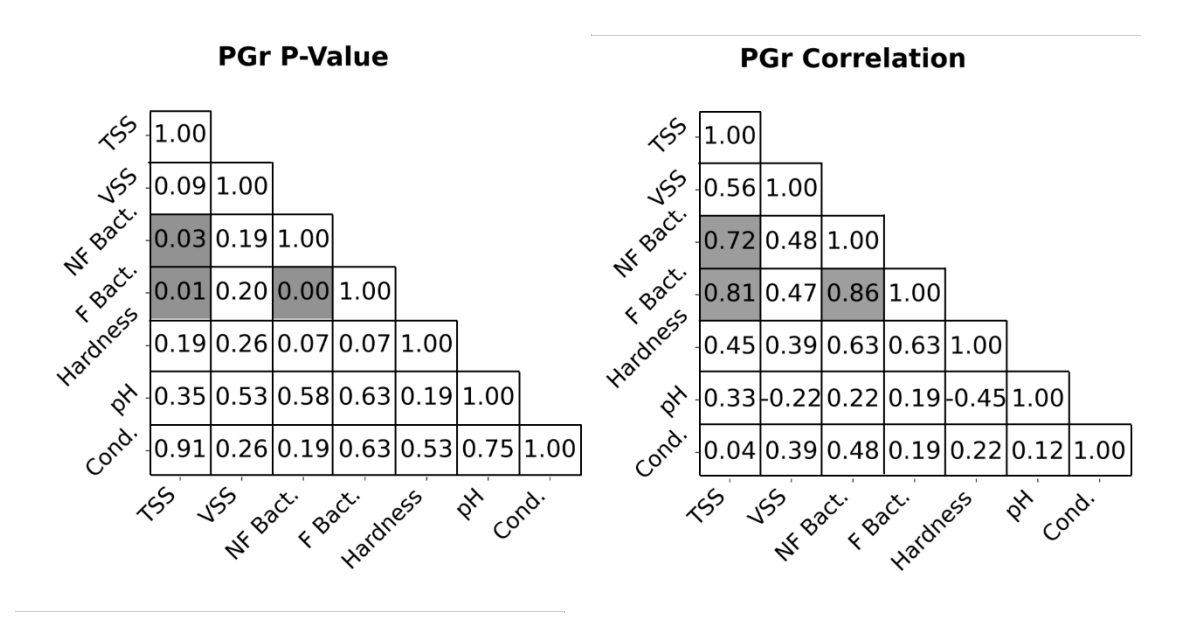


Figure 41: Correlation analysis between pollutants; PGr pavement

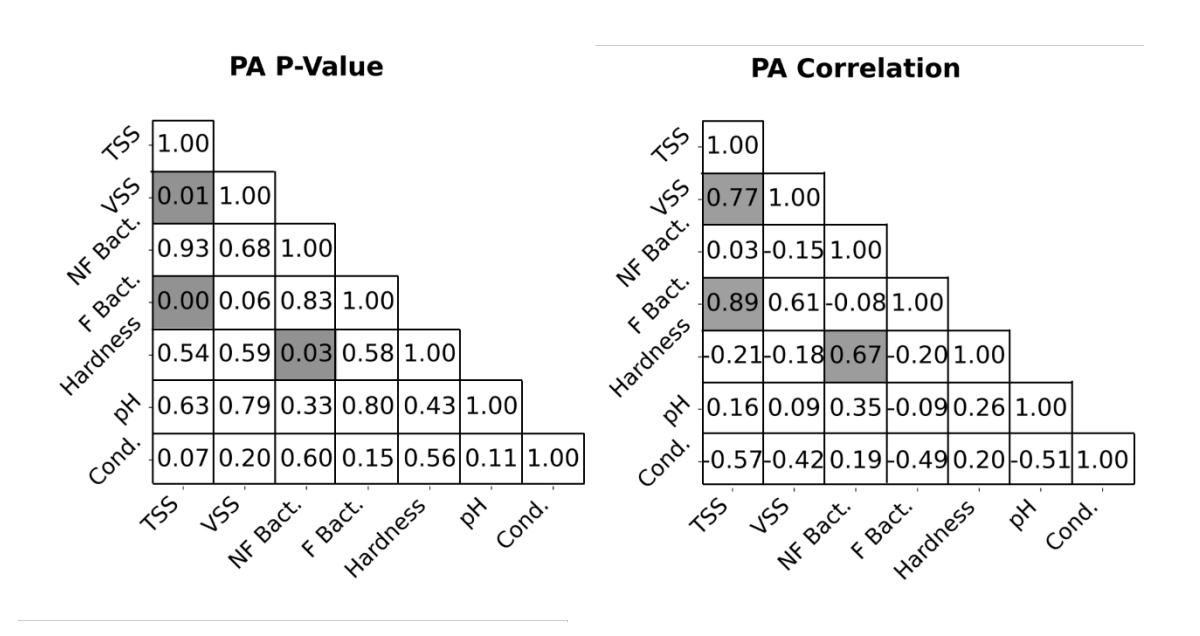


Figure 42: Correlation analysis between pollutants; PA pavement

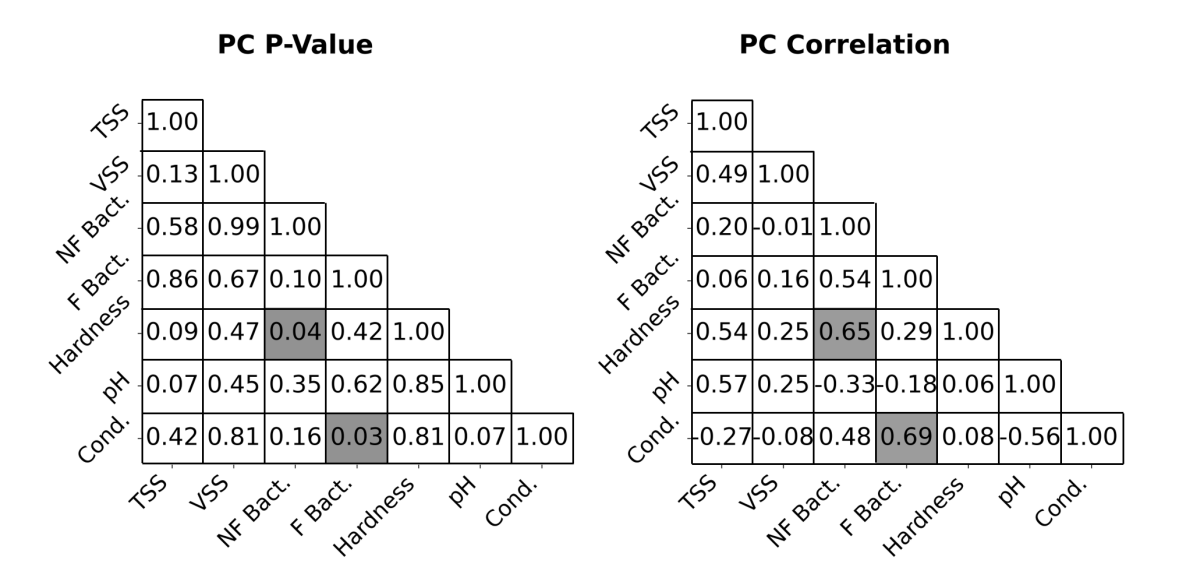


Figure 43: Correlation analysis between pollutants; PC pavement

For the PICP pavement (Figure 40), hardness showed a strong positive correlation with VSS, suggesting that the higher concentrations of VSS may be associated with the presence of calcium and magnesium ions contributing to water hardness. Conductivity also had a significant, strong negative correlation with TSS and VSS, suggesting that as particulate matter increases, the dissolved ion concentration in the water decreases, which lowers conductivity.

For the PGr pavement (Figure 41), non-fecal bacteria showed a strong positive correlation with TSS and fecal bacteria, indicating that the presence of suspended solids is associated with increased bacterial concentrations. Fecal bacteria also have a strong positive correlation with non-fecal bacteria, suggesting a common source of these pollutants in the PGr pavement. These relationships suggest that bacteria were likely transported along with particulate matter onto this pavement type.

For the PA pavement (Figure 42) the VSS showed a significant positive correlation with TSS. Additionally, fecal bacteria displayed a significant positive correlation with hardness, suggesting

that the presence of calcium and magnesium ions may be associated with bacterial accumulation. These relationships highlight the co-occurrence of particulate matter and bacteria, potentially driven by the retention and transport mechanisms within the PA pavement.

For the PC pavement (Figure 43), hardness showed a strong positive correlation with fecal bacteria, indicating that higher levels of calcium and magnesium are associated with an increase in fecal bacterial concentrations. Additionally, conductivity was significantly positively correlated with hardness, suggesting that the mineral content of the water in PC pavement may influence bacterial transport and overall water chemistry.

This analysis demonstrated significant differences in the relationships amongst pollutants between the CP and the PPs, as well as between PP types. For the CP, the TSS and VSS concentrations were positively correlated, indicating that organic particulates are a significant component of the suspended solids in runoff. Additionally, hardness correlated positively with VSS, non-fecal bacteria, indicating that mineral content in runoff may promote bacterial growth or that both VSS and non-fecal bacteria are influenced by common sources such as soil erosion. A negative correlation between hardness and pH implies that increased mineral content may lower the pH, affecting water chemistry.

In contrast, PPs showed fewer significant correlations between pollutants. Their ability to reduce pollutants depends on their surface permeability, void structure and material chemistry. For instance, the PC pavement showed TSS and VSS negatively correlates with conductivity, suggesting that as particulates are filtered out, the concentration of dissolved ions increases, enhancing conductivity. The PGr pavement showed strong positive correlation between TSS and both types of bacteria, indicating that this pavement type may allow more particulate and bacterial transport compared to others. These differences arise because PPs pavements facilitate the

infiltration of water, which reduces surface runoff and alters the transport mechanisms of pollutants, leading to different interactions than those observed in CPs.

The PA was the only PP that exhibited a significant positive correlation between VSS and TSS, being similar to the CP on this respect. This was likely the result of comparatively lower permeability and filtration efficiency, enabling the relationships between VSS and TSS to be easily discerned for these pavements. Furthermore, the positive correlation between fecal bacteria and hardness in this pavement type suggests that mineral content may influence bacterial presence. In the PC pavement, significant positive correlations between hardness, conductivity, and fecal bacteria indicate higher mineral dissolution, potentially affecting bacterial transport. These findings underscore that the specific composition and design of each PP type significantly influence the interactions and transport mechanisms of pollutants, affecting their overall performance in water quality management.

## **5.4** Temperature

### 5.4.1 Pavement Sensor Calibration and Validation

Before temperature data can be analyzed, we need to make sure the readings are accurate and without bias. Table 19 details the difference between each DS18B20 sensor and the reference probe temperatures before calibrating over a temperature range of 1°C to 55°C. Figure 44 shows the relationship between DS18B20 sensor 5 and the reference probe. It is evident that this sensor has a strong linear relationship with a correlation coefficient of 0.99. Also, the temperature differences are higher for temperatures closer to the minimum and maximum of the calibration range. All the sensors slightly overestimate lower temperatures and underestimate higher temperature readings before the calibration.

Table 19: Temperature differences before the calibration process

Temperature Probe	Maximum	Average	STD (°C)
rrobe	Difference (°C)	Difference (°C)	
Sensor 1	0.8	0.6	0.1
Sensor 2	0.7	0.4	0.2
Sensor 3	0.7	0.3	0.2
Sensor 4	1	0.7	0.2
Sensor 5	0.7	0.3	0.2
Sensor 6	0.7	0.4	0.1
Sensor 7	0.6	0.2	0.2
Sensor 8	0.8	0.4	0.3
Sensor 9	0.8	0.4	0.2
Sensor 10	0.2	0.1	0.1

Figure 44: Relationship between DS18B20 Sensor 5 and the reference probe temperatures (°C)

Appendix D contains the individual calibration curves and the errors for each sensor. The linear regression equation established for each sensor was used to adjust the field temperature readings. Table 20 shows the results after the calibration process. After calibrating all sensors, the average error decreased or remained the same, except Sensor 8 that exhibited a slight increase in maximum error. Based on the temperature values obtained after the individual calibration, the sensors were considered suitable for monitoring the temperature on the permeable pavement system. After installation, the temperature sensors were validated in-situ by comparing a laser sensor that measures the surface temperature with the DS18B20 sensor readings. Table 21 summarizes the results of the temperature readings. It shows the differences between the temperature sensors and laser probe.

Table 20: Temperature differences after the calibration process

Temperature Probe	Max Diff. (°F)	Average Diff. (°F)	STD of Difference (°F)
Sensor 1	0.5	0.2	0.2
Sensor 2	0.4	0.2	0.2
Sensor 3	0.5	0.2	0.2
Sensor 4	0.7	0.4	0.2
Sensor 5	0.9	0.4	0.2
Sensor 6	0.7	0.4	0.2
Sensor 7	0.5	0.4	0.2
Sensor 8	1.8	0.7	0.4
Sensor 9	1.4	0.5	0.2
Sensor 10	1.1	0.2	0.2

These data indicate a consistent pattern across all pavement types and measurement times, whereby the laser measurements of the pavement surface temperature were higher than the probe measurements taken from the bottom of the pavement surface layer. The percentage difference between these two readings ranged from 9% to 17%, depending on the pavement type and the measurement time (e.g., Figure 45). This is expected, given the heat diffusion with depth within the pavement layers (Papagiannakis and Masad, 2024).

Table 21: Differences between the laser measurement and the pavement probe

Pavement	Pavement	Laser Measurement (°F)	Pavement Probe (°F)	Difference
	9/29/23 3:28 PM	130.5	119.2	9%
СР	10/3/23 10:30 AM	104.7	91.65	12%
CP	4/8/24 9:21 AM	88.3	80.78	9%
	4/8/24 5:00 PM	81.2	72.77	10%
	9/29/23 3:28 PM	116.8	105.2	10%
PICP	10/3/23 10:30 AM	96.5	82	15%
PICP	4/8/24 9:21 AM	82.2	72.16	12%
	4/8/24 5:00 PM	90	81.04	10%
	9/29/23 3:28 PM	129.1	111.73	13%
PGr	10/3/23 10:30 AM	100.7	83.8	17%
rui	4/8/24 9:21 AM	82	72.44	12%
	4/8/24 5:00 PM	95	83.02	13%
	9/29/23 3:28 PM	136.5	119.67	12%
PA	10/3/23 10:30 AM	102.4	91.07	11%
ΓA	4/8/24 9:21 AM	88.6	76	14%
	4/8/24 5:00 PM	95.3	85.94	10%
	9/29/23 3:28 PM	126.7	108.63	14%
PC	10/3/23 10:30 AM	98.7	82.89	16%
rc	4/8/24 9:21 AM	85	71.17	16%
	4/8/24 5:00 PM	88.2	75.51	14%



Figure 45: Temperature differences between pavement surface and permeable layer bottom

## 5.4.2 Pavements Temperature

The thermal performance of pavement surfaces plays a crucial role in their structural integrity, longevity, and environmental impact. Understanding the thermal behavior of these pavements is essential for material selection and design strategies aimed at enhancing durability and mitigating heat island effects. The time series for the minimum, average, and maximum temperatures recorded by pavement type are shown in Figures 46 to 48, respectively, and their corresponding statistics are summarized in Tables 22 to 24. Analyzing these temperatures allows assessing the ability of the CP and PPs to manage heat and respond to climatic variations.

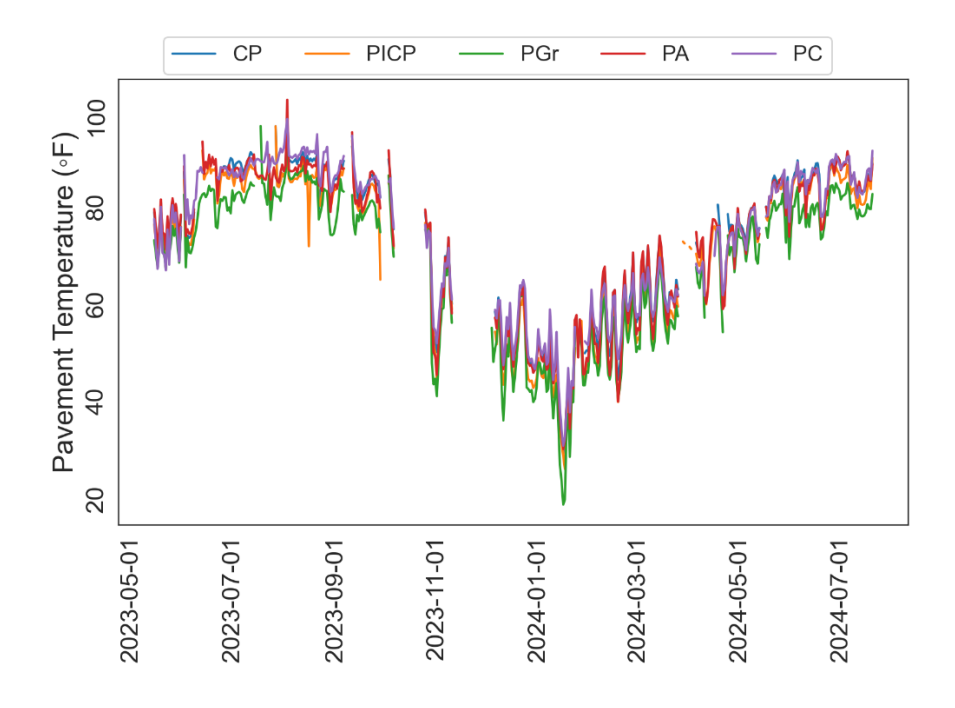


Figure 46: Minimum daily temperature time series

The PGr pavement exhibited the lowest mean in daily minimum temperatures (Figure 46, Table 22). This indicates a superior capability to dissipate heat during cooler periods due to the high volume of voids. In contrast, the PC showed the highest mean daily minimum temperature among the PPs (73.1 °F), slightly exceeding that of the CP (72.2 °F). The lower temperatures in the PGr

may be attributed to some extent to its higher albedo and its open-cell structure, which enhanced air circulation, facilitating more effective cooling.

Table 22: Daily minimum temperature statistics across different pavement types

Pavement	Mean of Daily	Median of Daily	STD of Daily
ravement	Minimum Temp. (°F)	Minimum Temp. (°F)	Minimum Temp. (°F)
CP	72.2	76.9	15.2
PICP	70.2	74.9	15.6
PGr	67.6	73.3	15.4
PA	72.0	76.8	15.3
PC	73.1	76.9	14.9

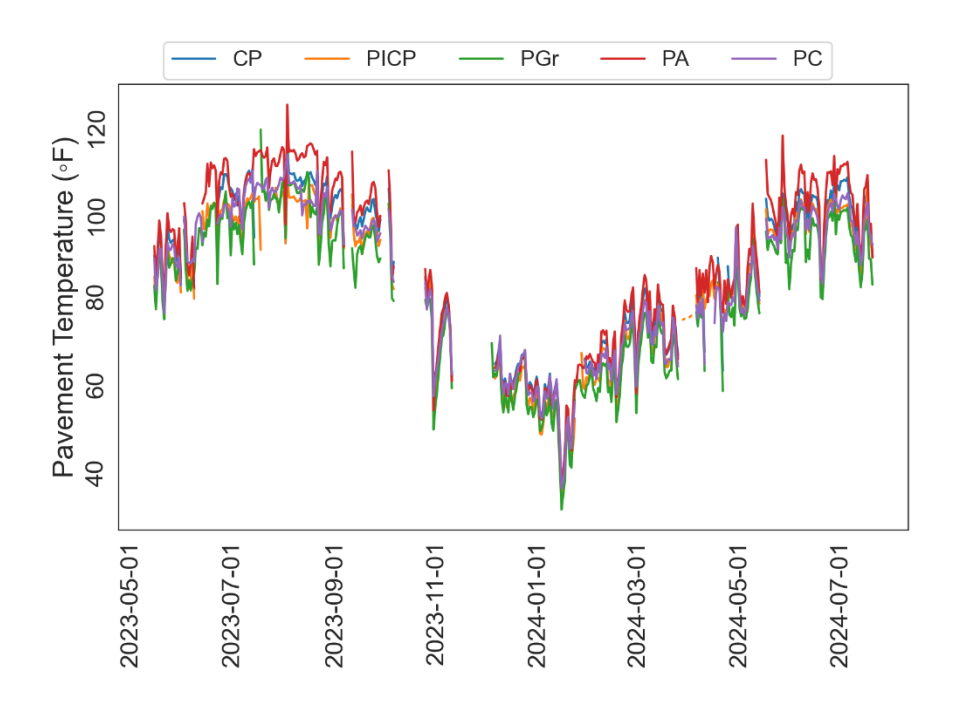


Figure 47: Average daily temperature time series

Table 23: Daily average temperature statistics across different pavement types

	Mean of Daily	Median of Daily	Std. Dev. of Daily
Pavement	Average Temperature	Average Temperature	Average Temperature
	(°F)	(°F)	(°F)
CP	103.9	107.3	23.0
PICP	97.7	100.2	19.5
PGr	99.4	104.2	22.9
PA	110.9	116.9	25.6
PC	97.2	102.0	19.7

The PC pavement demonstrated the lowest mean daily average temperatures at 97.2 °F, closely followed by PICP at 97.7 °F (Figure 47, Table 23). This suggests that the PC is more effective in maintaining lower average temperatures throughout the day, which can contribute to mitigating UHI effects and prolonging pavement life by reducing thermal stress. On the other hand, the PA recorded the highest mean daily average temperature at 110.9 °F, indicating a higher heat retention capacity. The lighter color and higher albedo of PC likely contributed to its ability to reflect more solar radiation, resulting in lower absorbed heat.

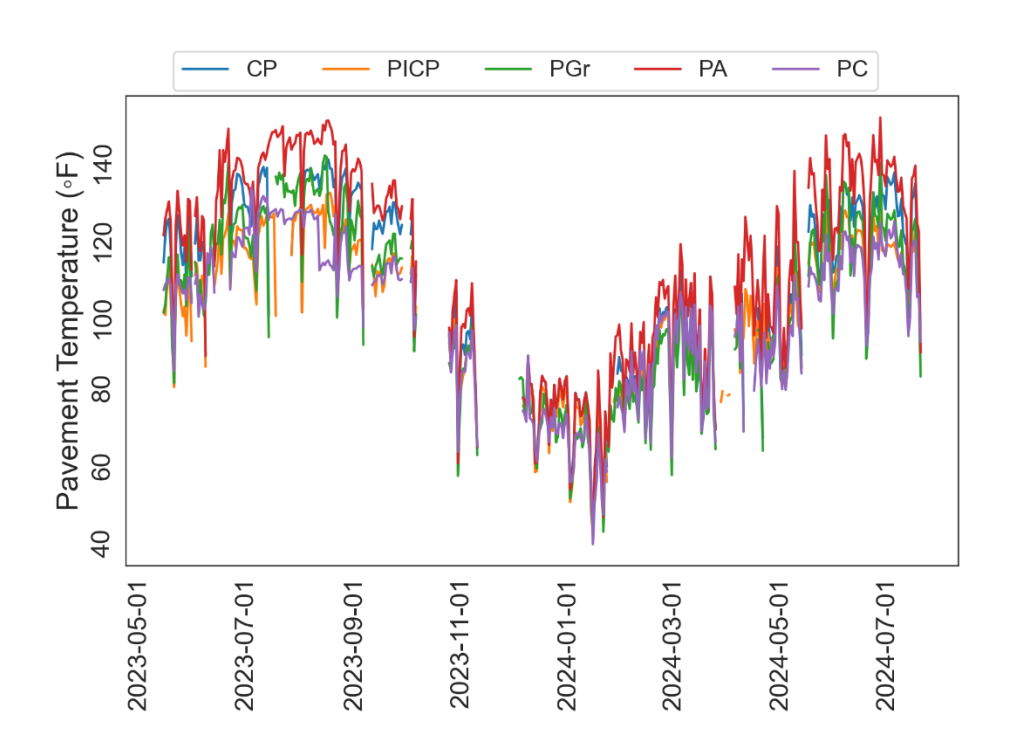


Figure 48: Maximum daily temperature time series

Table 24: Daily maximum temperature statistics across different pavement types

Pavement	Mean of Daily Maximum Temperature (°F)	Median of Daily Maximum Temperature (°F)	STD of Daily Maximum Temperature (°F)
CP	103.9	107.3	23.0
PICP	97.7	100.2	19.5
PGr	99.4	104.2	22.9
PA	110.9	116.9	25.6
PC	97.2	102.0	19.7

For the maximum temperatures, the PC again exhibited the lowest mean daily maximum temperatures at 97.2 °F (Figure 48, Table 24). This consistent performance underscores its effectiveness in limiting peak temperature increases, crucial for minimizing thermal expansion and associated pavement distress. Permeable asphalt, however, exhibited the highest mean daily maximum temperature at 110.9 °F, potentially increasing the risk of heat-related deformation. The PC's ability to maintain lower maximum temperatures dictates its suitability for applications where thermal performance is a critical consideration.

Comparing the thermal behaviors of the CP and PPs in terms of minimum, average, and maximum daily temperatures shows that the PPs generally exhibited superior thermal performance. The PC and the PICP pavements consistently maintained lower mean daily average and maximum temperatures than the CP. Specifically, the PC showed the lowest mean daily average and maximum temperatures, indicating its effectiveness in minimizing heat accumulation during high solar radiation periods.

The STDs give an insight into the pavement's thermal performance consistency. The PC and the PICP consistently showed lower STDs (around 19–20 °F for average and maximum temperatures), indicating more stable pavement temperatures. Moreover, the PA exhibited the highest STDs, especially in daily average and maximum temperatures (25.6 °F), highlighting higher thermal fluctuations.

The PA and the CP exhibited similar minimum daily minimum temperatures, indicating comparable heat retention during cooler periods. However, the PA records were significantly higher in terms of daily average and maximum temperatures than the CP. The elevated PA temperatures may be due to its material composition and darker color, leading to lower albedo and higher solar radiation absorption. Overall, the PC and the PICP exhibited superior thermal

performance compared to the CP, with lower mean and median temperatures and smaller standard deviations, indicating both effective heat management and thermal stability. The PA exhibited higher temperatures and greater variability across all metrics.

The temperature measurement data during a rainfall event can be seen in Figure 49. The surface temperatures of all five pavement types exhibit a noticeable decline at the start of rainfall events. The most drastic temperature decline was for the PGr pavement, while the CP showed the highest temperatures before, during, and after each event.

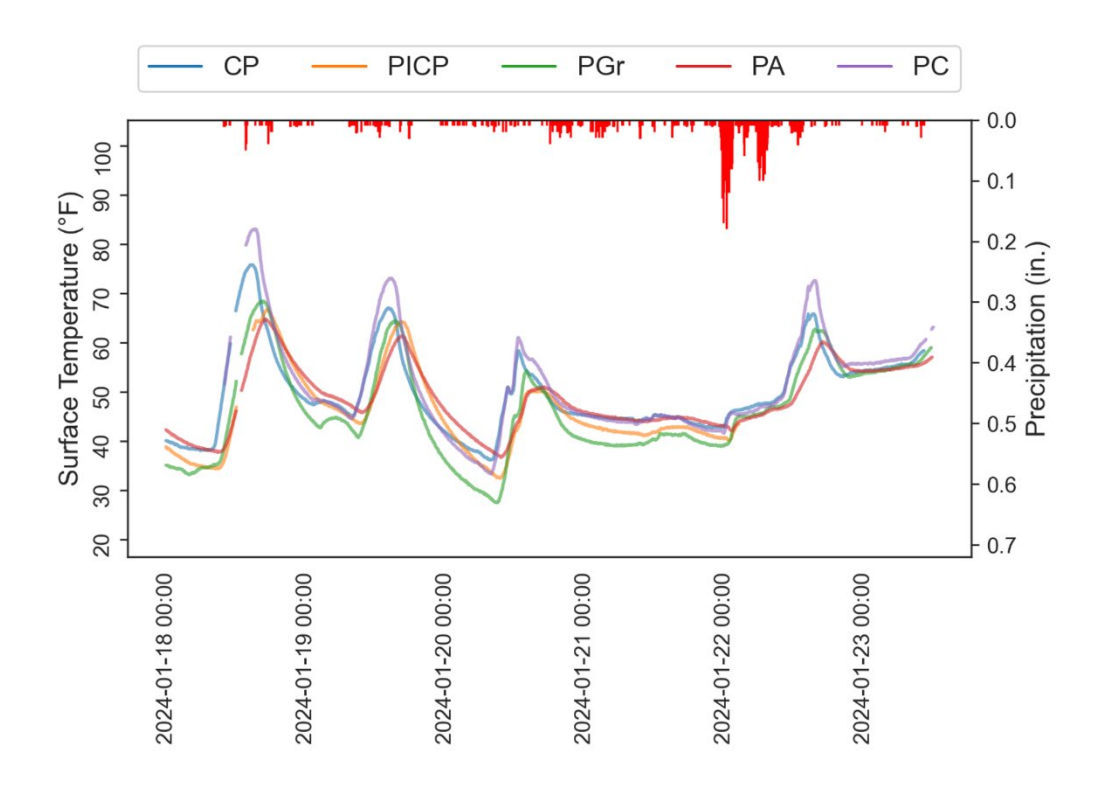


Figure 49: Temperature changes during rainfall events

As rainfall increases, all pavement types trended to lower temperatures, indicating a cooling effect driven by the moisture and potential evaporation. The PC appears to take longer to stabilize the temperature when subjected to water infiltration, suggesting that this pavement was less susceptible to temperature fluctuations.

According to the Shapiro-Wilk test, normality is violated for all pavement temperature data. Since normality is not the case for any of the daily temperature data, a pair-wise Wilcoxon signed-rank test was performed to evaluate if the median of the differences between the two pavements is different than zero. Figure 50 shows the median differences in daily minimum, average, and maximum temperatures between five pavement types, with the main diagonal representing the median temperature of each pavement. The Wilcoxon signed-rank test indicates that all pair-wise comparisons are statistically significant (p-value < 0.05), meaning that the pavements exhibit distinct temperature profiles.

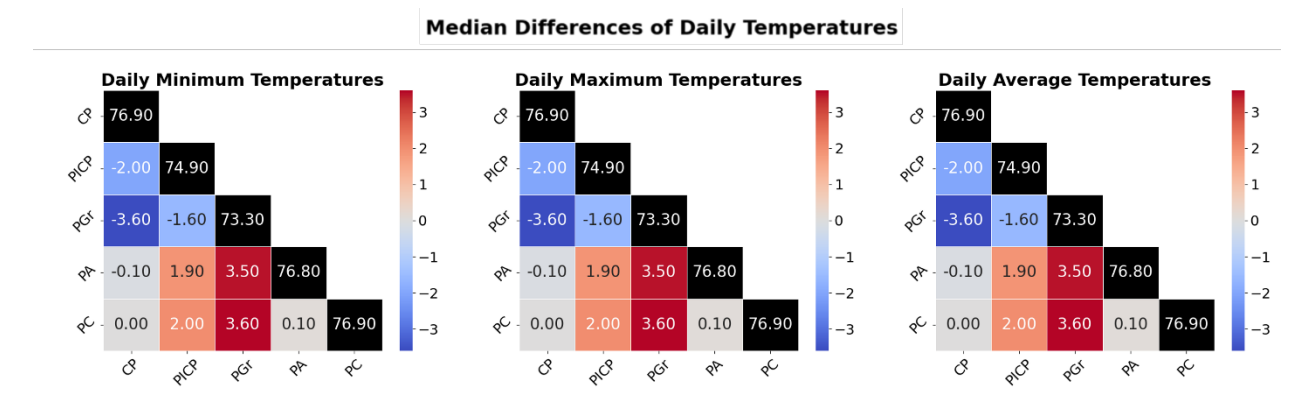


Figure 50: Comparison of the pavement surface temperatures median. The main diagonal shows the median temperature of the pavement.

The PA and the CP consistently show higher daily minimum, average, and maximum temperatures compared to the PICP, PGr and PC pavements. The PGr pavement shows the lowest temperatures, particularly for daily minima and maxima, suggesting better cooling performance. The PA, by contrast, had the highest daily maximum temperatures due to its high heat retention.

These temperature differences are mainly due to the albedo and the thermal properties of the materials. The PA and the CP absorb and retain more heat, leading to higher temperatures. In contrast, the PGr and the PICP allow for better heat dissipation through air circulation and water infiltration, resulting in cooler surface temperatures, especially during hot periods.

### 5.4.3 Water Temperature

To define the time period during which water was present on the pavement, temperature data from a pressure transducer was analyzed in conjunction with rainfall and pavement outflow data. The pressure transducer, installed on the inspection tube connected to the bottom layer of the pavement, continuously recorded temperature variations. Figure 51 shows a distinct temperature drop once the rainfall started. This temperature drop corresponds to when water begins to accumulate on the pavement, as the cooler rainwater comes into contact with the surface and lowers the temperature detected by the transducer. Following the initial drop, the temperature gradually increases until it stabilizes as rainfall continues or ceases, reflecting changes in water temperature due to the heat exchange with the warm pavement surface and structure.

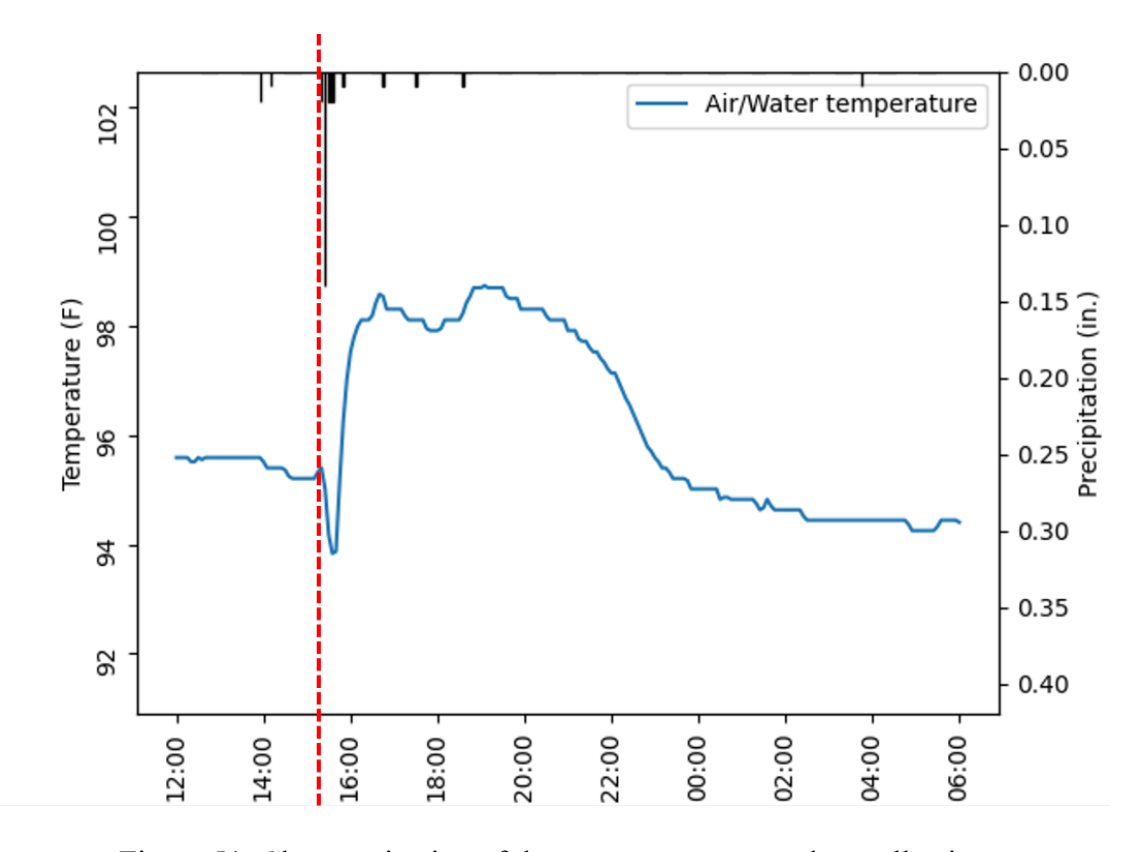


Figure 51: Characterization of the water temperature data collection

A dashed line indicates the point where the temperature initially changes due to water presence and was manually defined for each pavement and rainfall event. This point represents the transition from a dry to a wet pavement state and was used as the first water temperature observation. To accurately capture the duration of water presence until the event's conclusion, outflow data was incorporated. The final water temperature observation was recorded when the outflow reached zero, indicating that water had fully drained from the pavement.

Table 25 shows the results for the monitored events. Event 5 was excluded from the analysis due to malfunctioning on the pressure transducers. The average water temperature across different pavement types was evaluated to assess their thermal performance during rainfall events. The results show that the pavement's average water temperature can be classified (from lowest to highest) as PGr (71°F), PC (72.9°F), PICP (76.9°F), and PA (77.4°F). The PGr pavement consistently exhibited the lowest average water temperature, indicating less outflow thermal pollution. This result can be attributed to the high infiltration rate, which reduces the time where the water is in contact with the surface and subsurface layers.

The PC pavement also exhibited relatively low average water temperatures, although it was less effective than PGr. This performance can be attributed to its thermal properties and lower surface temperature compared to PA and PICP pavements. On the other hand, despite having the second lowest surface temperature, PICP recorded the second highest average water temperature. This outcome is likely due to its limited infiltration area, as permeability occurs only through the joints of the interlocking pavers. Consequently, the reduced infiltration capacity increases water retention time, resulting in prolonged contact between the water and the warmer pavement surface, thereby raising the water temperature.

Table 25: Water temperature data for all events.

Event	Pavement	Max (°F)	Min (°F)	Avg (°F)	Med (°F)	STD (°F)
	PICP	98.7	93.8	97.9	98.1	1.0
E4.1	PGr	-	-	-	-	-
Event 1	PA	98.1	96.7	97.6	97.7	0.4
	PC	-	-	-	-	-
	PICP	90.3	88.3	89.9	89.9	0.3
E4-2	PGr	83.4	82.2	82.9	82.9	0.5
Event 2	PA	91.6	89.4	91.0	91.1	0.5
	PC	88.7	86.7	88.3	88.5	0.4
	PICP	82.2	80.8	81.6	81.6	0.5
E4-2	PGr	77.2	76.9	77.0	77.1	0.1
Event 3	PA	83.6	82.9	83.2	83.0	0.3
	PC	80.7	80.4	80.5	80.6	0.1
	PICP	77.1	75.7	76.5	76.5	0.3
E 4.4	PGr	73.9	72.4	73.3	73.6	0.5
Event 4	PA	77.7	76.4	77.1	77.1	0.5
	PC	75.7	71.7	73.8	73.6	1.2
	PICP	54.8	48.9	53.3	53.8	1.3
E-vand (	PGr	52.1	44.6	49.2	50.1	2.2
Event 6	PA	57.1	51.0	56.1	56.8	1.6
	PC	54.3	47.1	51.5	51.5	2.2
	PICP	62.1	60.9	61.9	62.1	0.3
Ewant 7	PGr	61.1	60.5	60.8	60.9	0.1
Event 7	PA	62.6	61.4	62.2	62.4	0.4
	PC	61.1	60.2	60.8	60.9	0.2
	PICP	75.5	73.2	74.8	75.1	0.8
Event 8	PGr	72.9	72.4	72.6	72.7	0.2
Event 8	PA	74.8	73.6	74.4	74.4	0.4
	PC	73.6	71.7	73.1	73.4	0.6
	PICP	76.5	75.3	76.0	76.0	0.4
Event 9	PGr	73.1	72.9	72.9	72.9	0.1
Event 9	PA	76.0	75.5	75.6	75.7	0.2
	PC	74.4	72.9	73.8	73.8	0.4
	PICP	77.6	75.7	77.1	77.2	0.5
Event 10	PGr	73.9	73.8	73.9	73.9	0.1
Event 10	PA	77.6	76.0	77.2	77.4	0.5
	PC	75.7	74.4	75.4	75.5	0.3
	PICP	80.6	79.3	80.1	80.4	0.4
Evant 11	PGr	76.4	76.2	76.2	76.2	0.1
Event 11	PA	79.7	79.2	79.5	79.5	0.1
	PC	78.8	77.7	78.6	78.8	0.4

The PA exhibited the highest average water tempeature. This result aligns with findings from the surface temperature, where the PA had the highest surface temperatures observed on the permeable pavements. The pavement high temperature is primarily attributed to the pavement's darker color, which enhances it's absorption of solar radiantion resulting in greater heat retention.

As evidenced by the performance of the PICP, lower surface temperatures did not translate into lower outflow water temperatures. A similar effect was observed by Selbig & Buer, (2018) where the temperature analysis between the surface temperature and the water temperature of a PICP, PA, and PC shows that the outflow temperatures are from 1°C to 8°C higher than the surface temperature, with the PICP performing worse than the other pavements.

Figure 52 presents the variation of water temperature and pavement surface temperature during a rainfall event. Initially, the pavement surface temperature is higher than the water temperature, and, as the rainfall event progresses, the surface temperature decreases rapidly, reflecting the cooling effect of the rain on the pavement. However, the water temperature rapidly surpasses the pavement surface temperature due to absorbing the heat from the surface and sub-layers. Smaller differences between the water temperature and the water temperature indicate less heat transfer from the pavement to the infiltrating water, which implies better thermal performance and reduced thermal pollution.

To compare the pavements performance regarding the difference of temperature between the pavement surface and the water temperature on the outflow, a linear regression between the average pavement temperature and the water temperature for each event is shown in Figure 53. A strong positive correlation (R² between 0.88 and 0.95) was found for all pavements, but the relations differ across pavement types, indicating varying thermal responses.

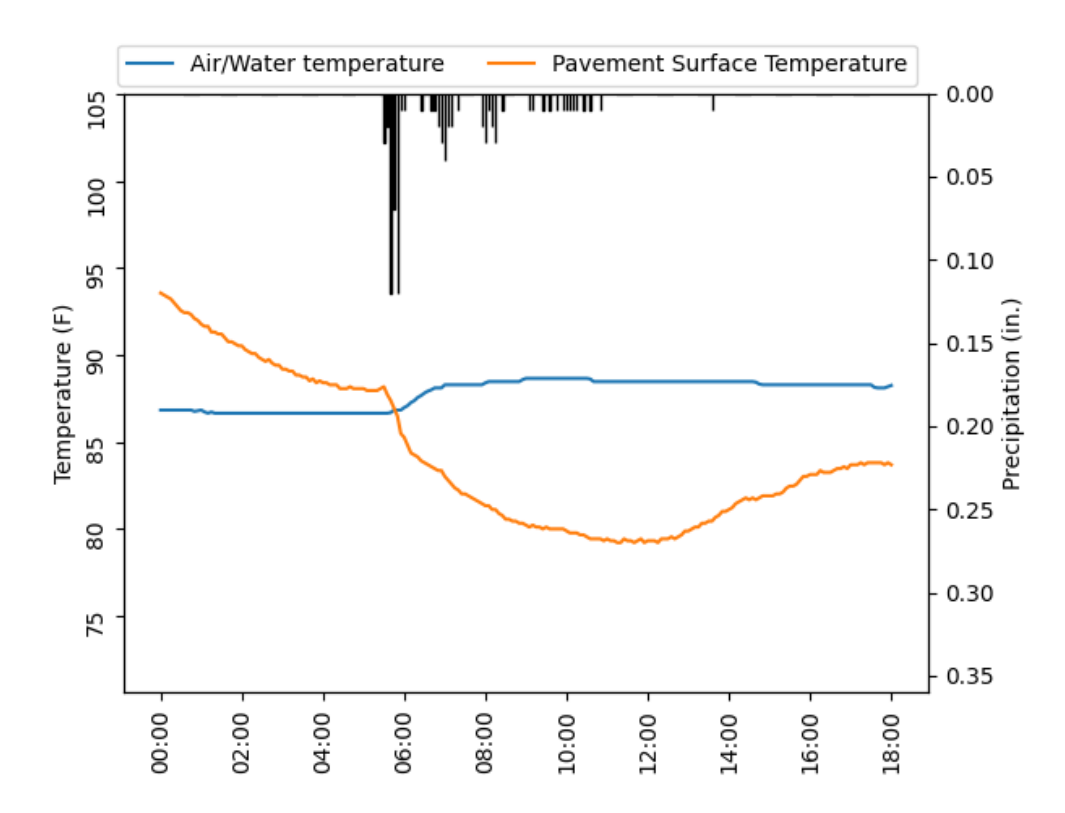


Figure 52: Comparison between pavement surface temperature and water temperature

Among the permeable pavements, PICP exhibits the steepest slope, suggesting a higher sensitivity of pavement temperature to changes in water temperature. This indicates that PICP water temperature increases more facing similar surface temperatures. Conversely, PGr shows a lower slope, implying better thermal regulation and less temperature variability compared to PICP.

Despite the higher slope of the PC, the lower temperature of the surface translates to lower water temperature, enhancing the control of thermal pollution of the pavement. On the other hand, the PA shows a smaller slope but since the surface temperature is the highest among the permeable pavements, the water temperature is the highest (on average) between the pavements.

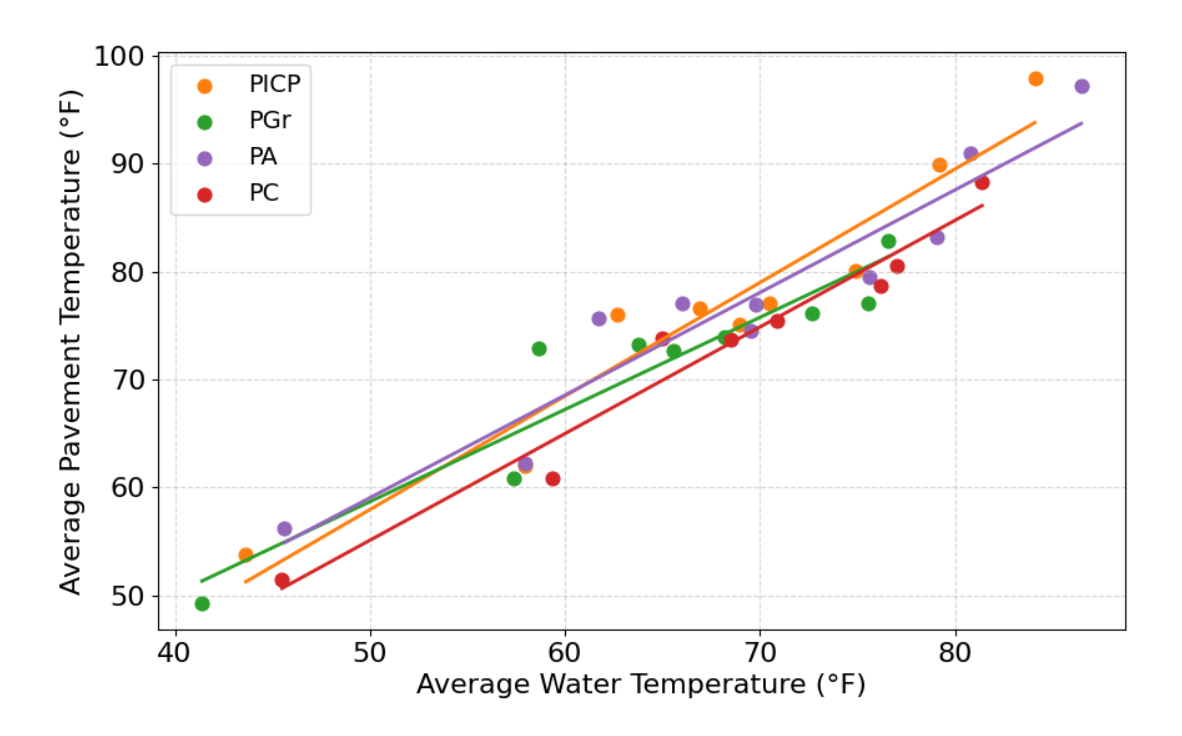


Figure 53: Linear relationship between water temperature and pavement surface temperature

Despite the increase in outflow water temperature from permeable pavements, studies have demonstrated that they are effective in mitigating thermal pollution compared to conventional pavements. Wang et al. (2023) reported that, in a lab-scale experiment, the outflow temperature from permeable pavement was 2.5°F to 8°F lower than that from conventional pavement, depending on the initial surface temperature. Similarly, Wardynski et al. (2013) observed a 9.5°F reduction in outflow temperature by incorporating internal water storage (IWS) in the permeable pavement system through the elevation of the outflow pipe. The IWS mechanism retains stormwater for extended periods, thereby allowing heat dissipation and resulting in lower outflow temperatures.

In summary, PGr and PC pavements exhibit superior thermal performance, with PGr achieving the lowest temperature differences in most events. Conversely, PA demonstrates the poorest performance, contributing to the highest thermal pollution in stormwater outflows.

### **5.5** Infiltration Rate

The average infiltration rates across the three monitored locations, along with the standard deviations (represented as error bars), are shown in Figure 54. Among the tested surfaces, the PICP exhibited the lowest infiltration rate, with an average of 2.88 in/min and a standard deviation of 1.32 in/min. These results are consistent with those reported by Collins et al., (2008) where a similar PICP had an average infiltration rate of 2.1 in/min using the ASTM C1781 method (single-ring falling-head). Since the infiltration in PICP primarily occurs through the joints between the concrete pavers, the limited void area significantly influences its infiltration rate (Rezaei & Karami, 2023).

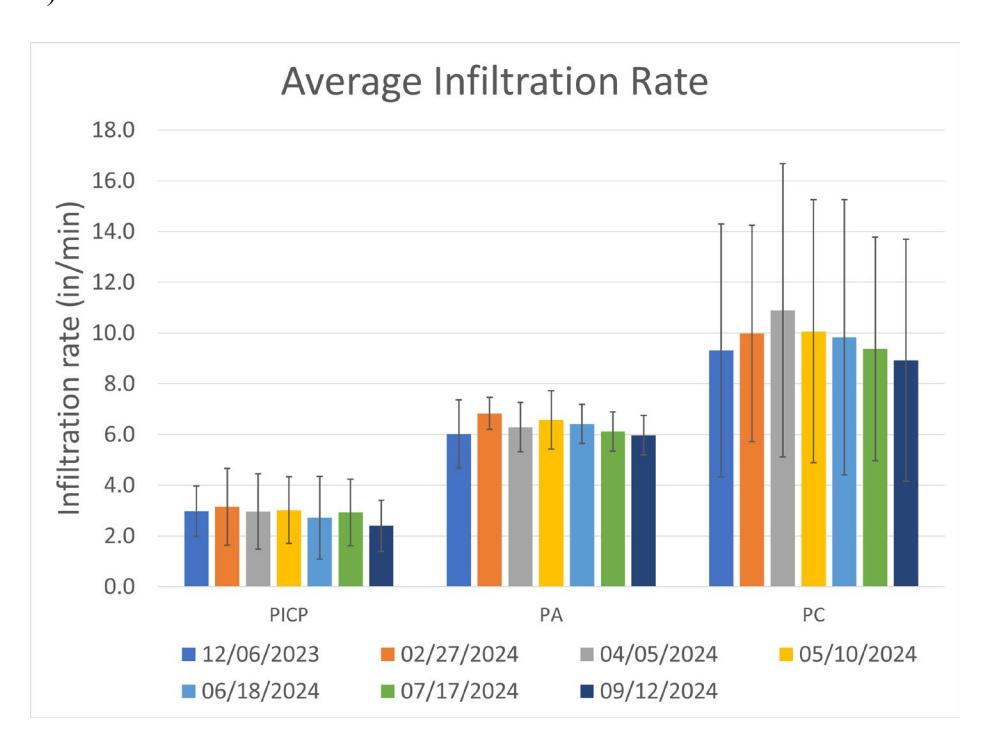


Figure 54: Average infiltration rate for the monitoring period. The error bars represent 1 STD from the three different locations.

The PA exhibited the second-highest infiltration rate among the tested pavements, with an average rate of 6.32 in/min and the lowest variability across the three locations, indicated by a standard deviation of 0.91 in/min. Comparable results were reported by Knappenberger et al., (2017) who observed an infiltration rate of approximately 5.3 in/min during the first year of monitoring. In contrast, Muttuvelu et al., (2024) monitored a similar PA pavement and recorded significantly higher initial infiltration rates, averaging 13 in/min during the first year.

The low spatial variability can be attributed to the uniformity of the construction method used for PA, where the continuous porous layer ensures more consistent infiltration across the entire surface. Over time, areas with higher traffic intensity, such as the central portion of the parking lot, are expected to experience accelerated clogging compared to the other locations, thereby increasing the spatial variability of infiltration rates on the PA (Knappenberger et al., 2017).

Finally, the PC had the highest average infiltration rate of 9.77 in/min. However, it also exhibited the greatest variability, with a standard deviation of 4.97 in/min. Welker et al., (2012) observed PC infiltration rates of 9.5 to 26 in/min when the pavement is in good condition. As shown in Table 26, the infiltration rate monitored at Location 1 was approximately half that of Location 2 and about 25% of the rate at Location 3. In contrast, Kumar et al., (2016) didn't observe any spatial variation on the monitored infiltration rate of the PC for the first two years, where only during the third year a significant reduction on the infiltration rate.

The high spatial variability may be explained by non-uniform compaction during construction, differences in curing conditions, or potential clogging at specific locations. Unlike other permeable pavements, permeable concrete is highly sensitive to small variations in its pore structure, which can lead to significant disparities in infiltration performance across different areas (Valinski & Chandler, 2015).

Table 26: Average infiltration rate (in/min) per monitoring location.

Pavement	Location 1	Location 2	Location 3
PICP	2.04±0.21	1.86±0.3	4.74±0.46
PA	6.02±0.39	7.55±0.37	5.38±0.38
PC	4.16±0.59	8.92±0.45	16.23±1.25

^{*}Data are shown as mean infiltration rate  $\pm 1$  standard deviation

It is important to note that the infiltration rate for all the pavements is significantly higher than all rainfall intensities (maximum intensity of 0.09 in/min). While our monitored pavements did not exhibit a clear sign of clogging during the observation period, long-term performance may be affected by progressive clogging, as shown in other studies, highlighting the clogging effect on the lifespan of permeable pavements and the potential need for maintenance over time.

Clogging can result from two primary mechanisms: surficial straining, where coarse particles accumulate on the surface forming a filter mat, and deep-bed filtration, where finer particles penetrate and fill the pores within the pavement structure (Sansalone et al., 2012). Both mechanisms progressively reduce the pavement hydraulic conductivity, with higher particulate matter (PM) loadings accelerating the rate of clogging. The infiltration rate typically follows an exponential decline, and depending on site-specific PM loadings, clogging can reduce the infiltration rate to critical levels within 1 to 3 years. Kumar et al. (2016) observed that for all monitored pavement types, the infiltration rate decreased by up to 10% in the first year, 40% in the second year, and more than 80% by the third year.

Although maintenance was not necessary during the PPS monitoring period, future clogging may require intervention. Common maintenance methods, such as vacuum sweeping or pressure washing, have been shown to recover the infiltration rate, ensuring the long-term functionality of permeable pavements (Razzaghmanesh & Beecham, 2018). Therefore, periodic monitoring and

preventive maintenance may be necessary to sustain high infiltration rates, particularly in areas prone to heavy particulate loading.

# **5.6** Pavement Usage

### 5.6.1 Calibration/Validation

The accuracy of the automated car detection system described in Section 4.3 was established by parking lot using manual vehicle counts as the reference. The results of the calibration/validation of the model developed are shown in Table 27. Errors are influenced primarily by the camera angle, obstructions, and image overlap, which is affected by the number of cars parked. The PC had the highest accuracy (93.4% calibration, 90.2% validation) as it was the pavement location with fewer obstructions. The CP, despite the better viewing angle and the camera proximity, had an accuracy of 75% and 86.5% for the calibration and validation, respectively, due to the interference of trees. The PA showed moderate accuracies (72.4% for calibration, improving to 78.3% for validation), suggesting that obstructions, mostly overlapping vehicles parked on the CP, had a more pronounced effect. Despite its distance from the camera and partial tree obstruction, the PGr achieved the second-highest accuracy (86.9% for calibration and 87.8% for validation). This high accuracy is primarily attributed to low pavement usage, as the absence of parked cars most of the time simplifies detection (i.e., accurately detecting no vehicles parked). Conversely, the PICP exhibited the lowest accuracies, which can be attributed to obstructions and the camera's oblique viewing angle. Additionally, the PICP was one of the most frequently used pavements, resulting in a higher density of parked cars which increased the likelihood of erroneous counts.

Table 27: Calibration/validation accuracy of pavement occupancy using the automated car detection system

<b>Pavement Type</b>	Calibration Accuracy	Validation accuracy
CP	75.0%	86.5%
PICP	51.5%	64.1%
PGr	86.9%	87.8%
PA	72.4%	78.3%
PC	93.4%	90.2%

Finally, the car detection algorithm was applied to a full 11-day dataset to compare the model's results with the observed data. The results show the differences in parking lot occupancy by pavement type (Figure 55). The parking lot occupancy was defined as the cumulative number of car-minutes per day. This figure compares observed and estimated parking lot occupancy data across five pavement types (CP, PICP, PGr, PA, and PC). The observed and estimated values for CP are in good agreement, with slight discrepancies during peak occupancy periods likely caused by obstructions and overlapping cars. PICP consistently overestimated occupancy, particularly when vehicle density was high. In contrast, the PGr, which was less frequently utilized, exhibited a very good agreement between observed and estimated vehicle occupancy. The PA, which was moderately utilized, exhibited larger errors during peak periods, reflecting the challenges in distinguishing vehicles in more complex images. The PC also exhibited excellent agreement between observed and estimated occupancy due to a relatively unobstructed camera view.

Table 28 summarizes the automated car detection system's performance by pavement type, highlighting accuracy, undercounts, and overcounts. The PICP exhibited the lowest accuracy (56.8%) with a significant undercount rate (33.9%) despite relatively low overcounts (9.3%) observed (Figure 55). Similarly, the PA exhibited a higher undercount than overcount rate, reflecting detection issues caused by obstructions. In contrast, CP, PGr, and PC had balanced values between overcount and undercount, indicating relatively stable detection performance.

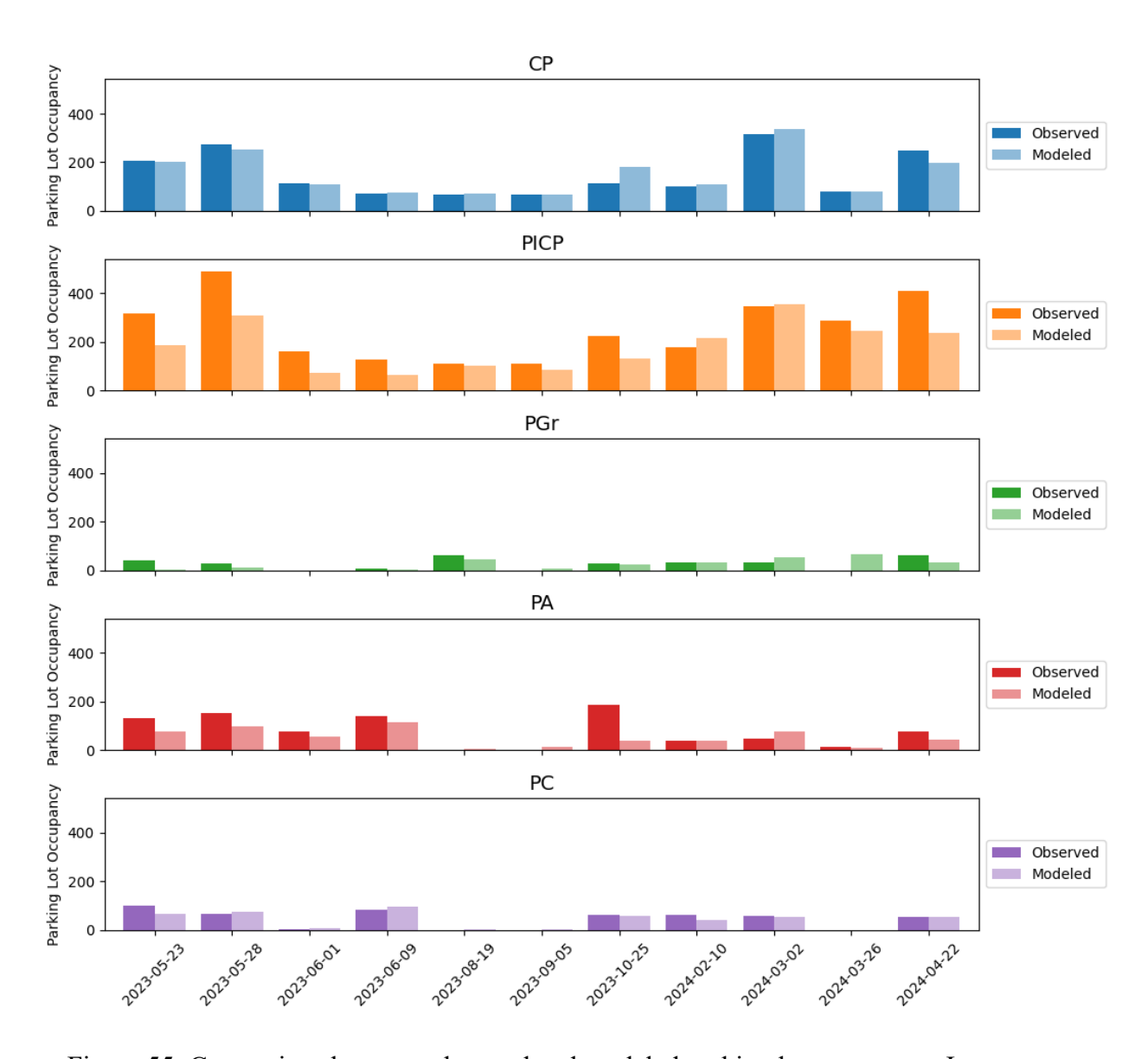


Figure 55: Comparison between observed and modeled parking lot occupancy. Images were analyzed every 5 minutes from dawn to dusk.

Table 28: Accuracy of the automated car detection system for the whole dataset

Pavement	Accuracy	Undercount	Overcount
CP	80%	8.7%	11.3%
PICP	56.8%	33.9%	9.3%
PGr	87.3%	6.7%	6%
PA	74.9%	17.2%	7.8%
PC	92%	4.9%	3.1%

These results suggest that the automated parking lot occupancy system developed, can be used as an indicator of how much each parking lot is used, keeping in mind that several factors affect its accuracy such as, camera viewing angle, pavement usage and obstructions (e.g., trees).

# 5.6.2 Parking Lot Occupancy

The car detection algorithm developed was used to estimate the number of cars parked in each parking lot over the monitoring period allowing a clear comparison of pavement usage trends and computing the pavement usage (Figure 56). As defined earlier, the parking lot occupancy was measured as the cumulative car-minutes per day. Days with missing data or defective camera outputs were excluded from the analysis. Only days where all pavements had complete and reliable data were included to ensure consistency in the comparison.

Figure 56 shows notable differences in parking lot usage across the five pavement types, with PICP standing out as the most heavily used. This contrasts sharply with the PGr, which exhibits the lowest usage despite its proximity to PICP. A possible explanation, other than the proximity to the pavilion, lies in the pavement itself. Unlike the structured surfaces of the other pavements, PGr consists of gravel, which may be less desirable than the other pavement surface types. An anecdotal observation during data collection supports this: A driver explicitly asked one of the researchers whether they could park on the PGr lot, reflecting uncertainty about its suitability and readiness for use. On the other hand, the CP occupancy was moderate with notable fluctuations, suggesting intermittent periods of higher parking activity. The PA showed a similar pattern with fewer peaks, indicating moderate and less variable parking occupancy. On the other hand, the PC exhibited steady but consistently low usage. Overall, the results highlight how pavement surface characteristics affect driver choices in selecting a parking area.

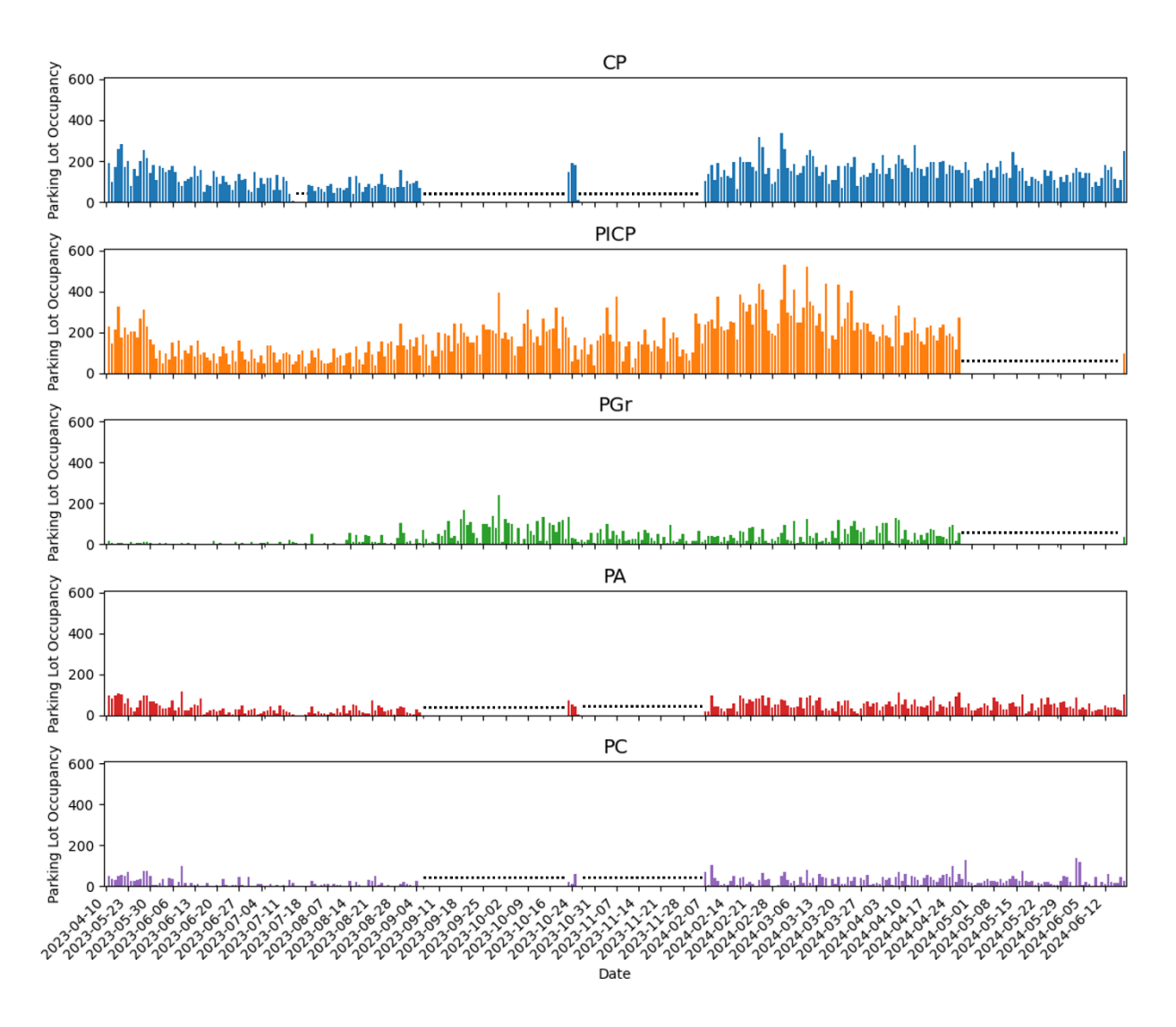


Figure 56: Pavement parking occupancy by pavement type during the monitoring period

# 5.6.3 Correlation Analysis

For the statistical analysis, the events 5 to 7 (see Table 11) were excluded due to the absence of images, resulting in a sample size of 8 events for all pavements. The results of the Spearman correlation analysis between Parking Lot Occupancy and Total Suspended Solids (TSS) show distinct trends across the CP and the permeable pavements. The CP correlation is strong and statistically significant, with a Spearman correlation coefficient of 0.83 (p-value = 0.010), indicating a positive relationship between the pavement lot occupancy and TSS concentrations. This suggests that increased parking lot occupancy on conventional pavement contributes to higher

TSS levels, likely due to the accumulation of particulates and vehicle-related pollutants on the surface.

In contrast, none of the permeable pavements exhibited a statistically significant relationship between the number of cars (p-values: 0.482, 0.823, 0.736, 0.233 from PICP, PGr, PA, and PC, respectively). These results suggest that permeable pavements, regardless of type, do not exhibit the same relationship between occupancy and TSS as conventional pavement. This could be attributed to the infiltration capacity of permeable pavements, which may reduce the accumulation and transport of suspended solids, mitigating the impact of parking lot usage on water quality. In contrast, the impervious surface of the conventional pavement likely facilitates runoff, leading to a stronger link between vehicle activity and TSS concentrations.

#### CHAPTER SIX: CONCLUSIONS AND RECOMMENDATIONS

### 6.1 Conclusions

The PPs outperformed significantly the CP in reducing stormwater runoff and lowering peak flows through water storage. Among the PPs, the PGr provided the highest hydrological benefits in reducing and delaying peak flows. The other PPs also demonstrated significant runoff attenuation. Overall, all four PPs effectively reduced runoff volumes and mitigated flow peaks compared to the CP, underscoring their stormwater management benefits.

All four PP types yielded substantially lower TSS, and VSS concentrations in water outflow compared to the CP. The PICP showed the best performance by producing the lowest and most stable mean TSS and VSS concentrations followed closely by the PGr. The PA exhibited occasionally higher mean values caused by outlier events, while the PC exhibited slightly higher TSS concentrations compared to the other PP types. Overall, these findings confirm the capacity of permeable paved surfaces to reduce suspended solids and volatility in runoff relative to impervious surfaces. Bacterial analyses revealed no statistically significant differences in fecal or non-fecal coliform levels between the CP and the PPs.

Metal concentrations in runoff were notably low for all pavement types, often below practical quantitation limits, with lead generally being undetectable. Water runoff from the CP showed the highest zinc loads, whereas the PC outflow occasionally exhibited higher concentrations of both zinc and copper, likely due to the presence of these metals within its matrix. Meanwhile, the PGr and PA appeared to retain deposited metals, leading to lower metal loads in the outflow. Although some variations were observed in pavement performance, the overall metal levels remained minimal and did not pose a significant environmental concern. The concentration of metals may increase over extended periods of time, considering that they are automobile sourced.

Hardness varied among pavement types, reflecting differences in mineral leaching and infiltration capacity. The PA and PGr outflow displayed higher hardness levels than the CP, while the PC and PGr yielded lower hardness concentrations overall. The PICP typically fell in between, yielding outflow with moderate hardness. These findings highlight that the material composition, infiltration rates, and chemistry of PP materials drive variations in dissolved mineral concentrations.

The PC pavement generated markedly alkaline runoff (i.e., pH around 10), helping precipitate metals out of solution and reducing their environmental impact. By contrast, the CP, PGr, and PICP outflows generally showed moderately alkaline pH levels in the 8–9 range, while the PA's runoff ranged from neutral to mildly alkaline. Statistical analyses confirmed that the pH of the PC was significantly higher than that of the other pavements, suggesting strong buffering capacity that can reduce metal solubility.

All PPs exhibited higher mean EC than the CP, reflecting elevated dissolved ion content in their outflows. Among the PP types, the PC consistently showed the highest conductivity, likely due to its alkaline cement-based matrix. The PA, PGr, and PICP outflows also exhibited higher conductivity than the CP, although the PICP tended to have lower EC than the other PPs. Overall, the material properties and infiltration mechanisms of PPs contribute to the degree of dissolved ion transport.

PAH concentrations were generally low for both the CP and the PPs, with only a few samples exceeding the minimum detection limits. Considering the limited measurements available, the CP exhibited higher PAH levels compared to the PPs, with occasional spikes attributed to point-source contamination like vehicle oil leakage. Over time, PAH concentrations appeared to decrease, suggesting that the initial elevated levels in newly-constructed surfaces decrease with pavement

age. Despite some variability, PAH runoff from all pavements remained well below thresholds of environmental concern.

Correlation results highlighted distinct runoff-pollutant dynamics between the impermeable CP and the PPs. The CP generally showed strong dilution effects for TSS, VSS, and other pollutants during larger storm events, whereas the PPs in large rainfall events revealed higher pollutant mobilization due to infiltration flushing. The permeable designs also displayed fewer consistent correlations with the antecedent dry period than expected, indicating that pavement-specific factors (i.e., void structure, infiltration capacity, and materials) strongly influenced pollutant retention and release. Ultimately, the permeability of these systems altered pollutant transport mechanisms, distinguishing their water quality outcomes from those of the CP.

Daily minimum, average, and maximum temperatures revealed better thermal performance for the PPs overall compared to the CP. The PC and PICP often maintained lower average and maximum temperatures, likely aided by their higher albedo (i.e., lighter color) and surface voids that allowed air circulation. The PGr exhibited strong cooling at night (lowest minimum temperatures), while the PA produced the highest daytime maxima, caused by its darker surface and heat retention properties. Statistical tests confirmed significant temperature differences between pavement types, with the PPs generally mitigating heat more effectively than the CP.

During rainfall, all surfaces cooled as water infiltrated, but the PGr and PC outflows showed consistently lower average water temperatures than the PA and PICP. Although the PICP had a relatively cool surface, its lower infiltration surface prolonged water contact, raising its outflow temperatures. The PA, with the warmest pavement surface, transferred more heat to infiltrating water, producing the highest outflow temperatures. Overall, the PGr and PC were best in

minimizing thermal pollution in stormwater, underscoring the importance of material choice and void structure in heat exchange dynamics.

Automated car detection revealed notable differences in usage by pavement type, with the PICP being the most heavily used and the PGr the least used. This was likely due to drivers' preference for more familiar parking lot surfaces. The CP and PA showed moderate usage with intermittent peaks, while the PC experienced relatively lower but steady usage. Statistical correlations indicated that higher occupancy of the CP corresponded to elevated TSS levels, whereas occupancy had no significant effect on TSS for the PPs, underscoring the effective pollutant mitigation offered by permeable designs.

#### 6.2 Recommendations

Monitoring infiltration rates is essential to assess future clogging that will require maintenance to restore pavement permeability. Although no significant reduction in PP infiltration rates was observed over the monitoring period of this study, it is recommended to perform periodic infiltration rate measurements in order to ascertain the need for maintenance. This should be in the form of vacuum sweeping or pressure washing and should be carried out following the maintenance routine described in SARA's LID Technical Design Guidance Manual.

Both CP and PPs had alkaline outflows, but the pH of the PC was notably higher. While a high pH is beneficial for metal precipitation, it can be detrimental to aquatic wildlife. Therefore, the impact on local ecosystems should be considered when choosing PC.

Regarding surface and water temperature, the PICP and PC are recommended over the CP. The PGr performed similarly to the CP yielding lower temperatures, while the PA had higher temperatures than the CP, which may be a concern in hot environments. For water temperature,

the PC is recommended as it increases only slightly water temperatures, thereby reducing thermal pollution.

Parking preferences, measured by occupancy, revealed that the PICP pavement was the most attractive option, followed by CP, PA, PC, and PGr. The aesthetic appeal and proximity to the playing field influenced these choices. Interestingly, despite being closest to the PICP, the PGr had the least use during the period, suggesting other factors at play in parking decisions.

The findings of this study suggest that PPs have significant environmental benefits and should be considered as one of the LID strategies available for mitigating impermeable ground cover effects in delicate ecosystems and especially over sensitive aquifers. Wider use of permeable surfaces will result in lowering construction costs that will make them more competitive. Constructing PGr and PICP surfaces are particularly attractive since they require no specialized equipment for construction and repair.

### **6.3** Future Study

Evaluating long-term clogging is crucial to ensuring the long-term effectiveness of PPs. Periodic monitoring of infiltration rates will help to understand the clogging effects and guide maintenance scheduling. This will ensure that the pavements maintain their surface permeability over time.

Another area of interest is the impact of pavement surface albedo (i.e., reflectivity) on surface temperatures. To mitigate the increase in temperature, different material compositions for the PA as well as the CP should be evaluated. This would be an effective mechanism for mitigating UHI effects.

The high pH levels observed in the PC runoff warrant further investigation. It is essential to understand the reasons behind the elevated pH and its correlation with higher TSS concentrations.

The significant difference in TSS between PC and other PPs suggests that possibly some cementitious material may be leaching resulting in high pH levels.

As pavement usage increases, hydrocarbons (i.e., TPH and PAH) as well as automobile sourced metals (i.e., Zinc, Copper) are expected to accumulate over time. It would be very interesting to ascertain the long-term effectiveness of these PP types in removing such pollutants by performing water quality measurements at the same site 5 to 7 years in the future.

### REFERENCES

- 1. Tong, S., Liu, A., and Goodrich, J. (2009). "Assessing the water quality impacts of future land-use changes in an urbanizing watershed." *Civil Engineering and Environmental Systems*, 26(1), 3-18.
- 2. US EPA. (1993). "Urban runoff pollution prevention and control planning." National Risk Management Research Laboratory, Office of Research and Development, U.S. Environmental Protection Agency, Cincinnati, Ohio.
- 3. Sharif, H., Jackson, T., Hossain, M., and Zane, D. (2014). "Analysis of Flood Fatalities in Texas." Natural Hazards Review, 0(0), 04014016.
- 4. Fang, Z., Dolan, G., Sebastian, A., and Bedient, P. (2014). "Case Study of Flood Mitigation and Hazard Management at the Texas Medical Center in the Wake of Tropical Storm Allison in 2001." Natural Hazards Review, 15(3), 05014001
- 5. Dorman, T., M. Frey, J. Wright, B. Wardynski, J. Smith, B. Tucker, J. Riverson, A. Teague, and K. Bishop (2013). San Antonio River Basin Low Impact Development Technical Design Guidance Manual, v1. San Antonio River Authority. San Antonio, TX.
- 6. Texas Dept. of Transportation (2016), Pavement Manual, May 2016 Draft.
- 7. Cindy K. Estakhri, Allex E. Alvarez, and Amy Epps-Martin (2007), Guidelines on Construction and Maintenance of Porous Friction Courses in Texas, FHWA/TX-08/0-5262-2.
- 8. Davis, A. P., Shokouhian, M., Sharma, H., Minami, C., and Winogradoff, D. (2003). "Water quality improvement through bioretention: Lead, copper, and zinc removal." Water Environment Research, 75(1), 73-82.
- 9. Kim, M. H., Sung, C. Y., Li, M. H., and Chu, K. H. (2012). "Bioretention for stormwater quality improvement in Texas: Removal effectiveness of Escherichia coli." Separation and Purification Technology, 84, 120-124.
- 10. Houdeshel, C. D., Pomeroy, C. A., Hair, L., and Moeller, J. (2011). "Cost-Estimating Tools for Low-Impact Development Best Management Practices: Challenges, Limitations, and Implications." ASCE Journal of Irrigation and Drainage Engineering 137(3), 183-189.
- 11. Liu, J., Sample, D. J., Bell, C., and Guan, Y. T. (2014). "Review and Research Needs of Bioretention Used for the Treatment of Urban Stormwater." Water, 6(4), 1069-1099.
- 12. TCEQ. (2005). "Complying with the Edwards Aquifer Rules Technical Guidance on Best Management Practices." F. O. Division, ed., TCEQ, Austin, TX.
- 13. San Antonio River Authority (2023). San Antonio River Basin Low Impact Development Technical Design Guidance Manual 3rd Edition.
- 14. TNRCC, Texas Natural Resource Conservation Commission (TNRCC) Method 1005. Total Petroleum Hydrocarbons. 2001.
- 15. Xian, G., Homer, C., Dewitz, J., Fry, J., Hossain, N., and Wickham, J., 2011. The change of impervious surface area between 2001 and 2006 in the conterminous United States. Photogrammetric Engineering and Remote Sensing, Vol. 77(8): 758-762.

- 16. Papagiannakis A.T. and E.A. Masad (2024). Pavement Materials and Design 2nd Edition, ISBN 978-1394150175, Wiley and Sons, p. 501.
- 17. Davis, A. P., Shokouhian, M., & Ni, S. (2001). Loading estimates of lead, copper, cadmium, and zinc in urban runoff from specific sources. Chemosphere, 44(5), 997–1009. https://doi.org/10.1016/S0045-6535(00)00561-0
- 18. Legret, M., & Pagotto, C. (1999). Evaluation of pollutant loadings in the runoff waters from a major rural highway. The Science of the Total Environment, 235(1–3), 143–150. https://doi.org/10.1016/s0048-9697(99)00207-7
- 19. McKenzie, E. R., Money, J. E., Green, P. G., & Young, T. M. (2009). Metals associated with stormwater-relevant brake and tire samples. Science of The Total Environment, 407(22), 5855–5860. https://doi.org/10.1016/j.scitotenv.2009.07.018
- 20. Sansalone, J. J., & Buchberger, S. G. (1997). Partitioning and First Flush of Metals in Urban Roadway Storm Water. Journal of Environmental Engineering, 123(2), 134–143. https://doi.org/10.1061/(ASCE)0733-9372(1997)123:2(134)
- 21. Adachi, K., & Tainosho, Y. (2004). Characterization of heavy metal particles embedded in tire dust. Environment International, 30(8), 1009–1017. https://doi.org/10.1016/j.envint.2004.044
- 22. Chen, J., Wang, H., & Xie, P. (2019). Pavement temperature prediction: Theoretical models and critical affecting factors. *Applied Thermal Engineering*, 158(April). https://doi.org/10.1016/j.applthermaleng.2019.113755
- 23. Collins, K. A., Hunt, W. F., & Hathaway, J. M. (2008). Hydrologic Comparison of Four Types of Permeable Pavement and Standard Asphalt in Eastern North Carolina. *Journal of Hydrologic Engineering*, *13*(12), 1146–1157. <a href="https://doi.org/10.1061/(ASCE)1084-0699(2008)13:12(1146)">https://doi.org/10.1061/(ASCE)1084-0699(2008)13:12(1146)</a>
- 24. Knappenberger, T., Jayakaran, A. D., Stark, J. D., & Hinman, C. H. (2017). Monitoring Porous Asphalt Stormwater Infiltration and Outflow. *Journal of Irrigation and Drainage Engineering*, 143(8), 1–11. https://doi.org/10.1061/(asce)ir.1943-4774.0001197
- 25. Koestoer, R. A., Saleh, Y. A., Roihan, I., & Harinaldi. (2019). A simple method for calibration of temperature sensor DS18B20 waterproof in oil bath based on Arduino data acquisition system. *AIP Conference Proceedings*, 2062(December 2018). https://doi.org/10.1063/1.5086553
- 26. Kumar, K., Kozak, J., Hundal, L., Cox, A., Zhang, H., & Granato, T. (2016). In-situ infiltration performance of different permeable pavements in a employee used parking lot
   A four-year study. *Journal of Environmental Management*, 167, 8–14. https://doi.org/10.1016/j.jenvman.2015.11.019
- 27. Muttuvelu, D. V., Wyke, S., & Vollertsen, J. (2024). Measuring Infiltration Rates in Permeable Asphalt Pavement in Urban Landscapes. *KSCE Journal of Civil Engineering*, 28, 5255–5265. https://doi.org/10.1007/s12205-024-0014-y
- 28. Razzaghmanesh, M., & Beecham, S. (2018). A review of permeable pavement clogging investigations and recommended maintenance regimes. *Water (Switzerland)*, 10(3). https://doi.org/10.3390/w10030337
- 29. Rezaei, A., & Karami, H. (2023). Investigating the Effect of High Strength Clogging Resistant Permeable Pavement (CRP) and Permeable Interlocking Concrete Pavement

- (PICP) on the Characteristics of Runoff. *Environmental Processes*, 10(4). https://doi.org/10.1007/s40710-023-00672-5
- 30. Sansalone, J., Kuang, X., Ying, G., & Ranieri, V. (2012). Filtration and clogging of permeable pavement loaded by urban drainage. *Water Research*, 46(20), 6763–6774. https://doi.org/10.1016/j.watres.2011.10.018
- 31. Selbig, W. R., & Buer, N. (2018). Hydraulic, water-quality, and temperature performance of three types of permeable pavement under high sediment loading conditions. *U.S. Geological Survey Scientific Investigations Report 2018–5037*, *May*, 44. https://pubs.er.usgs.gov/publication/sir20185037
- 32. Valinski, N. A., & Chandler, D. G. (2015). Infiltration performance of engineered surfaces commonly used for distributed stormwater management. *Journal of Environmental Management*, 160, 297–305. https://doi.org/10.1016/j.jenvman.2015.06.032
- 33. Wang, J., Wang, X., Xu, W., Xue, C., Li, H., Sun, Z., Zhang, C., & Li, J. (2023). Characteristics of thermal pollution from stormwater runoff from impermeable/permeable pavement surfaces via a lab-scale experiment. *Journal of Environmental Management*, 325(PB), 116484. https://doi.org/10.1016/j.jenvman.2022.116484
- 34. Wardynski, B. J., Winston, R. J., & Hunt, W. F. (2013). Internal Water Storage Enhances Exfiltration and Thermal Load Reduction from Permeable Pavement in the North Carolina Mountains. *Journal of Environmental Engineering*, 139(2), 187–195. https://doi.org/10.1061/(asce)ee.1943-7870.0000626
- 35. Welker, A. L., Barbis, J. D., & Jeffers, P. A. (2012). A Side-by-Side Comparison of Pervious Concrete and Porous Asphalt. *Journal of the American Water Resources Association*, 48(4), 809–819. https://doi.org/10.1111/j.1752-1688.2012.00654.x
- 36. Winston, R. J., Al-Rubaei, A. M., Blecken, G. T., & Hunt, W. F. (2016). A Simple Infiltration Test for Determination of Permeable Pavement Maintenance Needs. *Journal of Environmental Engineering*, 142(10), 1–5. https://doi.org/10.1061/(asce)ee.1943-7870.0001121

# APPENDIX A: GEOTECHNICAL EXPLORATION AT THE CLASSEN-STEUBING **PARK SITE**

#### Boring Log No. B-8 Project: Sampling Date: 12/23/19 Classen-Steubing Ranch Park San Antonio, Texas N29°37'45.19" W-98°28'32.7" Coordinates: Location: Pavilion and Restroom: See Boring Location Plan Backfill: Cuttings Depth WC PL ы -200 Soil Description SN LL N (ft) CLAYEY GRAVEL with Sand (GC), dense, brown 49 22 SS 10 19 30 40 STRATUM I - color transitions to Tan at 1' SS 1 *50/1 LIMESTONE, very hard, tan STRATUM III SS **50/0 Clayey Gravel (GC) filled void from 5.5-11' SS 18 41 23 60 17 SS 5 36 SS 5 50/5" SS **50/0 Borehole terminated at 18.5 feet Groundwater Data: During drilling: Not encountered Nomenclature Used on Boring Log Split Spoon (SS) Field Drilling Data: Coordinates: Hand-held GPS Unit Logged By: R. Arizola Driller: Eagle Drilling, Inc. WC = Water Content (%) PL = Plastic Limit ** = Blow Counts During Seating Penetration -200 = % Passing #200 Sieve LL = Liquid Limit PI = Plasticity Index N = SPT Blow Count

Figure 57: Borehole location B-8 (Source: Arias Geoprofessionals)

Air rotary: 0 - 18.5 ft

		Boring Log I	No. B-9					
	Project: Classen-Steubing Ranch Park Sampling Date: 12/23/19 San Antonio, Texas							
			Coordinates:	N29°3	37'42.9	2" W	-98°2	8'33.82"
	Location: Parking Lot (So	uth): See Boring Location Plan	Backfill:	Cuttings				
		Soil Description			Depth	S	N W	C N
LIMESTO	ONE, very hard, tan				(ft)			4 **50/1"
STRATU								
						L s	s	1 **50/0"
						`	Ĭ	.   55.5
						L s	s	1 **50/0'
Borehole	terminated at 4.5 feet							
Groundwa		Nomenclature Used on Bori	na Loa					
	ng: Not encountered	Split Spoon (SS)	ng Log					
Field Drillin								
Logged By:	s: Hand-heid GPS Unit R. Arizola	WC = Water Content (%)						
Driller: Eag	le Drilling, Inc.	N = SPT Blow Count						
		** = Blow Counts During Seating Penetration						
Air rotary: 0	1 - 4.5 ft							
		l						

Figure 58: Borehole location B-9 (Source: Arias Geoprofessionals)

### APPENDIX B: PRE-CONSTRUCTION MONITORING

Figure 58Error! Reference source not found. shows that the permeable pavement construction area has significantly changed. The runoff and water quality were monitored to assess the PPS installation impact. A flowmeter was installed in a natural open channel to measure the runoff, and water samples were collected for water quality analysis. The parameters and methods of the water quality analysis are shown in Table 29.

The minimum volume for the water quality sampling was 30000 cubic feet per event (for a minimum of 5 samples collected per event), and a maximum of 72000 cubic feet which represents around 0.5 inch and 1 inch of rainfall in the contribution area. A total of ten events were monitored and considered in water quantity and quality analysis. However, during two of the ten events, the monitoring equipment failed. Events 1 to 6 occurred during the preconstruction. Meanwhile, the 7 and 8 were during the PPS construction. The hydrographs can be seen in Figure 59 and Figure 60. The collected data will be used to analyze the impact of the permeable pavement for both the water volume and hydrograph peaks.



Figure 59: Google Earth® images pre- and during construction: (a) 03/01/2021 and (b) 10/29/2021

Table 29: Water quality parameters and analysis methods

Parameter	Units	Method	Instrument	Test Limits
Temperature	°F	NA	Level TROLL 500, Level Sensor Range	NA
pH	-	Standard Method 4500- H+B	HACH® sensION156	2 to 14
Conductivity	μs/cm	Standard Method 2510 B	HACH® sensION156	0.01 to 200
Total Suspended Solids (TSS)	mg/L	USEPA Gravimetric Method for water and wastewater of solids, nonfilterable suspended solids	Desiccator, Furnace	NA
Volatile Suspended Solids (VSS)	mg/L	USEPA Gravimetric Method for water and wastewater of solids, nonfilterable suspended solids	Desiccator, Furnace	NA
Bacteria (Total Coliform)	CFU/100 ml	Prepared Agar Plates Method with Membrane Filtration for low-turbidity water	Incubator	NA
Zinc Lead	μg/L μg/L	Acid digestion preparation with ICP mass spectrometry	PerkinElmer ELAN DRC-e Spectrometer	4.5E-7 7E-8
Copper	μg/L	-	-	5E-8

The water sampling was set as a flow-paced with 6000 cubic feet per sample volume.

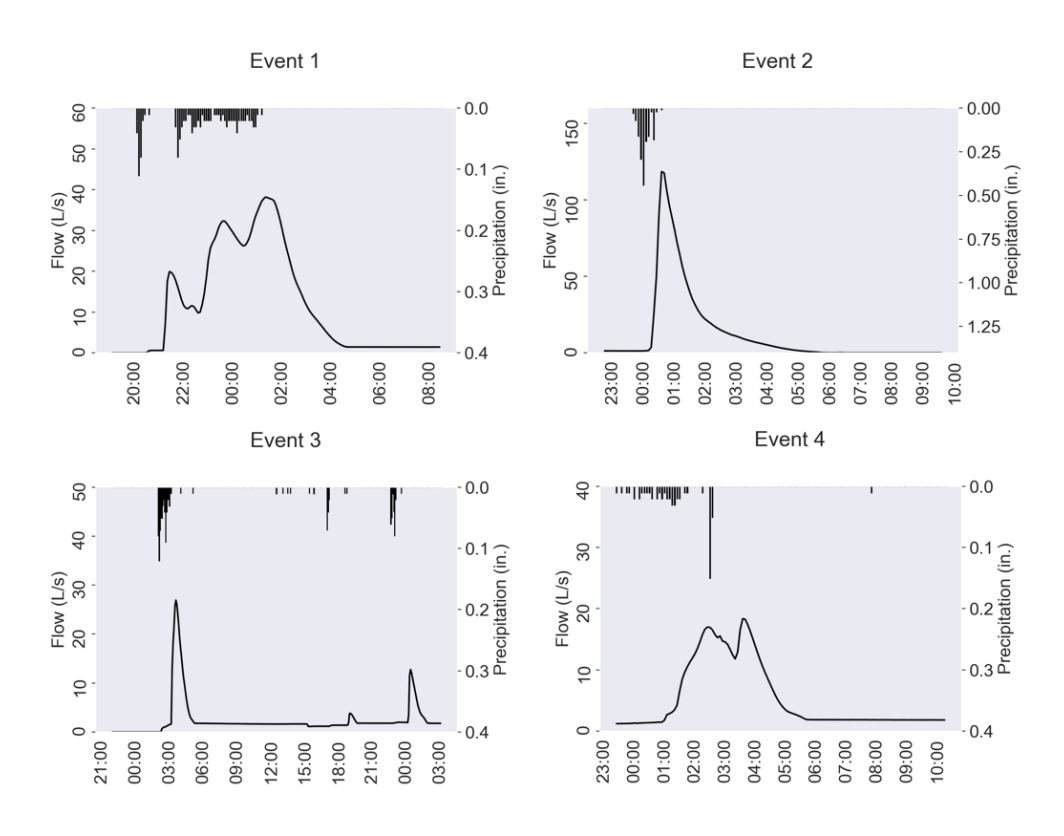


Figure 60: Pre-construction water quantity monitoring events 1 to 4

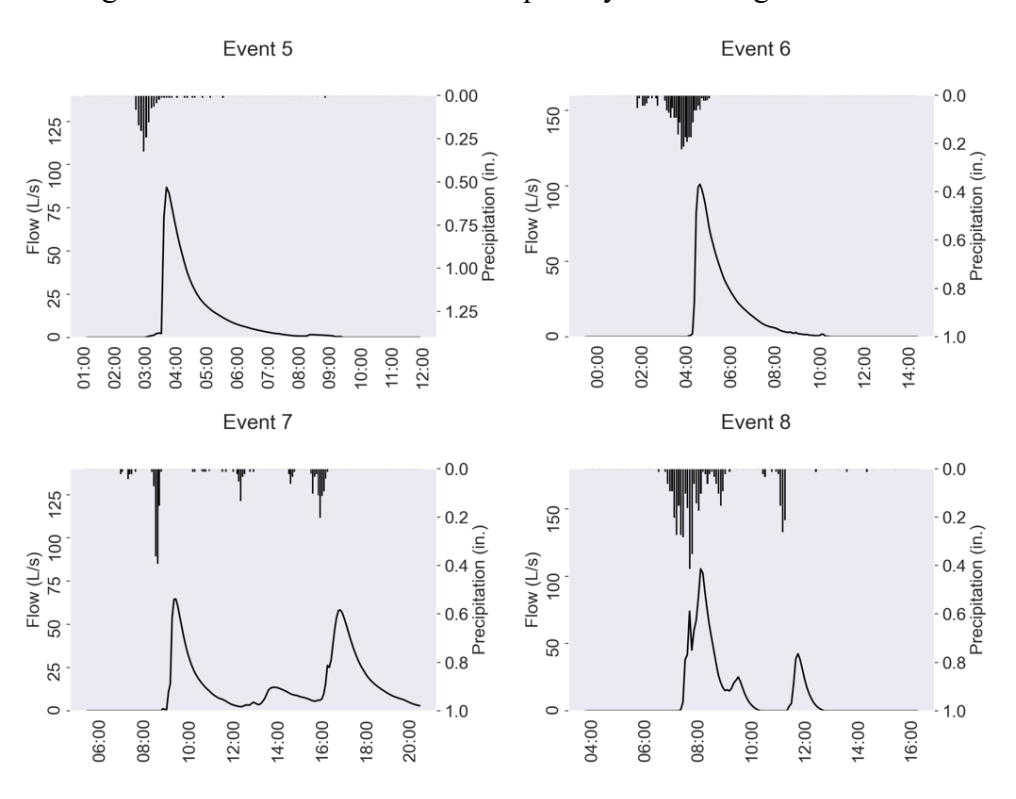


Figure 61: Pre-construction water quantity monitoring events 5 to 8

Figure 61 shows the variation for the events related to water quality. Zinc, Lead, and Copper were analyzed. However, their concentration was less than the detection limit of the methods applied. The water quality data and the data from the traditional permeable pavement will be used as a baseline for the water treatment performance of the PPS.

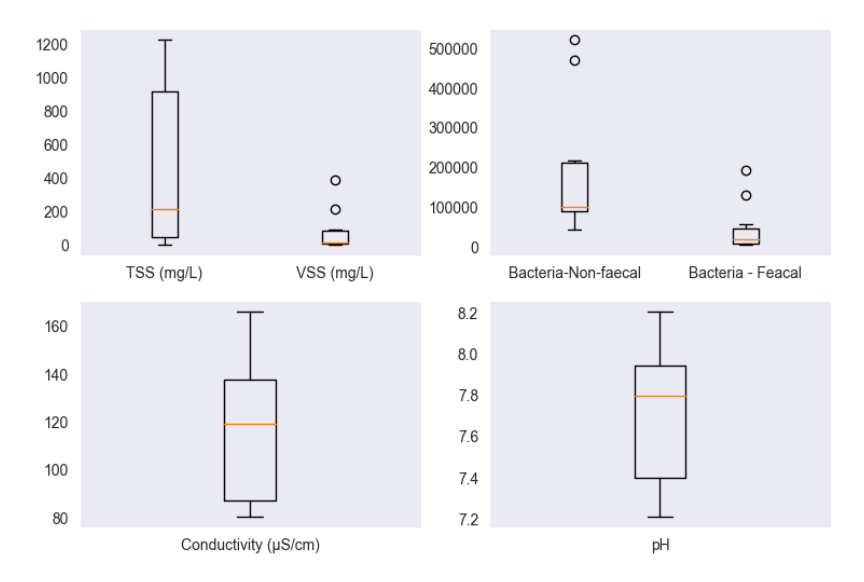


Figure 62: Pre-construction water quality monitoring

# APPENDIX C: WATER QUANTITY MONITORING

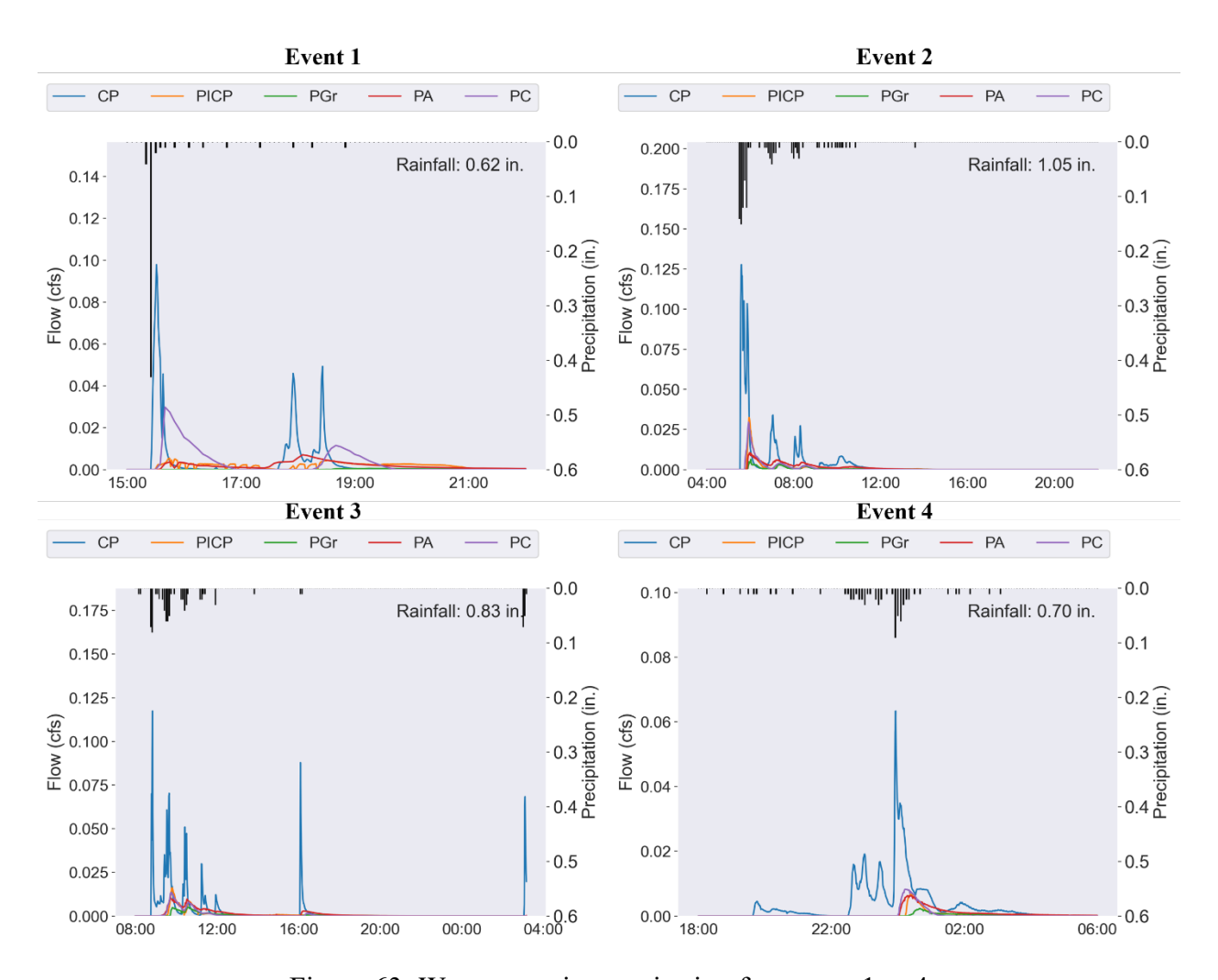


Figure 63: Water quantity monitoring for events 1 to 4

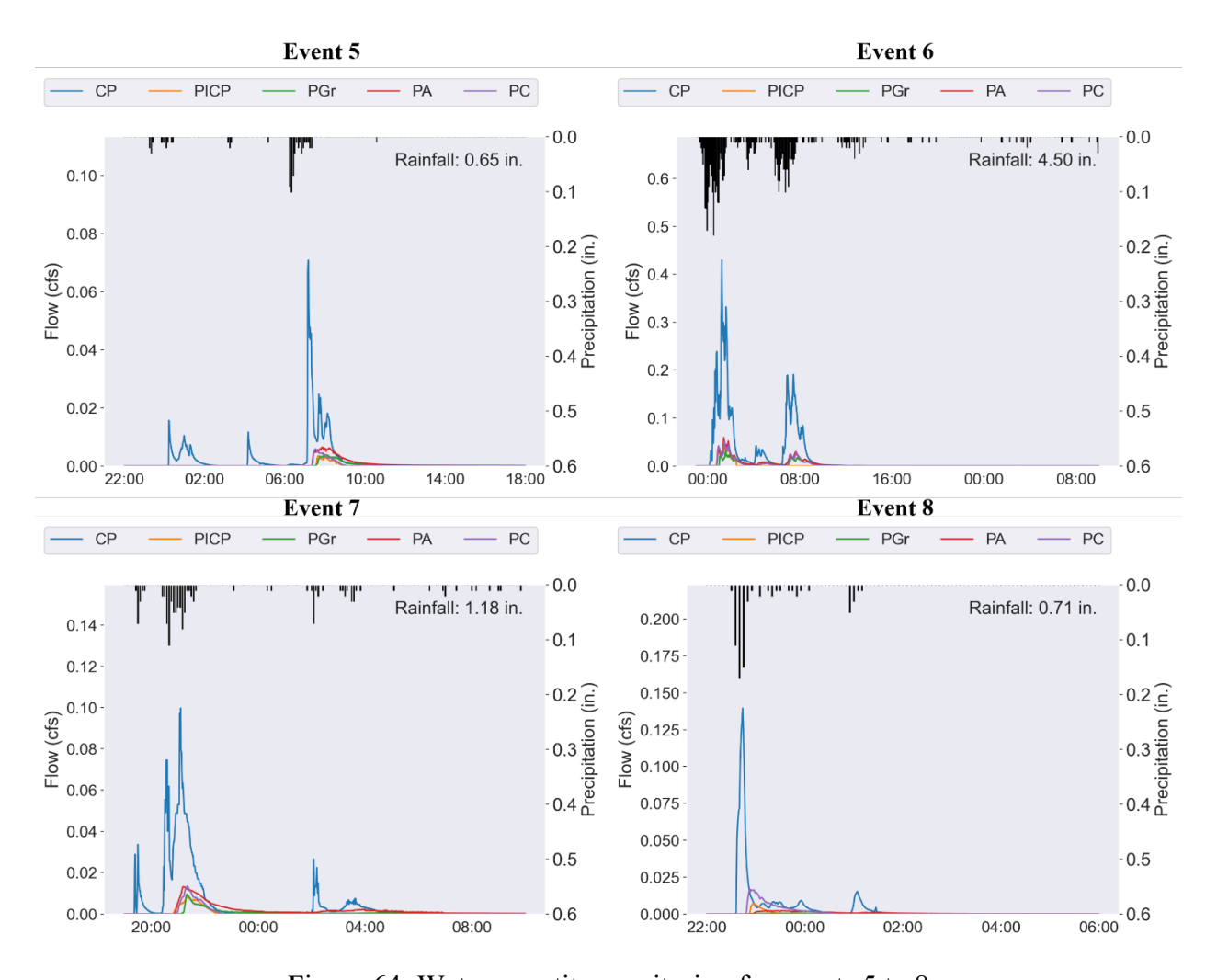
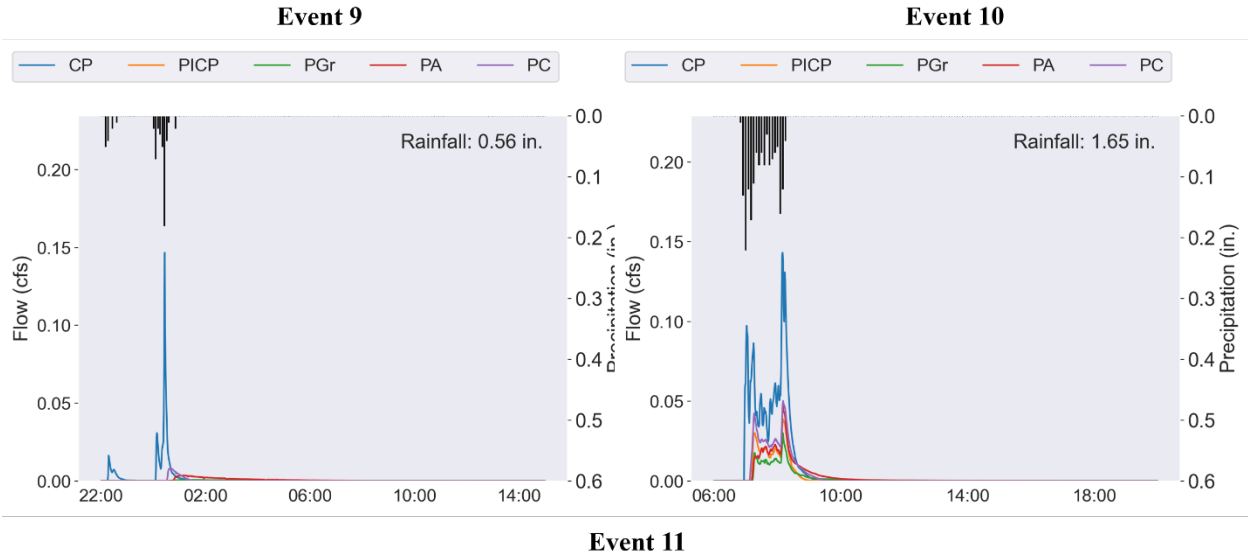


Figure 64: Water quantity monitoring for events 5 to 8



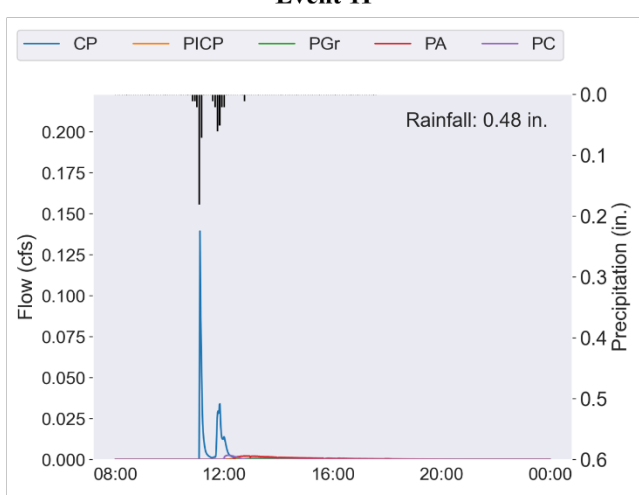
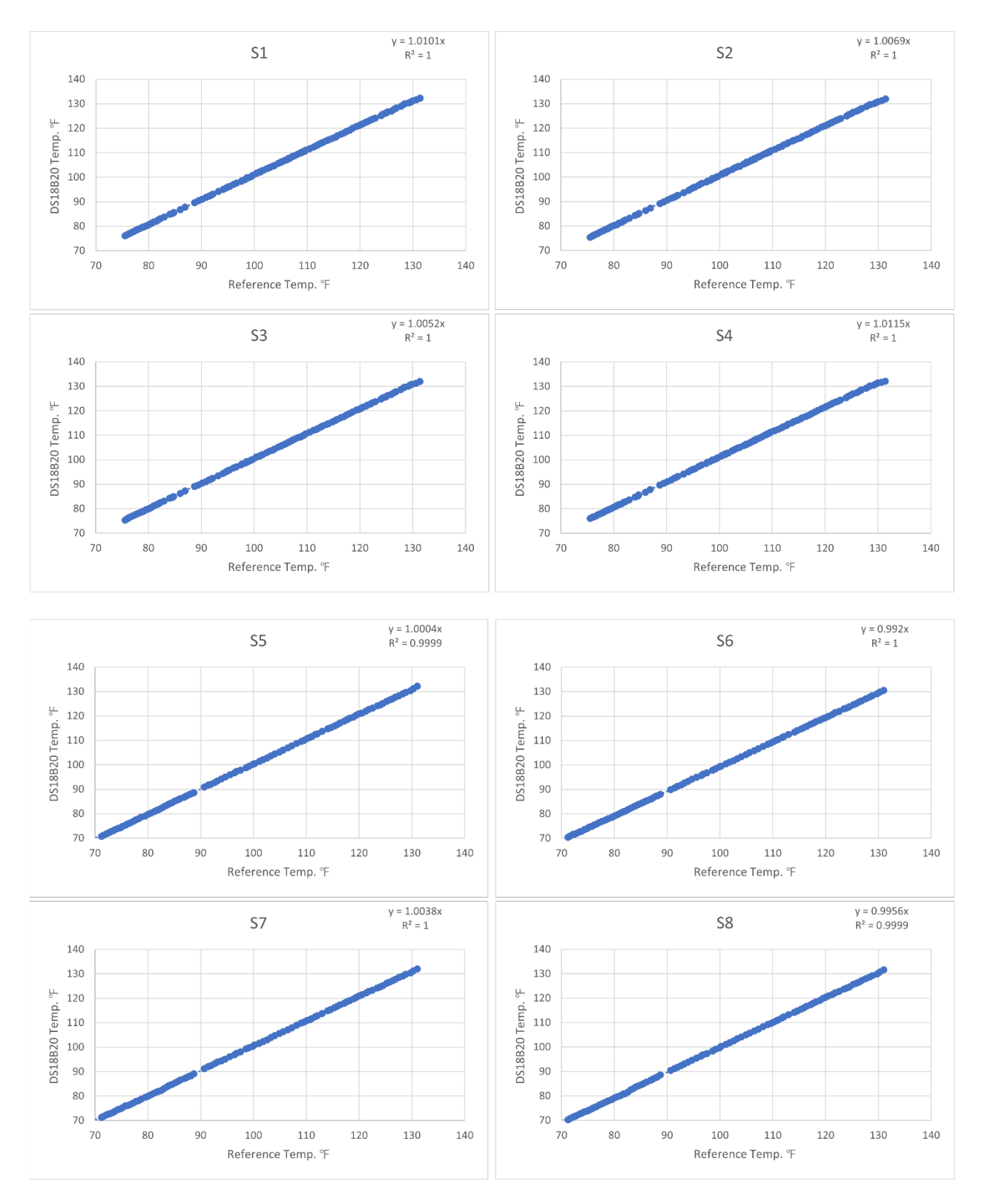


Figure 65: Water quantity monitoring for events 9 to 11

## APPENDIX D: TEMPERATURE GAUGE CALIBRATION



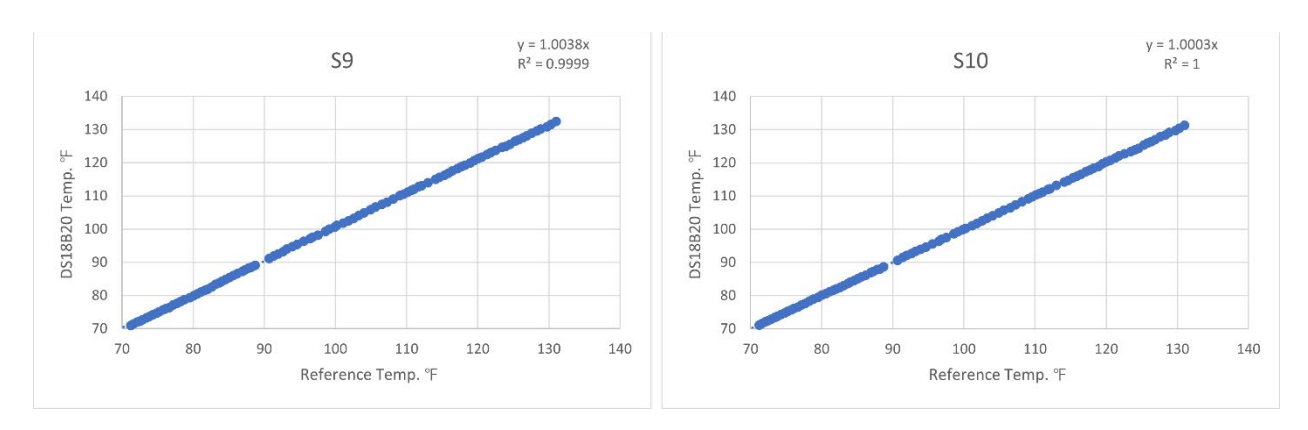


Figure 66: Temperature sensors calibration curves